

学位論文

Anomaly of Hydrogen Recombination Line Ratio
in Ultraluminous Infrared Galaxies

(超高光度赤外線銀河における
水素再結合輝線強度比異常)

平成28年12月 博士（理学）申請

東京大学大学院理学系研究科
物理学専攻

矢野 健一

Abstract

Ultraluminous infrared galaxies (ULIRGs) radiate most ($\geq 90\%$) of their extremely large luminosities ($> 10^{12}L_{\odot}$) as infrared dust emission. Since their discovery in 1980's, it has been long debated which is the dominant energy source in ULIRGs: starburst activities and/or active galactic nuclei (AGNs). ULIRGs are thought to be dust-enshrouded quasars formed through the merger processes, eventually shedding their dust to evolve into quasars or massive ellipticals. Thus understanding the dust-obscured energy source of ULIRGs is important for investigating the merger-driven evolutionary scenario of galaxies. However, the large amount of dust harboured in ULIRGs makes it difficult to investigate the energy sources observationally.

In this thesis, we take two approaches to investigate the energy sources and the nature of starburst activities in ULIRGs.

First, in order to investigate the contribution of starburst activities as the energy source in ULIRGs quantitatively, we conducted systematic observations of the H I Br α line ($4.05 \mu\text{m}$) in 50 nearby ($z < 0.3$) ULIRGs with *AKARI*. The Br α line is predicted to be the brightest among the H I lines, which trace ionizing photons from OB stars and are used as an indicator of star formation, under heavy dust-extinction conditions ($A_V > 15$ mag). We detected the Br α line in 33 ULIRGs. The luminosity of the line ($L_{\text{Br}\alpha}$) correlates well with that of the $3.3 \mu\text{m}$ polycyclic aromatic hydrocarbon (PAH) emission ($L_{3.3}$). Thus we utilize $L_{3.3}$ also as an indicator of star formation in fainter objects where the Br α line is undetected. We compare $L_{\text{Br}\alpha}$ (or $L_{3.3}$) with the total infrared luminosity (L_{IR}) to investigate the contribution of starburst activities as the energy sources in ULIRGs. Among the 33 galaxies where the Br α line is detected, the mean $L_{\text{Br}\alpha}/L_{\text{IR}}$ ratio in LINERs/Seyferts is significantly lower than that in H II galaxies. This difference

is reconfirmed with the $L_{3.3}/L_{\text{IR}}$ ratio in the larger sample (46 galaxies). Using the ratios, we estimate that the contribution of starburst in LINERs/Seyferts is $(67 \pm 9)\%$, and active galactic nuclei contribute to the remaining $(33 \pm 9)\%$. However, comparing the number of ionizing photons, $Q_{\text{Br}\alpha}$, derived from $L_{\text{Br}\alpha}$ with that, Q_{IR} , expected from star formation rate required to explain L_{IR} , we find that the mean $Q_{\text{Br}\alpha}/Q_{\text{IR}}$ ratio is only $(55.5 \pm 7.5)\%$ even in H II galaxies which are thought to be energized by pure starburst. We propose that dust within H II regions absorbs a significant fraction of ionizing photons.

Next, in order to investigate the validity of the standard theory of H I line ratios, case B, in ULIRGs, we conducted systematic observations of the H I Br β ($2.63 \mu\text{m}$) line in addition to the Br α line in 52 nearby ($z < 0.3$) ULIRGs with *AKARI*. We detected the Br α and Br β lines in 31 ULIRGs. Among the 31 ULIRGs, three galaxies, IRAS 10494+4424, IRAS 10565+2448, and Mrk 273, show a Br β /Br α line ratio (0.873 ± 0.074 , 0.983 ± 0.053 , and 1.029 ± 0.037 , respectively) significantly higher than that of case B (0.565). We cannot explain the high Br β /Br α line ratio in the three galaxies with the combination of the case B theory and dust extinction since dust extinction could reduce but not increase the ratio. We explore possible causes of the high Br β /Br α line ratio. If the Brackett lines are optically thin, we cannot explain the high Br β /Br α line ratio with possible excitation mechanisms: recombination, collisional excitation, and resonant excitation. On the other hand, we show that the deviation of the Br β /Br α line ratio from that of case B can be explained if the Br α line becomes optically thick while the Br β line is still optically thin. We assume that the high Br β /Br α line ratio is produced in an ensemble of H II regions with uniform density gas and each H II region is ionized by a single star. We simulate such H II regions with the Cloudy code and show that the high Br β /Br α line ratio is explained when the Br α line becomes optically thick. To achieve the column density large enough to make the Br α line optically thick within a single H II region, the gas density as high as $n \sim 10^8 \text{ cm}^{-3}$ is required. From this result, we propose an ensemble of H II regions, in each of which the Br α line is optically thick, can explain the high Br β /Br α line ratio.

We suggest that the high-density starburst indicated by our model enhances the OB star population and causes the high efficiency of starburst in ULIRGs.

Contents

1	Introduction	1
1.1	Energy Sources in Ultraluminous Infrared Galaxies	1
1.2	Hydrogen Recombination Line Ratio	2
1.3	Outline of This Thesis	3
2	<i>AKARI</i> Infrared Astronomical Satellite	5
2.1	<i>AKARI</i> Satellite	5
2.2	IRC Near-Infrared Spectroscopy	8
3	Star Formation in Ultraluminous Infrared Galaxies	12
3.1	Introduction	12
3.2	Observation and Data Reduction	13
3.2.1	Targets	13
3.2.2	Spectral Analysis	19
3.2.3	Line Fitting	19
3.3	Results	20
3.3.1	Resultant Spectra and Br α Line Flux	20
3.3.2	Effect of Dust Extinction on the Br α Line	23
3.3.3	Comparison to Other Indicators of Star Formation	29
3.4	Discussion	33
3.4.1	Starburst Contribution	33
3.4.2	Deficit of Ionizing Photons	42
3.5	Summary	44

4	Anomaly of Hydrogen Recombination Line Ratio	46
4.1	Introduction	46
4.2	Observations and Data Reduction	47
4.2.1	Targets	47
4.2.2	Reduction of Spectroscopic Data	48
4.3	Results	50
4.3.1	Line Flux	50
4.3.2	Anomaly of $\text{Br}\beta/\text{Br}\alpha$ Line Ratio	54
4.3.3	Possible Contamination to Brackett Lines	61
4.4	Discussion	64
4.4.1	Possible Causes of Anomaly	64
4.4.2	The Expected Number of High-Density H II Regions in ULIRGs	80
4.4.3	Comparison with Other Hydrogen Recombination Lines	82
4.4.4	Implications with Our Model	88
4.5	Summary	89
5	Conclusion	92
A	Near-Infrared Spectra of Ultraluminous Infrared Galaxies	95
B	$\text{Br}\beta/\text{Br}\alpha$ Line Ratio in Galactic H II Regions	102
B.1	<i>ISO</i> Observation	102
B.2	<i>AKARI</i> Observation	103

Chapter 1

Introduction

1.1 Energy Sources in Ultraluminous Infrared Galaxies

Ultraluminous infrared galaxies (ULIRGs) radiate most ($\geq 90\%$) of their extremely large, quasar-like luminosities ($> 10^{12}L_{\odot}$) as infrared dust emission (Sanders et al. 1988). The possible energy source of their enormous infrared luminosity is starburst activities and/or active galactic nuclei (AGNs). Morphologically, most ULIRGs exhibit merger features. Thus, ULIRGs are thought to be dust-enshrouded quasars formed through the merger processes, eventually shedding their dust to evolve into quasars or massive ellipticals (e.g., Sanders et al. 1988; Sanders & Mirabel 1996). Understanding whether the dust-obscured energy source of ULIRGs is dominated by starburst or AGNs is therefore important for investigating this merger-driven evolutionary scenario.

To identify the energy source of galaxies, optical line ratios have been used to classify galaxies according to the excitation mechanism (e.g., Kim et al. 1998). This optical classification method was promoted by Baldwin et al. (1981), and later modified by Veilleux & Osterbrock (1987). On the basis of two-dimensional line-intensity ratios, such as $[\text{O III}] \lambda 5007/\text{H}\beta$ versus $[\text{N II}] \lambda 6583/\text{H}\alpha$, galaxies are mainly classified into three categories; H II galaxies, Seyferts, and LINERs. The emission lines are mainly excited by starburst and AGNs in H II galaxies and Seyferts, respectively. The line excitation mechanisms in LINERs are not clear and still under debate (e.g., see a review by Ho 2008). However, in ULIRGs, it is difficult to distinguish starburst and AGNs through optical

studies because of their high dust extinction. To avoid this problem, many attempts have been made to reveal dust-obscured energy sources with infrared observations.

Using near-infrared observations with *AKARI*, Imanishi et al. (2008, 2010b) found dust-obscured AGN signatures in a significant fraction of ULIRGs that were optically classified as non-Seyferts. From observations using *ISO* (e.g., Genzel et al. 1998) and *Spitzer* (e.g., Veilleux et al. 2009), the fractional contributions of starburst and AGNs as the energy sources in ULIRGs have been estimated with less bias from dust extinction. Their results from infrared observations, however, rely largely on empirical relations. For instance, many of them use the polycyclic aromatic hydrocarbon (PAH) feature as an indicator of starburst activities. PAHs are thought to be excited by UV photons from OB stars; PAHs emit fluorescent light at infrared wavelengths, but their emission mechanisms are very complex (Draine 2003). PAH emission has not been theoretically related to the number of UV photons from OB stars. Thus, quantitative discussion about the contribution of starburst or AGNs is difficult on the basis of these observations.

To investigate the energy sources of ULIRGs quantitatively, we focus on the near-infrared hydrogen recombination line $\text{Br}\alpha$ ($\mathcal{N} = 5 \rightarrow 4$, $\lambda_{\text{rest}} = 4.051 \mu\text{m}$) and utilize it as a probe of starburst activity in ULIRGs.

1.2 Hydrogen Recombination Line Ratio

ULIRGs harbour large amount of dust, and thus it is important to estimate the amount of dust extinction in ULIRGs to correct observed quantities for this extinction. One of the most widely used indicators of dust extinction is the ratio of hydrogen recombination lines such as the $\text{H}\beta/\text{H}\alpha$ line ratio.

The hydrogen recombination lines have been extensively studied and widely used as a tracer of ionized gas because hydrogen is the simplest and most abundant element in the universe (e.g. Seaton 1959; Johnson 1972; Hummer & Storey 1987; Storey & Hummer 1995). The ratio of the H I line fluxes from photoionized gas can be numerically calculated with assuming so called the case B model. In this model, all Lyman photons are assumed to be absorbed by other hydrogen atoms, and all other H I lines are optically thin. The line ratio calculated with the case B assumption is recognized to explain the observed line ratio

in Galactic H II regions and in nearby starburst galaxies well (e.g. Osterbrock & Ferland 2006).

Comparing observed line ratios with that of case B, we can estimate the amount of dust extinction on the H I lines. In the optical through infrared wavelength, the dust extinction is larger in shorter wavelength (e.g. Draine 2003). If we take a line ratio of two H I lines, the line at the shorter wavelength is extinguished more than that at the longer wavelength, and hence the observed line ratio deviates from the case B prediction. Thus we can evaluate dust extinction from the deviation of the observed line ratio from the case B value.

The most widely used H I line ratio for the estimation of dust extinction is that of the optical H α and H β lines (e.g., Veilleux et al. 1995; Kim et al. 1998), so called Balmer decrement, because their wavelengths are easily accessible from ground-based telescopes. However, in heavily dust-obscured objects such as ULIRGs, dust extinction is so high that the optical Balmer lines trace only the outer region of the object and underestimate the extinction. To avoid this problem, we focus on the infrared H I lines Br α and Br β ($\mathcal{N} = 6 \rightarrow 4$, $\lambda_{\text{rest}} = 2.626 \mu\text{m}$), which are less affected by dust extinction than optical ones.

We hence expect that the Br β /Br α line ratio can be used as a tracer of high dust extinction in ULIRGs. However, it is not clear whether the assumption of case B, i.e., the H I lines other than those of the Lyman series are optically thin, is applicable to H II regions in ULIRGs. Most of the enormous infrared luminosity is thought to be produced by starburst activities in ULIRGs (e.g., Veilleux et al. 2009). This makes ULIRGs have one of the highest star formation rate (SFR) of the order of $\sim 100 M_{\odot} \text{ yr}^{-1}$ in galaxies. This suggests a presence of large amount gas in starburst regions in ULIRGs, and hence H I lines may become optically thick in the regions. We investigate this problem by systematically observing the Br α and Br β lines in ULIRGs.

1.3 Outline of This Thesis

The outline of this thesis is as follows. Following the introduction, we describe the infrared astronomical satellite *AKARI* in Chapter 2. In order to conduct systematic observations of the Br α and Br β line, we use the *AKARI* near-infrared spectroscopy. In Chapter 3,

we discuss the energy sources of ULIRGs with the Br α line, which is expected to be the brightest among H I lines in ULIRGs. In Chapter 4, we investigate the Br β /Br α line ratio in ULIRGs. We discover an anomalously high Br β /Br α line ratio, which we cannot explain with the case B theory and dust extinction. We discuss possible causes of the high Br β /Br α line ratio. We summarize the conclusions of this thesis in Chapter 5.

Chapter 2

AKARI Infrared Astronomical Satellite

In order to conduct a systematic observation of the infrared H I lines, Br α and Br β , whose wavelengths are difficult to access from the ground, we employed the near-infrared spectroscopy of the *AKARI* infrared astronomical satellite. In this chapter, we describe the basic information of the *AKARI* satellite, instruments, and the near-infrared spectroscopy.

2.1 *AKARI* Satellite

The *AKARI* satellite (Murakami et al. 2007) was a Japanese infrared astronomical satellite launched on 2006 February 22 (JST) and conducted numerous astronomical observations until the termination of its operation on 2011 November 24 (JST). The primary mission of *AKARI* was to survey the entire sky at six wavelength bands (9, 18, 65, 90, 140, and 160 μm) so as to provide infrared all-sky catalogues with higher sensitivity and spatial resolution than the first catalogues produced by the *IRAS* mission (Neugebauer et al. 1984). *AKARI* had the capability to make pointed observations of specific targets in the wavelength range from 1.7 to 180 μm in addition to the all-sky survey. The effective aperture of the *AKARI* telescope was 68.5 cm in diameter. Two scientific instruments, the Far-Infrared Surveyor (FIS; Kawada et al. 2007) and the Infrared Camera (IRC; Onaka et al. 2007), were installed on *AKARI*. The telescope and the instruments are cooled down

Table 2.1. *AKARI* Scientific Instruments^a

Cryogenics	Liquid-helium cryostat with Stirling-cycle coolers the telescope and instruments are cooled down to < 7 K
Telescope	Ritchey–Chretien type optics, Effective aperture 68.5 cm
Far-Infrared Surveyor (FIS)	All-Sky Survey, imaging and spectroscopy with FTS Bands: N60 (65 μm), WIDE-S (90 μm), WIDE-L (140 μm), N160 (160 μm)
Infrared Camera (IRC)	All-Sky Survey, imaging and spectroscopy with gratings and a prism Channels: NIR (1.8–5.5 μm), MIR-S (4.6–13.4 μm), MIR-L (12.6–26.5 μm)

^aData taken from Murakami et al. (2007); Nakagawa et al. (2007).

to < 7 K with a cryogenic system, which consists of cryogen (liquid helium) and mechanical coolers (Nakagawa et al. 2007). Figure 2.1 shows a schematic view of the *AKARI* satellite. Scientific instruments are summarized in Table 2.1.

A circular Sun-synchronous polar orbit was adopted as the satellite orbit of *AKARI*. The altitude was approximately 700 km, and the inclination was $98^\circ 2'$. This is schematically shown in Figure 2.2 (Murakami et al. 2007). *AKARI* flew along the border of day and night. The orbital period was approximately 100 minutes. *AKARI* observed a certain sky position with an attitude stability of approximately $1''$ in the pointing mode. One pointing observation took approximately 10 minutes for an exposure time and 20 minutes for a maneuvering time.

Three phases were defined in the observation period of *AKARI* (Murakami et al. 2007). The first six months after the performance-verification phase were defined as Phase 1 (from 2006 May 8 to 2006 November 9). The first All-Sky Survey was conducted during this phase. Some pointed observations of targets at high ecliptic latitudes were also performed. Phase 2 began on 2006 November 10 and ended on 2007 August 26 when *AKARI* exhausted all the helium. During this phase, several pointed observations were conducted in addition to the second All-Sky Survey. The period after the exhaustion of the helium was defined as Phase 3 (after 2007 August 27). In this phase, pointed observations using the IRC/NIR channel, which was able to be operated without the liquid-helium cooling, were conducted. In this thesis, we focus on observations conducted in the liquid-helium cool holding period (Phases 1 & 2) to obtain high quality data.

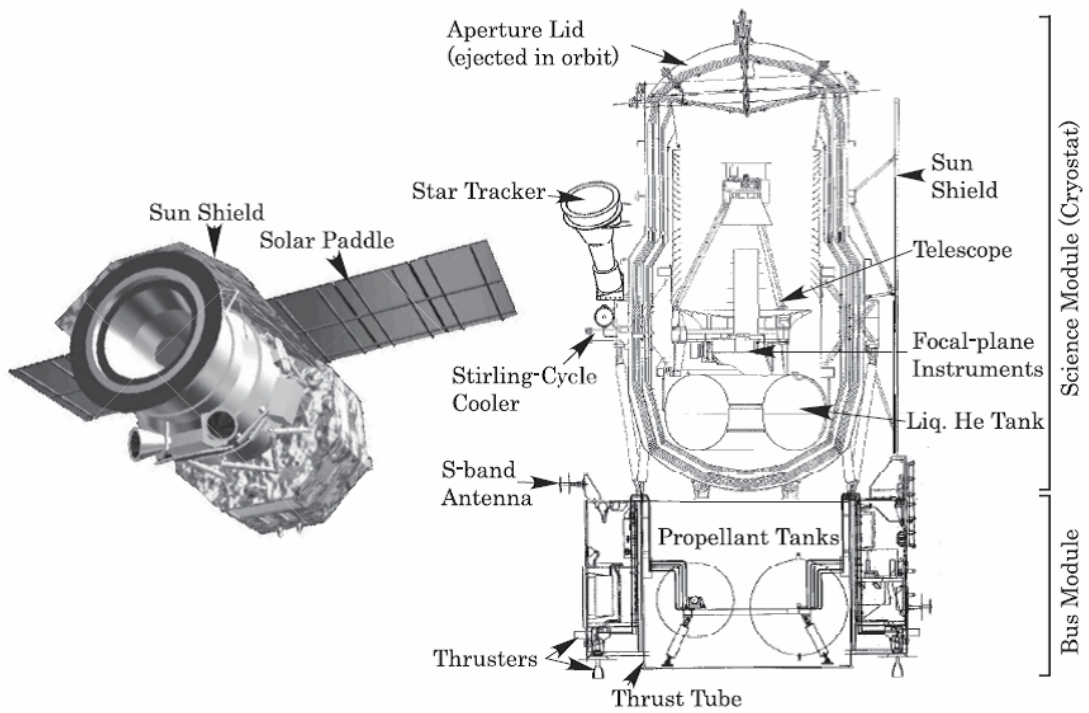


Figure 2.1. Illustration of *AKARI* (left panel) and its sectional view (right panel). This figure is taken from Murakami et al. (2007).

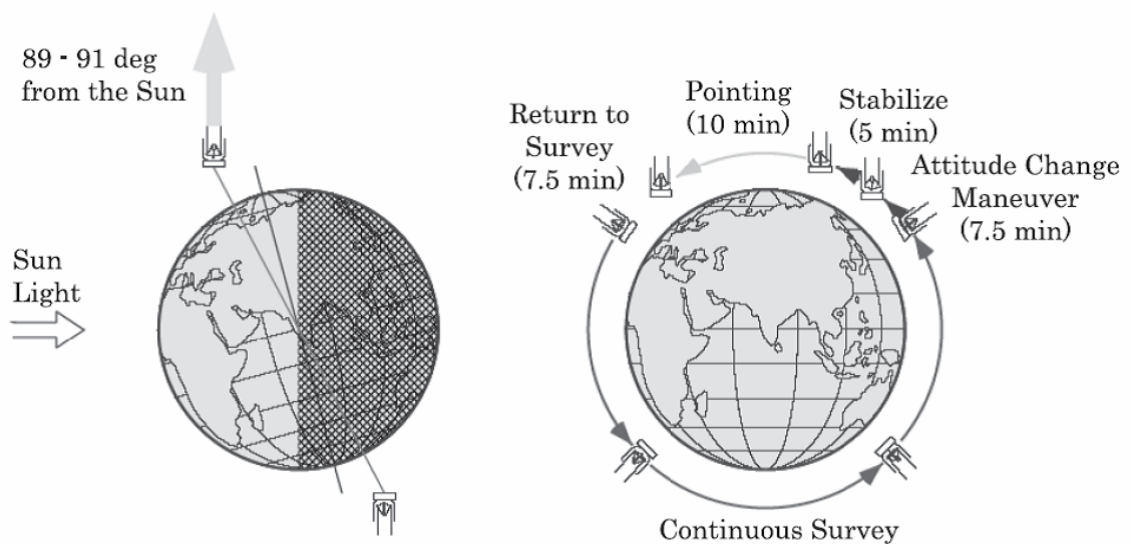


Figure 2.2. Satellite orbit and attitude control for observations. This figure is taken from Murakami et al. (2007).

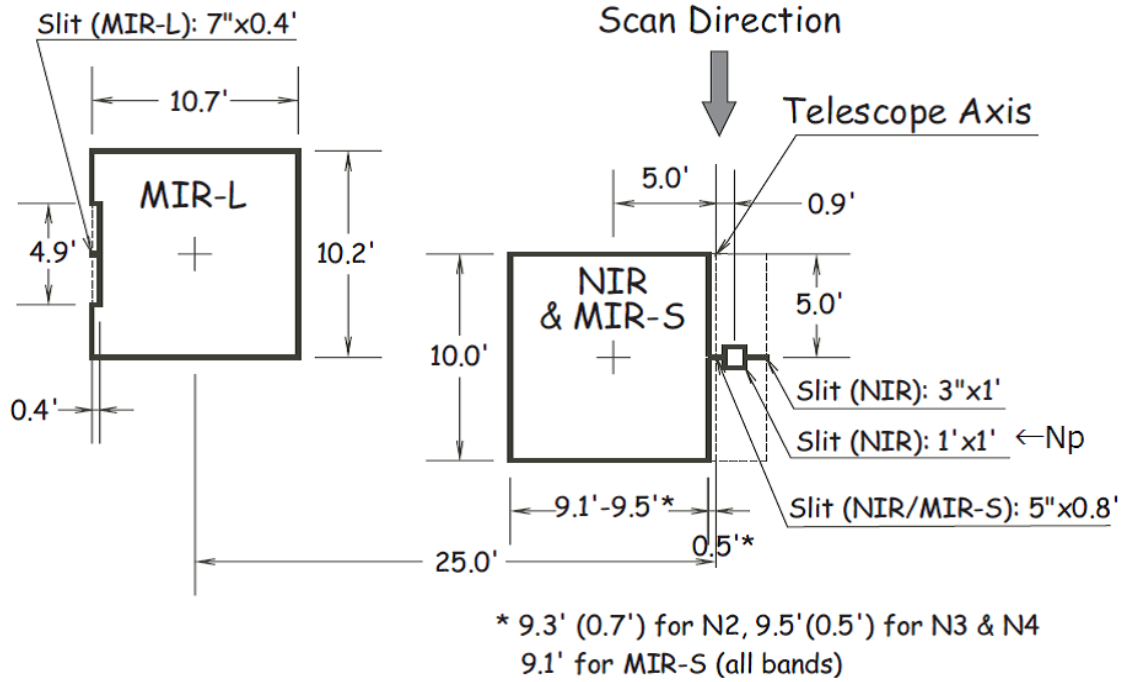


Figure 2.3. Field-of-view of the IRC. This figure is taken from Onaka et al. (2007).

2.2 IRC Near-Infrared Spectroscopy

The IRC performs the near- to mid-infrared ($1.8\text{--}26.5\ \mu\text{m}$) wide-field imaging and low-resolution spectroscopy in the pointing mode of *AKARI* (Onaka et al. 2007). Three independent cameras, the NIR channel ($1.8\text{--}5.5\ \mu\text{m}$), the MIR-S channel ($4.6\text{--}13.4\ \mu\text{m}$), and the MIR-L channel ($12.6\text{--}26.5\ \mu\text{m}$), are installed on the IRC. The NIR adopts a 512×412 InSb array, while the MIR-S and MIR-L employ 256×256 Si:As arrays. The NIR, MIR-S, and MIR-L channels have a pixel scale of $1''.46\times 1''.46$, $2''.34\times 2''.34$, and $2''.51\times 2''.39$, respectively. Each of the three channels has a field-of-view of about $10'\times 10'$. Simultaneous operation of the three channels is possible. The aperture configuration is shown in Figure 2.3. Using a beam splitter, the NIR and MIR-S share the same field-of-view. In addition to the square area, the NIR has an extra slit area of 100×412 pixels.

The NIR is equipped with three filters (N2, N3, and N4) for imaging and two dispersers (NP prism and NG grism) for spectroscopy (Onaka et al. 2007). Table 2.2 summarizes the wavelength coverage of the observations with the NIR. The $2.5\text{--}5.0\ \mu\text{m}$ near-infrared spectroscopic observations are performed with the NG grism mode of the NIR with moderate spectral resolution $R\sim 120$. For the spectroscopy of point sources with the NG grism, a

Table 2.2. IRC NIR Band Characteristics

Name	Mode	Wavelength (μm)	R ($\lambda/\delta\lambda$)
N2	Imaging	2.4	3.4
N3	Imaging	3.2	3.7
N2	Imaging	4,1	2.7
NP	Spectroscopy	1.8–5.5	1.9 @3.5 μm
NG	Spectroscopy	2.5–5.0	120 @3.6 μm



Figure 2.4. Observation sequence of the AOT IRC04. Exposure frames are presented by yellow boxes labeled as “Exposure cycle”. Filter-wheel rotations are shown by light-blue boxes with “W”. The extra observation time, which is overlapped with the maneuvering time and is not guaranteed, is indicated by the green area. This figure is taken from Lorente et al. (2008).

$1' \times 1'$ slit (Np in Figure 2.3) is used to avoid source confusion. The NG grism observations are conducted with the use of Astronomical Observation Template (AOT) IRC04 (Lorente et al. 2008). As shown in Figure 2.4, IRC04 has an imaging observation with the N3 filter during observations with the NG grism. The image is used to determine the reference point of the wavelength calibration for slitless spectroscopy. Figure 2.5 shows an example of raw data taken with IRC04. With reducing the slitless spectra obtained in the Np aperture, we obtain the 2.5–5.0 μm near-infrared spectra. We show an example of the 2.5–5.0 μm spectra of ULIRGs in Figure 2.6. The H I Br α and Br β lines are expected to be observed within this wavelength range in targets with redshift $z \lesssim 0.2$.

This thesis is based on the 2.5–5.0 μm spectroscopic observations performed with the NG grism mode of the IRC on board the *AKARI* satellite. The wavelength coverage of the near-infrared spectroscopy is one of the unique capabilities of *AKARI* because ground-based telescopes cannot continuously cover the wavelength range due to the atmospheric interferences. From space, *ISO* is also capable of spectroscopy in the near-infrared wavelength (Kessler et al. 1996). However, due to the low sensitivity of *ISO* (of the order of a few Jy), observations with *ISO* are limited to bright sources. The *Spitzer* space telescope

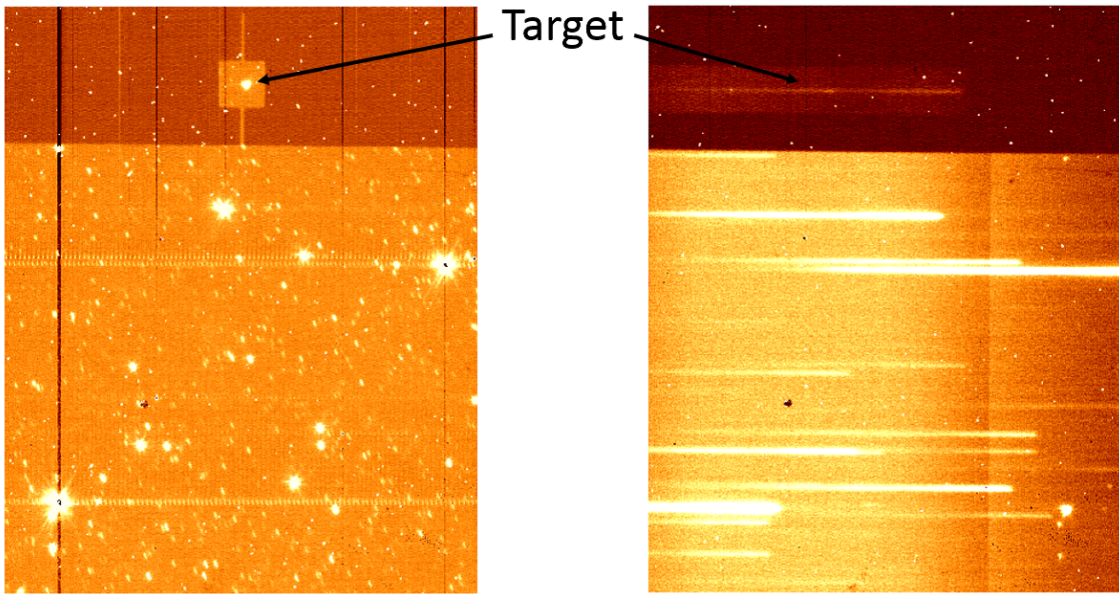


Figure 2.5. Example of raw data taken by IRC04. The left panel shows an N3 reference image while the right panel shows a two-dimensional spectrum taken with the NG grism. The target source is placed in the Np aperture.

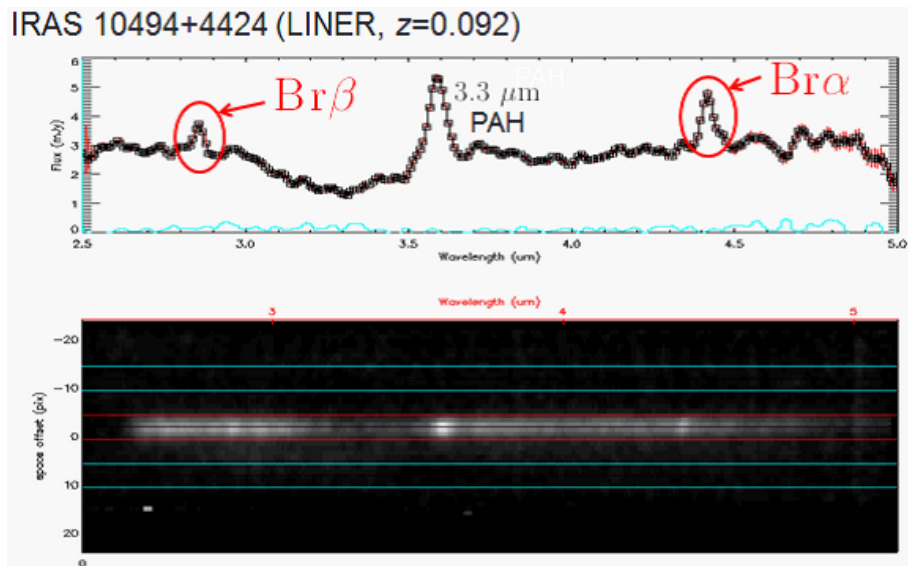


Figure 2.6. Example of the 2.5–5.0 μm spectra obtained with the NG grism mode of the IRC. This is a spectrum of an ULIRG, IRAS 10494+4424. The top panel shows the near-infrared spectrum extracted from the two-dimensional spectrum shown in the bottom panel. The H I Br α and Br β lines are clearly detected in this object.

(Werner et al. 2004) does not have a capability of spectroscopy in wavelengths shorter than $5.2 \mu\text{m}$.

With the unique capability of the *AKARI* near-infrared spectroscopy, we conduct systematic observations of the H I Br α and Br β lines and investigate the nature of starburst activity in ULIRGs.

Chapter 3

Star Formation in Ultraluminous Infrared Galaxies*

3.1 Introduction

In this chapter, we investigate the energy source of ULIRGs with the use of the near-infrared hydrogen recombination line $\text{Br}\alpha$.

Since hydrogen is the simplest element, the number of ionizing photons from OB stars is calculated from the fluxes of hydrogen recombination lines on the basis of the photoionization model in case B (Osterbrock & Ferland 2006). SFRs can then be estimated from the number of ionizing photons on the assumption of the initial mass function (e.g., Kennicutt & Evans 2012). Thus, we can theoretically estimate the strength of starburst activities with hydrogen recombination lines. Owing to its near-infrared wavelength, the observed flux of the $\text{Br}\alpha$ line is predicted to be the highest among hydrogen recombination lines (i.e., $\text{H}\alpha$ or $\text{Pa}\alpha$ lines) in the conditions of high dust extinction (visual extinction $A_V > 15$ mag) which are expected in ULIRGs (e.g., Genzel et al. 1998). Therefore, the $\text{Br}\alpha$ line is the most suitable for probing starburst activities in ULIRGs.

With the unique wavelength coverage of the near-infrared 2.5–5.0 μm spectroscopy of *AKARI* (Murakami et al. 2007; Onaka et al. 2007), we succeed in systematically observing the $\text{Br}\alpha$ line in ULIRGs; the wavelength of this line is difficult to access from ground-

*This chapter is based on Yano et al. (2016).

based telescopes. The near-infrared spectroscopy of *AKARI* also has the unique capability to observe the $3.3 \mu\text{m}$ PAH emission and the $\text{Br}\alpha$ line simultaneously. The $3.3 \mu\text{m}$ PAH emission is stronger than the $\text{Br}\alpha$ line (Imanishi et al. 2008, 2010b), and hence its luminosity can be used as an indicator of star formation for fainter objects if we calibrate it with the luminosity of the $\text{Br}\alpha$ line.

By comparing the luminosity of the $\text{Br}\alpha$ line (or the $3.3 \mu\text{m}$ PAH emission) with the total infrared luminosity, we quantitatively investigate the dust-obscured energy sources in ULIRGs. We assume that the $\text{Br}\alpha$ line luminosity is proportional to the strength of the starburst activity, i.e., the SFR. On the other hand, the total infrared luminosity has contributions from starburst and AGNs. Thus, the ratio of the $\text{Br}\alpha$ line luminosity to the total infrared luminosity is expected to be an indicator of the contribution of starburst to the total infrared luminosity. In Section 3.2, we present our targets, observations, and method of data reduction. The resulting spectra and measured $\text{Br}\alpha$ line fluxes are presented in Section 3.3. We utilize the $\text{Br}\alpha$ line and the $3.3 \mu\text{m}$ PAH emission as indicators of star formation and show a result of comparisons with the total infrared luminosity. Then, in Section 3.4, we discuss the contribution of starburst to the total energy from ULIRGs by comparing the luminosities of the $\text{Br}\alpha$ line and $3.3 \mu\text{m}$ PAH emission with the total infrared luminosity. We summarize our study in this chapter in Section 3.5. Throughout this chapter, we assume that the universe is flat with $\Omega_{\text{M}} = 0.27$, $\Omega_{\Lambda} = 0.73$, and $H_0 = 70.4 \text{ km s}^{-1} \text{ Mpc}^{-1}$ (Komatsu et al. 2011).

3.2 Observation and Data Reduction

3.2.1 Targets

Our targets are selected from the *AKARI* mission program “Evolution of ultraluminous infrared galaxies and active galactic nuclei” (AGNUL; P.I. T. Nakagawa), which aimed to investigate the connection between ULIRGs and AGNs. The AGNUL program conducted systematic near-infrared spectroscopic observations of ULIRGs in the local universe. The target ULIRGs of AGNUL are mainly drawn from a flux-limited catalog called the 1 Jy sample (Kim & Sanders 1998). The 1 Jy sample contains 118 ULIRGs which are selected

from the *IRAS* Faint Source Catalog (Moshir et al. 1992) on the basis of their $60\ \mu\text{m}$ flux higher than 1 Jy and their total infrared luminosity (L_{IR}) higher than $10^{12}L_{\odot}$. Among the archived data of AGNUL, we focus on the observations conducted during the liquid-He cool holding period (2006 May 8–2007 August 26; Murakami et al. 2007). As a result, 50 near-infrared grism spectroscopic observations of ULIRGs are selected and used for this study. Table 3.1 shows the observation log. Table 3.2 summarizes the basic information, such as redshifts and *IRAS*-based L_{IR} of our target ULIRGs.

The spectra of all the targets have been reported by Imanishi et al. (2008, 2010b). The $3.3\ \mu\text{m}$ PAH feature in these galaxies is closely investigated in their papers, but the Br α line is not discussed in detail. Thus, we further reduced the spectra to systematically derive the Br α line fluxes in the sample for the first time, while the $3.3\ \mu\text{m}$ PAH emission fluxes and optical classifications of the galaxies are taken from Imanishi et al. (2008, 2010b).

Table 3.1. Observation Log of ULIRGs

Object Name	Observation ID	Observation Date
IRAS 00183–7111	1100137.1	2007 May 2
IRAS 00456–2904	1100221.1	2007 Jun 19
IRAS 00482–2721	1100036.1	2006 Dec 21
IRAS 01199–2307	1100209.1	2007 Jul 1
IRAS 01298–0744	1100226.1	2007 Jul 10
IRAS 01355–1814	1100018.1	2007 Jan 6
IRAS 01494–1845	1100215.1	2007 Jul 10
IRAS 01569–2939	1100225.1	2007 Jul 7
IRAS 02480–3745	1100030.1	2007 Jan 14
IRAS 03209–0806	1100210.1	2007 Aug 8
IRAS 03521+0028	1100200.1	2007 Aug 19
IRAS 04074–2801	1100201.1	2007 Aug 14
IRAS 04313–1649	1100031.1	2007 Feb 22
IRAS 05020–2941	1100003.1	2007 Feb 28
IRAS 05189–2524	1100129.1	2007 Mar 8
IRAS 06035–7102	1100130.1	2007 Mar 11
IRAS 08572+3915	1100049.1	2006 Oct 29
IRAS 08591+5248	1100121.1	2007 Apr 21
IRAS 09320+6134 (UGC 5101)	1100134.1	2007 Apr 22
IRAS 09463+8141	1100004.1	2006 Oct 8
IRAS 09539+0857	1100267.1	2007 May 19
IRAS 10035+2740	1100216.1	2007 May 15
IRAS 10091+4704	1100122.1	2007 May 7
IRAS 10494+4424	1100266.1	2007 May 16
IRAS 10594+3818	1100021.1	2006 Nov 23
IRAS 11028+3130	1100006.1	2006 Nov 26
IRAS 11180+1623	1100202.1	2007 Jun 5
IRAS 11387+4116	1100269.1	2007 May 29
IRAS 12447+3721	1100022.1	2006 Dec 15
IRAS 12540+5708 (Mrk 231)	1100271.1	2007 May 30
IRAS 13428+5608 (Mrk 273)	1100273.1	2007 Jun 8
IRAS 13469+5833	1100023.1	2006 Dec 7
IRAS 13539+2920	1100235.1	2007 Jul 6
IRAS 14121–0126	1100011.1	2007 Jan 22
IRAS 14202+2615	1100212.1	2007 Jul 15
IRAS 14394+5332	1100283.1	2007 Jun 25
IRAS 15043+5754	1100213.1	2007 Jun 23
IRAS 16333+4630	1100013.1	2007 Feb 8
IRAS 16468+5200	1100249.1	2007 Aug 10

Table 3.1. (continued)

Object Name	Observation ID	Observation Date
IRAS 16487+5447	1100247.1	2007 Aug 6
IRAS 17028+5817	1100248.1	2007 Aug 8
IRAS 17044+6720	1100297.1	2007 May 31
IRAS 17068+4027	1100026.1	2007 Feb 26
IRAS 17179+5444	1100253.1	2007 Aug 23
IRAS 19254−7245	1100132.1	2007 Mar 30
IRAS 21477+0502	1100207.1	2007 May 22
IRAS 22088−1831	1100214.1	2007 May 19
IRAS 23128−5919	1100294.1	2007 May 10
IRAS 23129+2548	1100015.1	2006 Dec 22
IRAS 23498+2423	1100287.1	2007 Jul 1

Table 3.2. Basic Information of Our Target ULIRGs

Object Name	z^a	D_L^b (Mpc)	F_{25}^c (Jy)	F_{60}^c (Jy)	F_{100}^c (Jy)	L_{IR}^d ($10^{12}L_\odot$)	Optical ^e Class	$F_{3.3}^f$ ($10^{-14}\text{erg s}^{-1}\text{cm}^{-2}$)	Ref. ^g
IRAS 00183–7111 ^{hi}	0.327	1717	0.13	1.20	1.19	7.56	LINER	< 1.8	1
IRAS 00456–2904	0.110	508	0.14	2.60	3.38	1.40	H II	4.0	2
IRAS 00482–2721	0.129	604	< 0.18	1.13	1.84	1.17	LINER	1.3	3
IRAS 01199–2307	0.156	744	< 0.16	1.61	1.37	1.22	H II	0.8	2
IRAS 01298–0744 ^j	0.136	640	0.19	2.47	2.08	1.62	H II	1.7	4
IRAS 01355–1814 ^j	0.192	935	0.12	1.40	1.74	2.80	H II	0.6	5
IRAS 01494–1845	0.158	753	< 0.15	1.29	1.85	1.71	Unclassified	2.2	5
IRAS 01569–2939	0.140	660	0.14	1.73	1.51	1.26	H II	1.8	3
IRAS 02480–3745	0.165	790	< 0.11	1.25	1.49	1.43	Unclassified	1.5	5
IRAS 03209–0806	0.166	798	< 0.13	1.00	1.69	1.77	H II	2.2	6
IRAS 03521+0028 ^j	0.152	721	0.20	2.52	3.62	3.32	LINER	2.2	7
IRAS 04074–2801 ^j	0.154	731	0.07	1.33	1.72	1.47	LINER	0.9	2
IRAS 04313–1649	0.268	1364	0.07	1.01	1.10	3.58	Unclassified	< 0.4	5
IRAS 05020–2941	0.154	734	0.10	1.93	2.06	1.79	LINER	1.0	2
IRAS 05189–2524 ^k	0.043	187	3.47	13.25	11.84	1.55	Seyfert 2	30.0	8
IRAS 06035–7102 ^{ilm}	0.079	359	0.62	5.34	6.18	1.68	H II	11.2	4
IRAS 08572+3915 ^k	0.058	260	1.76	7.30	4.77	1.37	LINER	< 4.2	9
IRAS 08591+5248	0.157	750	< 0.16	1.01	1.53	1.50	Unclassified	1.4	10
UGC 5101 ^{kn}	0.039	173	1.02	11.68	19.91	1.05	LINER	22.5	11
IRAS 09463+8141	0.156	743	< 0.07	1.43	2.29	1.81	LINER	2.2	5
IRAS 09539+0857	0.129	603	< 0.15	1.44	1.04	0.62	LINER	1.2	12
IRAS 10035+2740	0.166	793	< 0.17	1.14	1.63	1.77	Unclassified	1.4	13
IRAS 10091+4704	0.246	1237	< 0.08	1.18	1.55	3.49	LINER	0.7	5
IRAS 10494+4424	0.092	420	0.16	3.53	5.41	1.48	LINER	3.6	7
IRAS 10594+3818	0.158	753	< 0.15	1.29	1.89	1.74	H II	2.6	5
IRAS 11028+3130 ^j	0.199	971	0.09	1.02	1.44	2.47	LINER	0.6	12
IRAS 11180+1623	0.166	795	< 0.19	1.19	1.60	1.80	LINER	0.5	5
IRAS 11387+4116	0.149	705	< 0.14	1.02	1.51	1.27	H II	1.9	14
IRAS 12447+3721 ^j	0.158	753	0.10	1.04	0.84	1.01	H II	1.3	5
Mrk 231 ^{ik}	0.042	186	8.84	30.80	29.74	3.89	Seyfert 1	76.6	15
Mrk 273 ^{ik}	0.038	166	2.36	22.51	22.53	1.29	Seyfert 2	24.8	7
IRAS 13469+5833 ^j	0.158	752	0.04	1.27	1.73	1.43	H II	1.4	1
IRAS 13539+2920	0.108	500	0.12	1.83	2.73	1.14	H II	4.3	16
IRAS 14121–0126 ^j	0.150	712	0.11	1.39	2.07	1.84	LINER	2.9	3
IRAS 14202+2615	0.159	757	0.15	1.49	1.99	2.19	H II	4.2	12
IRAS 14394+5332	0.105	481	0.35	1.95	2.39	1.40	Seyfert 2	6.2	17
IRAS 15043+5754	0.151	714	0.07	1.02	1.50	1.29	H II	2.0	6
IRAS 16333+4630 ^j	0.191	930	0.06	1.19	2.09	2.84	LINER	2.1	7
IRAS 16468+5200	0.150	711	0.10	1.01	1.04	1.06	LINER	0.6	5
IRAS 16487+5447	0.104	477	0.20	2.88	3.07	1.23	LINER	3.3	9
IRAS 17028+5817	0.106	489	0.10	2.43	3.91	1.42	LINER	3.7	9
(E nucleus)	H II	0.4	...
(W nucleus)	LINER	3.3	...
IRAS 17044+6720	0.135	634	0.36	1.28	0.98	1.71	LINER	2.3	18
IRAS 17068+4027	0.179	865	0.12	1.33	1.41	2.04	H II	2.2	5
IRAS 17179+5444	0.147	696	0.20	1.36	1.91	2.03	Seyfert 2	1.2	5
IRAS 19254–7245 ^{lo}	0.062	275	1.34	5.30	6.70	1.54	Seyfert 2	3.8	4
IRAS 21477+0502 ^j	0.171	822	0.16	1.14	1.46	2.19	LINER	0.6	5

Table 3.2. (continued)

Object Name	z^a	D_L^b (Mpc)	F_{25}^c (Jy)	F_{60}^c (Jy)	F_{100}^c (Jy)	L_{IR}^d ($10^{12}L_\odot$)	Optical ^e Class	$F_{3.3}^f$ ($10^{-14}\text{erg s}^{-1}\text{cm}^{-2}$)	Ref. ^g
IRAS 22088–1831 ^j	0.170	818	0.07	1.73	1.73	1.75	H II	< 2.0	1
IRAS 23128–5919 ^{ikm}	0.045	197	1.64	10.94	10.68	1.04	H II	32.0	19
IRAS 23129+2548 ^j	0.179	864	0.08	1.81	1.64	1.89	LINER	< 0.4	5
IRAS 23498+2423 ^j	0.212	1045	0.12	1.02	1.45	3.17	Seyfert 2	< 1.9	5

^aRedshift.

^bLuminosity distance calculated from z using our adopted cosmology.

^c*IRAS* fluxes at 25 μm (F_{25}), 60 μm (F_{60}), and 100 μm (F_{100}). These fluxes are taken from the *IRAS* Faint Source Catalog (Moshir et al. 1992), except for galaxies with additional notes.

^dTotal infrared (3–1100 μm) luminosity calculated with $L_{IR} = 4\pi D_L^2(\xi_1\nu F_{25} + \xi_2\nu F_{60} + \xi_3\nu F_{100})$, (ξ_1, ξ_2, ξ_3) = (2.403, -0.2454 , 1.6381) (Dale & Helou 2002). For sources with upper limits, we follow the method described in Imanishi et al. (2008, 2010b). The upper and lower limits on the infrared luminosity are obtained by assuming that the actual flux is equal to the *IRAS* upper limit and to zero value, respectively, and the average of these values is adopted as the infrared luminosity. Since the calculation is based on our adopted cosmology, the infrared luminosity of IRAS 09539+0857 is estimated to be less than that of $10^{12}L_\odot$, however, we treat this object as a ULIRG in this paper.

^eOptical classification of galaxies. These classifications are taken from Veilleux et al. (1999a), except for galaxies with additional notes.

^fObserved flux of 3.3 μm PAH emission. These fluxes are taken from Imanishi et al. (2008), except for galaxies with additional notes.

^gReferences for redshift: (1) Fisher et al. (1995), (2) 6dF Galaxy Survey (Jones et al. 2004) Data Release (DR) 3 (Jones et al. 2009), (3) 2dF Galaxy Redshift Survey (Colless et al. 2001) Final DR (Colless et al. 2003), (4) Strauss et al. (1992), (5) Kim & Sanders (1998), (6) Sloan Digital Sky Survey (SDSS; York et al. 2000) DR 1 (Abazajian et al. 2003), (7) Downes et al. (1993), (8) Huchra et al. (1983), (9) Murphy et al. (2001), (10) Hwang et al. (2007), (11) Rothberg & Joseph (2006), (12) Darling & Giovanelli (2006), (13) SDSS DR 6 (Adelman-McCarthy et al. 2008), (14) SDSS DR 4 (Adelman-McCarthy et al. 2006), (15) Carilli et al. (1998), (16) Strauss & Huchra (1988), (17) SDSS DR 3 (Abazajian et al. 2005), (18) Nagar et al. (2003), (19) Lauberts & Valentijn (1989).

^hOptical classification is taken from Armus et al. (1989).

ⁱ3.3 μm PAH emission flux is taken from Imanishi et al. (2010b).

^j*IRAS* fluxes are taken from Kim & Sanders (1998).

^k*IRAS* fluxes are taken from Sanders et al. (2003).

^l*IRAS* fluxes are taken from Sanders et al. (1995).

^mOptical classification is taken from Duc et al. (1997).

ⁿOptical classification is taken from Veilleux et al. (1995).

^oOptical classification is taken from Mirabel et al. (1991).

3.2.2 Spectral Analysis

The near-infrared spectroscopic observations were conducted with the InfraRed Camera (IRC) infrared spectrograph (Onaka et al. 2007) on board the *AKARI* infrared satellite (Murakami et al. 2007). The 1×1 arcmin² window is used to avoid source overlap. The pixel scale of the *AKARI* IRC is $1''.46 \times 1''.46$. We used the NG grism mode (Onaka et al. 2007) to obtain a $2.5\text{--}5.0$ μm spectrum. The NG grism has a dispersion of 9.7×10^{-3} $\mu\text{m pix}^{-1}$ and an effective spectral resolution of $\lambda/\delta\lambda \sim 120$ at 3.6 μm for a point source. We employed the observing mode of IRC04, in which one pointing comprised eight or nine independent frames. Thus, although we assigned only one pointing for each ULIRG, the effects of cosmic-ray hits were removed. The total net on-source exposure time is ~ 6 minutes for each ULIRG.

The data were processed using “IRC Spectroscopy Toolkit Version 20110114,” the standard IDL toolkit prepared for the reduction of *AKARI* IRC spectra (Ohyama et al. 2007). Each frame was dark-subtracted, linearity-corrected, and flat-field-corrected. Wavelength and flux calibrations were also made within this toolkit. The accuracy of wavelength calibration is taken to be ~ 1 pixel or $\sim 10^{-2}$ μm (Ohyama et al. 2007). The accuracy of absolute flux calibration is $\sim 10\%$ at the central wavelength of the spectra, and can be as large as $\sim 20\%$ at the edge of the spectra (Ohyama et al. 2007). We estimated a spatial extent of the object by stacking the spectrum along the spatial direction (i.e., perpendicular to the dispersion direction) for each source. The measured full width at half maximum (FWHM) of the spatial profile is typically $\sim 4\text{--}5$ pixel, which is consistent with the size of the point spread function of *AKARI* IRC in spectroscopic mode (Lorente et al. 2008). We adopted an aperture width of 5 pixel ($= 7''.3$) along the spatial direction for the spectrum extraction for each ULIRG. Smoothing with a boxcar kernel of three pixel in the dispersion direction was applied to each spectrum.

3.2.3 Line Fitting

The Br α line at a rest-frame wavelength of $\lambda_{\text{rest}} = 4.05$ μm was fitted with a linear continuum and a single Gaussian profile in each spectrum. The free parameters are the offset and the slope of the linear continuum, the normalization of the Gaussian profile, and

the central wavelength. The line width is fixed at the spatial width of each object (FWHM $\sim 4\text{--}5$ pixel). Here, we assumed that the spectral resolution is determined by the size of each object because the observations employ slitless spectroscopy, and the intrinsic line widths are narrower than the Δv resolution of $\sim 3000 \text{ km s}^{-1}$. The range of wavelengths used for the fitting was determined to satisfactorily reproduce the continuum emission and is typically $\pm 0.15 \mu\text{m}$ around the central wavelength of the Br α line. The obtained central wavelengths of the Br α lines exhibit small discrepancies from those expected from redshifts. The discrepancy is larger than the fitting error of typically $\sim 10^{-3} \mu\text{m}$ but within the wavelength calibration error of $\sim 10^{-2} \mu\text{m}$ (Ohyama et al. 2007). Therefore, we shifted the wavelength of the entire spectrum so that the best-fit central wavelength of the Br α line matches the redshift. The flux of the Br α line was then calculated by integrating the best-fit Gaussian profile.

3.3 Results

In this section, we present the result of the measurement of the Br α line flux in ULIRGs. We utilize the Br α line luminosity as an indicator of star formation and investigate the effect of heavy dust extinction on the Br α line. We also present the result of a comparison of the Br α line with the total infrared luminosity and the $3.3 \mu\text{m}$ PAH emission.

3.3.1 Resultant Spectra and Br α Line Flux

Figure 3.1 presents an example of $2.5\text{--}5.0 \mu\text{m}$ spectra of ULIRGs obtained with *AKARI* IRC. Among the sample of galaxies, one source, IRAS 17028+5817, has two nuclei. Since the eastern (E) and western (W) nuclei of this galaxy are resolved with *AKARI* IRC, the spectra of the two nuclei are extracted separately. Thus, in total, 51 spectra are obtained from the 50 observations (Tab. 3.1).

Among the 51 spectra, three sources (IRAS 00183–7111, IRAS 04313–1649, and IRAS 10091+4704) have a redshift higher than 0.24, and the Br α line was not observed within the $2.5\text{--}5.0 \mu\text{m}$ wavelength range by *AKARI*. Moreover, the line fitting was not performed for two other sources (IRAS 21477+0502 and IRAS 23129+2548) because their spectra suffer from spectral overlapping with other objects and we were not able to determine the

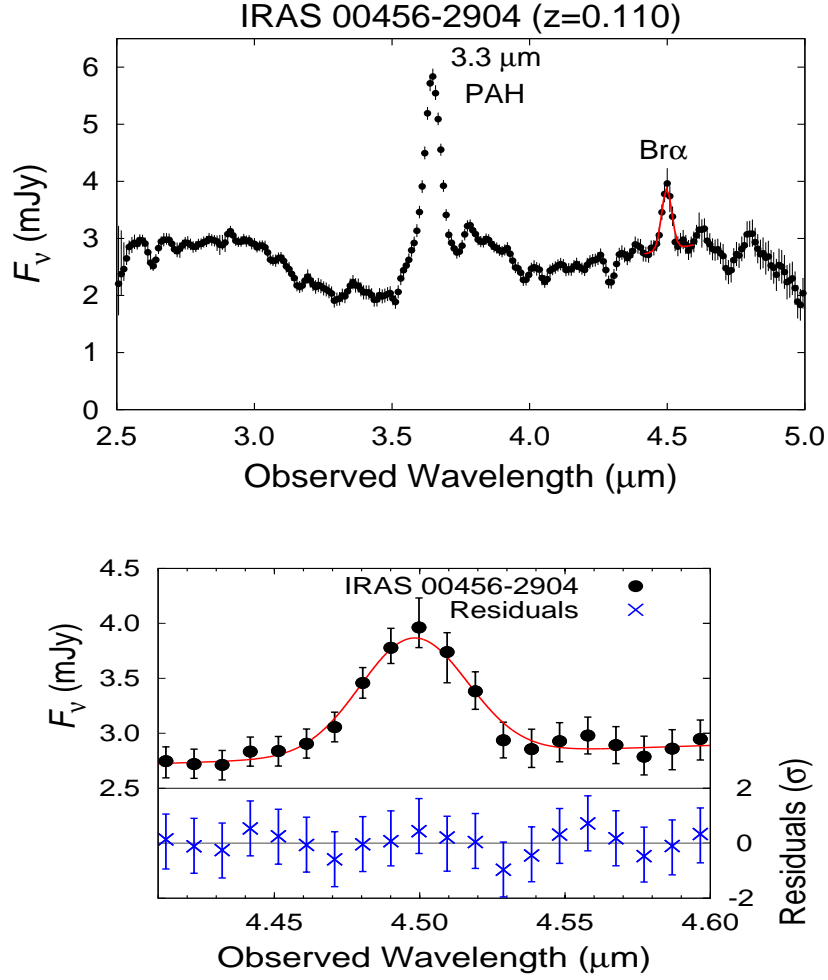


Figure 3.1. Typical example of the *AKARI* IRC 2.5–5.0 μm spectra of ULIRGs. The top panel presents the entire spectrum, while the bottom panel shows a magnification around the $\text{Br}\alpha$ line of the top panel. The best-fit Gaussian profile for the $\text{Br}\alpha$ line is plotted with the red solid line. The residual spectrum of the best fit is also displayed in the bottom panel with the blue crosses.

spatial extent of the targets. We therefore performed the line fitting to 46 objects and detected the $\text{Br}\alpha$ line at the 99% confidence level (2.5σ) in 33 objects. In the remaining 13 objects, we derived 2.5σ upper-limit fluxes of the $\text{Br}\alpha$ line. These upper-limit fluxes are not used in the following discussions. The measured $\text{Br}\alpha$ line fluxes ($F_{\text{Br}\alpha}$) are summarized in Table 3.3. In this chapter, we compare $F_{\text{Br}\alpha}$ with other observations. Thus both the statistical and systematic errors are taken into account for the error estimation of $F_{\text{Br}\alpha}$ shown in Table 3.3.

Table 3.3. Observed Br α Line Flux and Correction for Dust Extinction

Object Name	$F_{\text{Br}\alpha}^{\text{a}}$ ($10^{-15}\text{erg s}^{-1}\text{cm}^{-2}$)	H α /H β^{b}	A_V^{c} (mag)	$C_{\text{Br}\alpha}^{\text{d}}$	Ref. ^e
IRAS 00183–7111	... ^f	2.9 ± 1.0	0.06 ± 0.98	1.002 ± 0.032	1
IRAS 00456–2904	7.32 ± 0.82	6.25 ± 0.31	2.17 ± 0.14	1.074 ± 0.005	2
IRAS 00482–2721	3.53 ± 0.81	9.09 ± 0.45	3.22 ± 0.14	1.111 ± 0.005	2
IRAS 01199–2307	< 4.5	6.67 ± 0.33	2.35 ± 0.14	1.080 ± 0.005	2
IRAS 01298–0744	< 2.2	6.67 ± 0.33	2.35 ± 0.14	1.080 ± 0.005	2
IRAS 01355–1814	< 2.6	6.25 ± 0.31	2.17 ± 0.14	1.074 ± 0.005	2
IRAS 01494–1845	5.04 ± 0.81
IRAS 01569–2939	5.71 ± 0.83	16.67 ± 0.83	4.91 ± 0.14	1.175 ± 0.005	2
IRAS 02480–3745	2.94 ± 0.77
IRAS 03209–0806	5.59 ± 0.87	11.11 ± 0.56	3.78 ± 0.14	1.132 ± 0.005	2
IRAS 03521+0028	2.9 ± 1.2	33.3 ± 8.3	6.85 ± 0.70	1.252 ± 0.023	2
IRAS 04074–2801	< 2.1	9.09 ± 0.45	3.22 ± 0.14	1.111 ± 0.005	2
IRAS 04313–1649	... ^f	16.8 ± 3.5	4.94 ± 0.58	1.176 ± 0.019	3
IRAS 05020–2941	2.08 ± 0.74	6.25 ± 0.31	2.17 ± 0.14	1.074 ± 0.005	2
IRAS 05189–2524	17.4 ± 6.9	8.3 ± 2.1	2.98 ± 0.70	1.103 ± 0.023	2
IRAS 06035–7102	7.1 ± 1.7	13.4 ± 4.4	4.30 ± 0.93	1.151 ± 0.030	4 ^g
IRAS 08572+3915	< 14.9	20.8 ± 1.0	5.52 ± 0.14	1.199 ± 0.005	2 ^h
IRAS 08591+5248	2.61 ± 0.75	6.09 ± 0.88	2.10 ± 0.41	1.071 ± 0.013	5
UGC 5101	< 20.4	17.29 ± 0.95	5.02 ± 0.15	1.179 ± 0.005	5
IRAS 09463+8141	3.00 ± 0.90	25.0 ± 6.3	6.05 ± 0.70	1.219 ± 0.023	2
IRAS 09539+0857	2.11 ± 0.64	10.00 ± 0.50	3.49 ± 0.14	1.121 ± 0.005	2
IRAS 10035+2740	< 2.6	8.5 ± 1.1	3.03 ± 0.35	1.105 ± 0.012	5
IRAS 10091+4704	... ^f	12.50 ± 0.63	4.11 ± 0.14	1.144 ± 0.005	2
IRAS 10494+4424	11.59 ± 0.68	9.09 ± 0.45	3.22 ± 0.14	1.111 ± 0.005	2
IRAS 10594+3818	6.7 ± 1.1	5.88 ± 0.29	2.00 ± 0.14	1.068 ± 0.005	2
IRAS 11028+3130	< 6.7	3.45 ± 0.17	0.51 ± 0.14	1.017 ± 0.005	2
IRAS 11180+1623	< 4.1	10.00 ± 0.50	3.49 ± 0.14	1.121 ± 0.005	2
IRAS 11387+4116	5.16 ± 0.71	12.50 ± 0.63	4.11 ± 0.14	1.144 ± 0.005	2
IRAS 12447+3721	4.73 ± 0.85	5.26 ± 0.26	1.69 ± 0.14	1.057 ± 0.005	2
Mrk 231	< 99.7	5.2 ± 2.2	1.6 ± 1.2	1.055 ± 0.039	6
Mrk 273	38.8 ± 2.3	10.00 ± 0.50	3.49 ± 0.14	1.121 ± 0.005	2
IRAS 13469+5833	5.0 ± 1.2	11.11 ± 0.56	3.78 ± 0.14	1.132 ± 0.005	2
IRAS 13539+2920	12.5 ± 1.6	14.29 ± 0.71	4.48 ± 0.14	1.158 ± 0.005	2
IRAS 14121–0126	3.99 ± 0.87	12.50 ± 0.63	4.11 ± 0.14	1.144 ± 0.005	2
IRAS 14202+2615	7.69 ± 0.90	6.25 ± 0.31	2.17 ± 0.14	1.074 ± 0.005	2
IRAS 14394+5332	7.93 ± 0.76	7.69 ± 0.38	2.75 ± 0.14	1.095 ± 0.005	2
IRAS 15043+5754	1.95 ± 0.50	7.69 ± 0.38	2.75 ± 0.14	1.095 ± 0.005	2
IRAS 16333+4630	4.16 ± 0.92	8.33 ± 0.42	2.98 ± 0.14	1.103 ± 0.005	2
IRAS 16468+5200	< 3.9	9.20 ± 0.35	3.25 ± 0.11	1.113 ± 0.003	2 ^h
IRAS 16487+5447	9.33 ± 0.72	5.00 ± 0.25	1.55 ± 0.14	1.052 ± 0.005	2
IRAS 17028+5817E	2.38 ± 0.74	5.56 ± 0.28	1.84 ± 0.14	1.062 ± 0.005	2
IRAS 17028+5817W	5.15 ± 0.77	14.29 ± 0.71	4.48 ± 0.14	1.158 ± 0.005	2
IRAS 17044+6720	6.7 ± 1.7	7.14 ± 0.36	2.55 ± 0.14	1.087 ± 0.005	2
IRAS 17068+4027	8.79 ± 0.95	12.50 ± 0.63	4.11 ± 0.14	1.144 ± 0.005	2

Table 3.3. (continued)

Object Name	$F_{\text{Br}\alpha}^{\text{a}}$ ($10^{-15}\text{erg s}^{-1}\text{cm}^{-2}$)	$\text{H}\alpha/\text{H}\beta^{\text{b}}$	A_V^{c} (mag)	$C_{\text{Br}\alpha}^{\text{d}}$	Ref. ^e
IRAS 17179+5444	4.0 ± 1.1	10.00 ± 0.50	3.49 ± 0.14	1.121 ± 0.005	2
IRAS 19254-7245	15.7 ± 2.5	9.8 ± 1.6	3.43 ± 0.45	1.119 ± 0.015	1
IRAS 21477+0502	... ⁱ	5.88 ± 0.29	2.00 ± 0.14	1.068 ± 0.005	2
IRAS 22088-1831	< 2.2	4.76 ± 0.24	1.41 ± 0.14	1.047 ± 0.005	2
IRAS 23128-5919	64.2 ± 1.5	7.95 ± 0.80	2.85 ± 0.28	1.098 ± 0.009	4 ^h
IRAS 23129+2548	... ⁱ	12.50 ± 0.63	4.11 ± 0.14	1.144 ± 0.005	2
IRAS 23498+2423	< 3.3	7.14 ± 0.36	2.55 ± 0.14	1.087 ± 0.005	2

^aObserved Br α line flux obtained with our *AKARI* result. The values are different from those in Table 4.3 because of the difference of the version of the toolkit used for the data reduction and the revision of the error estimation in Chapter 4.

^bFlux ratio of H α and H β lines taken from the literature.

^cVisual extinction derived from the H α /H β line ratio.

^dCorrection factor for dust extinction for the Br α line flux.

^eReferences for optical line fluxes: (1) Buchanan et al. (2006), (2) Veilleux et al. (1999a), (3) Rupke et al. (2008), (4) Duc et al. (1997), (5) Hou et al. (2009), (6) Lipari et al. (1994).

^fThe redshift is larger than 0.24, and the Br α line is not observed in the wavelength range 2.5–5.0 μm .

^gValue for the W nucleus.

^hSum of two nuclei.

ⁱSpectrum suffered from source overlapping.

3.3.2 Effect of Dust Extinction on the Br α Line

In the standard extinction curve (e.g., Draine 2003), dust extinction is lower at longer wavelengths. Thus the Br α line is less affected by dust extinction owing to its infrared wavelength (4.05 μm) than the optical Balmer lines and even the infrared Pa α and Br γ lines (~ 2 μm) widely observed from the ground. Furthermore, from observations of the Galactic center, Fritz et al. (2011) recently showed that extinction at 4 μm was about the same as that at ~ 7 –8 μm ($A_{7.5\mu\text{m}}/A_{4\mu\text{m}} \sim 0.8$, where A_λ is extinction in magnitude at a wavelength λ) and was even lower than that at ~ 9 –20 μm ($A_{12.4\mu\text{m}}/A_{4\mu\text{m}} \sim 1.3$). This means that the effect of dust extinction on the Br α line is compatible with (or even lower than) that on other indicators of star formation in the mid-infrared wavelengths such as the 7.7 μm PAH feature or the [Ne II] 12.8 μm line widely observed with *Spitzer* (e.g., Veilleux et al. 2009). Thus we conclude that the Br α line is one of the best tracers of star

formation in the near- to mid-infrared wavelength range. However, especially in ULIRGs, which harbor vast amounts of dust, dust extinction could pose a problem even if we use the Br α line.

The optical H α /H β line ratio is widely used as an indicator of extinction (e.g., Kim et al. 1998). The H α /H β line ratio taken from the literature and the inferred visual extinction in our sample are summarized in Table 3.3. We assume an intrinsic line ratio for H α /H β of 2.87 (Osterbrock & Ferland 2006, case B with $T = 10000$ K and the low-density limit). The Milky Way dust model of Draine (2003) is used for the extinction law ($A_{\text{H}\alpha} = 0.776A_V$, $A_{\text{H}\beta} = 1.17A_V$, and $A_{\text{Br}\alpha} = 3.56 \times 10^{-2}A_V$). The extinction-corrected luminosity of the Br α line ($L_{\text{Br}\alpha}$) is summarized in Table 3.4.

The visual extinction derived from the optical H α /H β line ratio is typically a few magnitudes, and the correction factor for the flux of the Br α line, $C_{\text{Br}\alpha}$, is at most ~ 1.3 (Table 3.3). If dust obscuration of starburst in these ULIRGs is so heavy, however, optical observations would trace only the outer region of the obscured starburst, and the visual extinction derived from the H α /H β line ratio would be regarded as a kind of lower limit. For instance, Genzel et al. (1998) reported visual extinction of 5–50 mag in ULIRGs based on the mid-infrared spectroscopic observations from *ISO*. Here we discuss the uncertainty arising from such heavy dust obscuration.

With our *AKARI* result, we are able to estimate visual extinction using the Br β line ($\mathcal{N} = 6 \rightarrow 4$, $\lambda_{\text{rest}} = 2.63 \mu\text{m}$) observed simultaneously with the Br α line, although it is difficult to measure the flux of the Br β line because of its faintness. In one source among our sample, IRAS 00456–2904 (Figure 3.1), we marginally detect the Br β line and measure its flux to be $(2.3 \pm 1.0) \times 10^{-15} \text{ erg s}^{-1} \text{ cm}^{-2}$. This yields the Br β /Br α line ratio of 0.31 ± 0.15 . Adopting an intrinsic line ratio for Br β /Br α of 0.57 (Osterbrock & Ferland 2006) and $A_{\text{Br}\beta} = 8.09 \times 10^{-2}A_V$ (Draine 2003), we derive visual extinction of 14 ± 11 mag from the Br β /Br α line ratio. This corresponds to a correction factor for the flux of the Br α line of 1.6 ± 0.5 . Thus, in this source, extinction heavier than that derived from the H α /H β line ratio ($A_V = 2.17 \pm 0.14$ mag) is indicated.

Table 3.4. Luminosity of Br α Lines

Object Name	$L_{\text{Br}\alpha}^{\text{a}}$ ($10^7 L_{\odot}$)	$L_{\text{Br}\alpha}/L_{\text{IR}}$ (10^{-5})
IRAS 00183–7111
IRAS 00456–2904	6.32 ± 0.71	4.50 ± 0.51
IRAS 00482–2721	4.5 ± 1.0	3.83 ± 0.88
IRAS 01199–2307	< 8.4	< 6.9
IRAS 01298–0744	< 3.1	< 1.9
IRAS 01355–1814	< 7.7	< 2.7
IRAS 01494–1845	8.9 ± 1.4	5.21 ± 0.84
IRAS 01569–2939	9.1 ± 1.3	7.2 ± 1.1
IRAS 02480–3745	5.7 ± 1.5	4.0 ± 1.0
IRAS 03209–0806	12.6 ± 2.0	7.1 ± 1.1
IRAS 03521+0028	5.9 ± 2.4	1.78 ± 0.71
IRAS 04074–2801	< 3.9	< 2.6
IRAS 04313–1649
IRAS 05020–2941	3.8 ± 1.3	2.10 ± 0.75
IRAS 05189–2524	2.10 ± 0.84	1.35 ± 0.54
IRAS 06035–7102	3.28 ± 0.78	1.96 ± 0.47
IRAS 08572+3915	< 3.7	< 2.7
IRAS 08591+5248	4.9 ± 1.4	3.26 ± 0.94
UGC 5101	< 2.2	< 2.1
IRAS 09463+8141	6.3 ± 1.9	3.5 ± 1.0
IRAS 09539+0857	2.68 ± 0.81	4.3 ± 1.3
IRAS 10035+2740	< 5.7	< 3.2
IRAS 10091+4704
IRAS 10494+4424	7.08 ± 0.42	4.80 ± 0.28
IRAS 10594+3818	12.6 ± 2.1	7.2 ± 1.2
IRAS 11028+3130	< 20.0	< 8.1
IRAS 11180+1623	< 9.0	< 5.0
IRAS 11387+4116	9.1 ± 1.3	7.22 ± 0.99
IRAS 12447+3721	8.8 ± 1.6	8.7 ± 1.6
Mrk 231	< 11.3	< 2.9
Mrk 273	3.72 ± 0.22	2.88 ± 0.17
IRAS 13469+5833	10.0 ± 2.3	7.0 ± 1.6
IRAS 13539+2920	11.3 ± 1.4	9.9 ± 1.2
IRAS 14121–0126	7.2 ± 1.6	3.93 ± 0.86
IRAS 14202+2615	14.8 ± 1.7	6.73 ± 0.79
IRAS 14394+5332	6.26 ± 0.60	4.47 ± 0.43
IRAS 15043+5754	3.40 ± 0.87	2.63 ± 0.67
IRAS 16333+4630	12.4 ± 2.7	4.35 ± 0.97

Table 3.4. (continued)

Object Name	$L_{\text{Br}\alpha}^{\text{a}}$ ($10^7 L_{\odot}$)	$L_{\text{Br}\alpha}/L_{\text{IR}}$ (10^{-5})
IRAS 16468+5200	< 6.8	< 6.4
IRAS 16487+5447	6.97 ± 0.54	5.67 ± 0.44
IRAS 17028+5817	6.32 ± 0.88	4.45 ± 0.62
(E nucleus)	1.88 ± 0.59	...
(W nucleus)	4.44 ± 0.66	...
IRAS 17044+6720	9.1 ± 2.3	5.3 ± 1.4
IRAS 17068+4027	23.4 ± 2.5	11.5 ± 1.2
IRAS 17179+5444	6.8 ± 1.9	3.34 ± 0.92
IRAS 19254-7245	4.16 ± 0.66	2.71 ± 0.43
IRAS 21477+0502
IRAS 22088-1831	< 4.8	< 2.7
IRAS 23128-5919	8.49 ± 0.22	8.17 ± 0.21
IRAS 23129+2548
IRAS 23498+2423	< 12.1	< 3.8

^aLuminosity of the Br α line ($L_{\text{Br}\alpha}$). Dust extinction is corrected with the H α /H β line ratio.

To investigate the effect of heavy dust extinction with the entire sample, we focus on the optical depth of the 9.7 μm silicate absorption feature ($\tau_{9.7}$) derived from the *Spitzer* observations. Owing to the mid-infrared wavelength, the 9.7 μm silicate absorption feature can probe dust extinction in heavily obscured regions. Table 3.5 summarizes $\tau_{9.7}$ taken from the literature (references are also listed therein). We convert $\tau_{9.7}$ to visual extinction $A_V^{9.7}$ using the following relation: $A_V^{9.7} (\text{mag}) = (1.08/0.087)\tau_{9.7}$ (Imanishi et al. 2007). We regard $A_V^{9.7}$ as the most extreme extinction in the sample. The mean value of $A_V^{9.7}$ is ~ 23 mag in our sample. This corresponds to the correction factor for a flux of the Br α line of ~ 2.1 . Thus the effect of heavy dust extinction on the Br α line flux is about a factor of two even in the extreme cases.

Table 3.5. Luminosity of 3.3 μm PAH Emission and 9.7 μm Silicate Absorption

Object Name	$\tau_{9.7}^{\text{a}}$	$A_V^{9.7\text{b}}$ (mag)	$L_{3.3}^{\text{c}}$ ($10^8 L_\odot$)	$L_{3.3}/L_{\text{IR}}$ (10^{-4})	Ref. ^d
IRAS 00183–7111	3.1 ± 0.16	38.5 ± 1.9	< 16.6	< 2.19	1
IRAS 00456–2904	1.2 ± 0.12	14.9 ± 1.5	3.6 ± 1.1	2.55 ± 0.77	2
IRAS 00482–2721	2.1 ± 0.11	26.1 ± 1.3	1.73 ± 0.52	1.49 ± 0.45	2
IRAS 01199–2307	2.4 ± 0.12	29.8 ± 1.5	1.55 ± 0.46	1.27 ± 0.38	3
IRAS 01298–0744	4.0 ± 0.20	49.7 ± 2.5	2.44 ± 0.73	1.51 ± 0.45	2
IRAS 01355–1814	2.4 ± 0.12	29.8 ± 1.5	1.82 ± 0.55	0.65 ± 0.19	3
IRAS 01494–1845	1.6 ± 0.16	19.9 ± 2.0	3.9 ± 1.2	2.28 ± 0.68	3
IRAS 01569–2939	2.8 ± 0.14	34.8 ± 1.7	3.11 ± 0.93	2.46 ± 0.74	2
IRAS 02480–3745	1.4 ± 0.14	17.4 ± 1.7	2.92 ± 0.88	2.04 ± 0.61	4
IRAS 03209–0806	1.0 ± 0.10	12.4 ± 1.2	5.3 ± 1.6	2.96 ± 0.89	4
IRAS 03521+0028	1.3 ± 0.13	16.1 ± 1.6	5.0 ± 1.5	1.50 ± 0.45	3
IRAS 04074–2801	3.0 ± 0.15	37.3 ± 1.9	1.75 ± 0.53	1.19 ± 0.36	4
IRAS 04313–1649	2.8 ± 0.14	34.8 ± 1.7	< 3.0	< 0.82	3
IRAS 05020–2941	2.4 ± 0.12	29.8 ± 1.5	1.87 ± 0.56	1.05 ± 0.31	4
IRAS 05189–2524	0.3 ± 0.02	3.92 ± 0.21	3.8 ± 1.1	2.45 ± 0.74	5
IRAS 06035–7102	2.9 ± 0.15	36.0 ± 1.8	5.6 ± 1.7	3.3 ± 1.0	1
IRAS 08572+3915	3.8 ± 0.19	47.2 ± 2.4	< 1.2	< 0.84	2
IRAS 08591+5248	1.0 ± 0.10	12.4 ± 1.2	2.72 ± 0.82	1.81 ± 0.54	4
UGC 5101	1.6 ± 0.08	20.1 ± 1.0	2.68 ± 0.80	2.55 ± 0.77	5
IRAS 09463+8141	2.0 ± 0.20	24.8 ± 2.5	5.1 ± 1.5	2.82 ± 0.85	2
IRAS 09539+0857	3.5 ± 0.18	43.5 ± 2.1	1.61 ± 0.48	2.59 ± 0.78	2
IRAS 10035+2740	2.0 ± 0.20	24.8 ± 2.5	3.18 ± 0.96	1.79 ± 0.54	3
IRAS 10091+4704	2.5 ± 0.13	31.0 ± 1.6	4.1 ± 1.2	1.17 ± 0.35	3
IRAS 10494+4424	1.7 ± 0.17	21.1 ± 2.1	2.32 ± 0.70	1.57 ± 0.47	2
IRAS 10594+3818	1.0 ± 0.10	12.4 ± 1.2	5.1 ± 1.5	2.91 ± 0.87	4
IRAS 11028+3130	2.5 ± 0.13	31.0 ± 1.6	1.81 ± 0.54	0.73 ± 0.22	3
IRAS 11180+1623	2.0 ± 0.20	24.8 ± 2.5	1.17 ± 0.35	0.65 ± 0.19	3
IRAS 11387+4116	1.1 ± 0.11	13.7 ± 1.4	3.6 ± 1.1	2.84 ± 0.85	2
IRAS 12447+3721	1.7 ± 0.17	21.1 ± 2.1	2.50 ± 0.75	2.46 ± 0.74	4
Mrk 231	0.6 ± 0.03	7.98 ± 0.43	8.9 ± 2.7	2.29 ± 0.70	5
Mrk 273	1.7 ± 0.09	21.7 ± 1.1	2.52 ± 0.76	1.95 ± 0.58	5
IRAS 13469+5833	1.7 ± 0.17	21.1 ± 2.1	2.97 ± 0.89	2.08 ± 0.62	3
IRAS 13539+2920	1.6 ± 0.16	19.9 ± 2.0	4.2 ± 1.3	3.7 ± 1.1	2
IRAS 14121–0126	1.3 ± 0.13	16.1 ± 1.6	5.6 ± 1.7	3.05 ± 0.92	4
IRAS 14202+2615	0.7 ± 0.07	8.69 ± 0.86	8.3 ± 2.5	3.8 ± 1.1	4
IRAS 14394+5332	5.1 ± 1.5	3.7 ± 1.1	...
IRAS 15043+5754	1.4 ± 0.14	17.4 ± 1.7	3.6 ± 1.1	2.81 ± 0.84	4
IRAS 16333+4630	1.3 ± 0.13	16.1 ± 1.6	6.5 ± 2.0	2.31 ± 0.69	3

Table 3.5. (continued)

Object Name	$\tau_{9.7}^a$	$A_V^{9.7b}$ (mag)	$L_{3.3}^c$ ($10^8 L_\odot$)	$L_{3.3}/L_{\text{IR}}$ (10^{-4})	Ref. ^d
IRAS 16468+5200	2.5 ± 0.13	31.0 ± 1.6	1.11 ± 0.33	1.04 ± 0.31	2
IRAS 16487+5447	1.8 ± 0.18	22.4 ± 2.2	2.53 ± 0.76	2.06 ± 0.62	2
IRAS 17028+5817	1.5 ± 0.15	18.6 ± 1.9	3.38 ± 0.92	2.38 ± 0.65	2
(E Nucleus)	0.33 ± 0.10
(W Nucleus)	3.06 ± 0.92
IRAS 17044+6720	1.8 ± 0.18	22.4 ± 2.2	3.26 ± 0.98	1.91 ± 0.57	2
IRAS 17068+4027	1.8 ± 0.18	22.4 ± 2.2	6.3 ± 1.9	3.07 ± 0.92	3
IRAS 17179+5444	2.15 ± 0.64	1.06 ± 0.32	...
IRAS 19254-7245	1.3 ± 0.07	16.7 ± 0.9	1.06 ± 0.32	0.69 ± 0.21	5
IRAS 21477+0502	0.8 ± 0.08	9.9 ± 1.0	1.39 ± 0.42	0.64 ± 0.19	4
IRAS 22088-1831	2.6 ± 0.13	32.3 ± 1.6	< 4.5	< 2.6	4
IRAS 23128-5919	4.4 ± 1.3	4.3 ± 1.3	...
IRAS 23129+2548	2.6 ± 0.13	32.3 ± 1.6	< 1.1	< 0.60	3
IRAS 23498+2423	0.6 ± 0.03	7.48 ± 0.36	< 7.3	< 2.3	6

^aOptical depth of the 9.7 μm silicate absorption.

^bVisual extinction derived from $\tau_{9.7}$.

^cLuminosity of the 3.3 μm PAH emission. Dust extinction is corrected using the $\text{H}\alpha/\text{H}\beta$ ratio.

^dReferences for $\tau_{9.7}$: (1) Dartois & Muñoz-Caro (2007), (2) Imanishi et al. (2007), (3) Imanishi (2009), (4) Imanishi et al. (2010a), (5) Wu et al. (2009), (6) Willett et al. (2011).

In summary, taking the effect of heavy dust extinction into account, we conclude that the intrinsic $\text{Br}\alpha$ line flux is determined within an uncertainty of underestimation by a factor of two. Allowing for this uncertainty, we adopt and apply the correction for dust extinction estimated from the $\text{H}\alpha/\text{H}\beta$ line ratio to the $\text{Br}\alpha$ line flux as the minimum correction because the $\text{H}\alpha/\text{H}\beta$ line ratio is available for all our targets. At least half the ionizing photons that originate from dust-obscured regions are expected to be traced by the $\text{Br}\alpha$ line, and thus we utilize the luminosity of the $\text{Br}\alpha$ line as a good indicator of star formation.

3.3.3 Comparison to Other Indicators of Star Formation

The total infrared luminosity is widely used as an indicator of star formation in star-forming galaxies where AGNs do not contaminate the luminosity (e.g., Kennicutt & Evans 2012). Thus we expect that $L_{\text{Br}\alpha}$ is correlated with L_{IR} if L_{IR} is governed solely by star formation. Here we compare $L_{\text{Br}\alpha}$ with L_{IR} . We note that the statistical uncertainty of L_{IR} arising from the measurement uncertainty of the *IRAS* fluxes is a few percent (Moshir et al. 1992), and the systematic one of L_{IR} caused by the conversion of the *IRAS* fluxes into L_{IR} is less than 5% (Dale & Helou 2002). The uncertainty of L_{IR} is much smaller than that of $L_{\text{Br}\alpha}$, which is typically $> 10\%$ of its luminosity as shown in Table 3.4. We regard that the uncertainty of L_{IR} has almost no impact on the following discussions.

The top panel of Figure 3.2 shows the comparison of $L_{\text{Br}\alpha}$ with L_{IR} for the 33 objects in which the $\text{Br}\alpha$ line is detected. We find that the galaxies do not follow a single relation and show a scatter in this plot. The correlation coefficient between L_{IR} and $L_{\text{Br}\alpha}$ is calculated to be 0.116, which yields the probability of obtaining such a correlation coefficient by chance of 52.6%. This indicates no significant correlation between them.

Within the spectral window of our *AKARI* observation, the $3.3 \mu\text{m}$ PAH emission, which traces UV photons from OB stars and is also expected to be used as an indicator of star formation, is observed simultaneously with the $\text{Br}\alpha$ line. Although complex emission mechanisms make it difficult to quantitatively connect the $3.3 \mu\text{m}$ PAH emission luminosity ($L_{3.3}$) with the number of ionizing photons, we also expect a correlation between $L_{3.3}$ and $L_{\text{Br}\alpha}$.

The top panel of Figure 3.3 shows the relation between $L_{3.3}$ and $L_{\text{Br}\alpha}$. We use $L_{3.3}$ listed in Table 3.5. Dust extinction is corrected for $L_{3.3}$ using the $\text{H}\alpha/\text{H}\beta$ line ratio. Extinction at the wavelength of the $3.3 \mu\text{m}$ PAH emission is assumed to be $A_{3.3} = 5.32 \times 10^{-2} A_V$ (Draine 2003). In contrast to the comparison of $L_{\text{Br}\alpha}$ with L_{IR} , $L_{3.3}$ and $L_{\text{Br}\alpha}$ are well correlated with each other, regardless of the optical classifications of the galaxies. The correlation coefficient between $L_{3.3}$ and $L_{\text{Br}\alpha}$ is calculated to be 0.659 for a sample size of 33. The probability of obtaining such a correlation coefficient by chance is less than 10^{-4} . We regard this correlation as statistically significant. We also examine the comparison of fluxes, $F_{3.3}$ and $F_{\text{Br}\alpha}$, in the bottom panel of Figure 3.3 to investigate a possible correlation

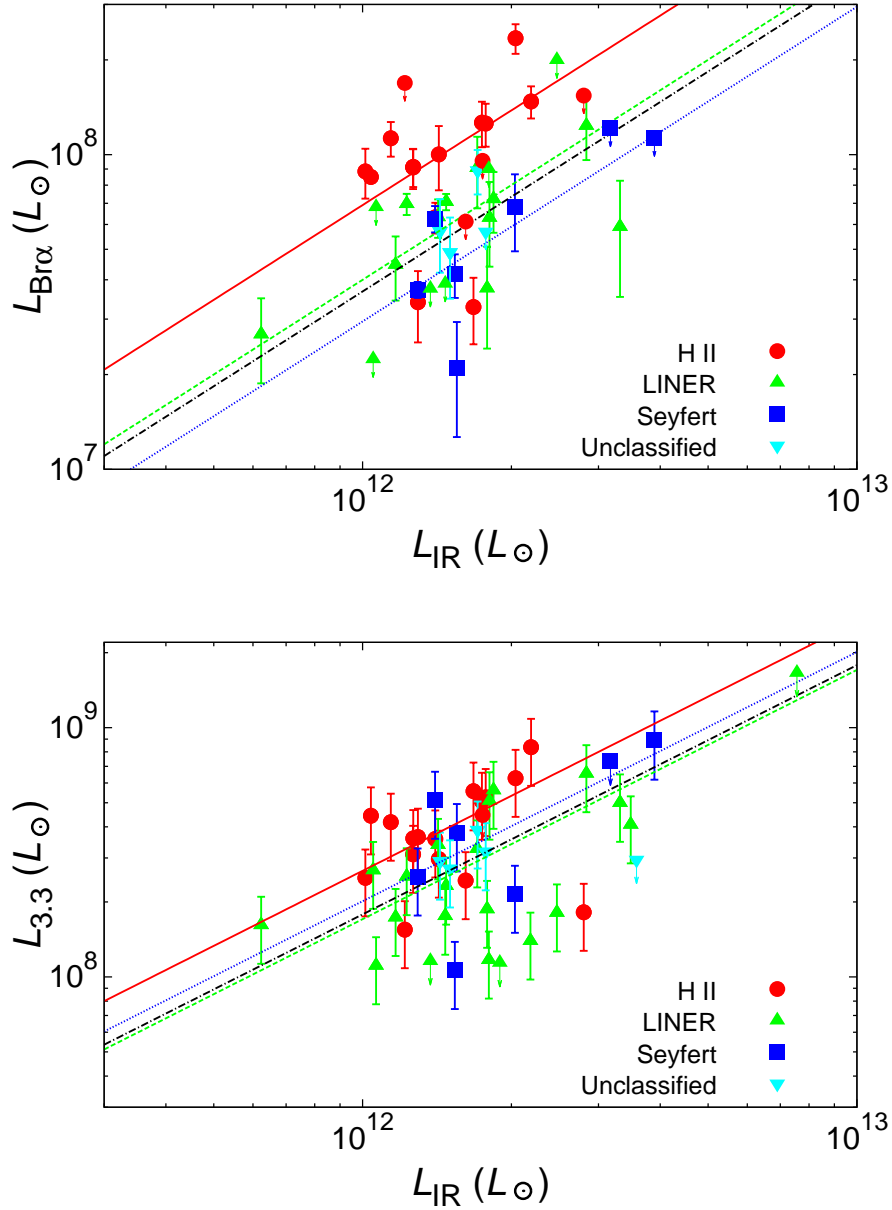


Figure 3.2. Comparison of the Br α line luminosity ($L_{\text{Br}\alpha}$; top) and the 3.3 μm PAH emission luminosity ($L_{3.3}$; bottom) with the total infrared luminosity (L_{IR}). The symbols and colors represent the optical classifications of the galaxy. The red solid, green dashed, blue dotted, and black dashed-dotted lines indicate the mean $L_{\text{Br}\alpha}/L_{\text{IR}}$ ($L_{3.3}/L_{\text{IR}}$) ratio for H II galaxies, LINERs, Seyferts, and the combination of LINERs and Seyferts, respectively. The figures are modified from those of Yano et al. (2016) to include galaxies with a 2.5σ upper-limit of $L_{\text{Br}\alpha}$ or $L_{3.3}$.

introduced by redshift in the luminosity comparison. The correlation coefficient between $F_{3.3}$ and $F_{\text{Br}\alpha}$ is 0.917, and the probability of obtaining this value by chance is well below 10^{-4} . Thus we conclude that the correlation between the $3.3 \mu\text{m}$ PAH emission and the $\text{Br}\alpha$ line is not affected by redshift and is real.

The result of the correlation between $L_{3.3}$ and $L_{\text{Br}\alpha}$ indicates that they trace the same excitation sources, i.e., star formation. If the broad-line region of AGNs contributes to line fluxes, hydrogen lines would have an FWHM of a few thousand km s^{-1} (Osterbrock & Ferland 2006). However, the width of the $\text{Br}\alpha$ line is consistent with the spectral resolution ($\Delta v \sim 3000 \text{ km s}^{-1}$) in all targets within a fitting uncertainty of $\leq 100 \text{ km s}^{-1}$. This indicates that none of the objects shows a broad component of the $\text{Br}\alpha$ line with an FWHM broader than $\sim 1000 \text{ km s}^{-1}$. Combining the absence of the broad component of the $\text{Br}\alpha$ line and the correlation between $L_{\text{Br}\alpha}$ and $L_{3.3}$, we assume that the $\text{Br}\alpha$ line and the $3.3\mu\text{m}$ PAH emission are entirely produced by star formation. The absence of a correlation between $L_{\text{Br}\alpha}$ and L_{IR} then indicates that L_{IR} has a contribution from energy sources other than star formation, i.e., AGNs, in our sample. Thus we conclude that we are able to investigate the contribution of starburst as the dust-enshrouded energy source in ULIRGs by comparing $L_{\text{Br}\alpha}$ with L_{IR} .

The $3.3 \mu\text{m}$ PAH emission, which is stronger than the $\text{Br}\alpha$ line, is detected in almost all our targets, even in the objects in which the $\text{Br}\alpha$ line is not observed (Tab. 3.2). Therefore, we calibrate $L_{3.3}$ with $L_{\text{Br}\alpha}$ to quantitatively investigate star formation in the objects with no $\text{Br}\alpha$ line detected. From the correlation between $L_{3.3}$ and $L_{\text{Br}\alpha}$, we assume a proportionality between them. The mean $L_{\text{Br}\alpha}/L_{3.3}$ ratio is calculated as

$$L_{\text{Br}\alpha}/L_{3.3} = 0.177 \pm 0.003. \quad (3.1)$$

This relation quantitatively associates $L_{3.3}$ with the number of ionizing photons from OB stars. Thus we utilize $L_{3.3}$ as a quantitative indicator of star formation for galaxies in which the $\text{Br}\alpha$ line is not detected.

When using the $3.3 \mu\text{m}$ PAH emission as a proxy for star formation, Kim et al. (2012) pointed out a caveat that $L_{3.3}/L_{\text{IR}}$ decreases as L_{IR} increases within an infrared luminosity range of $10^{10}L_{\odot} < L_{\text{IR}} < 10^{13}L_{\odot}$, and thus the power of $L_{3.3}$ as an indicator of star

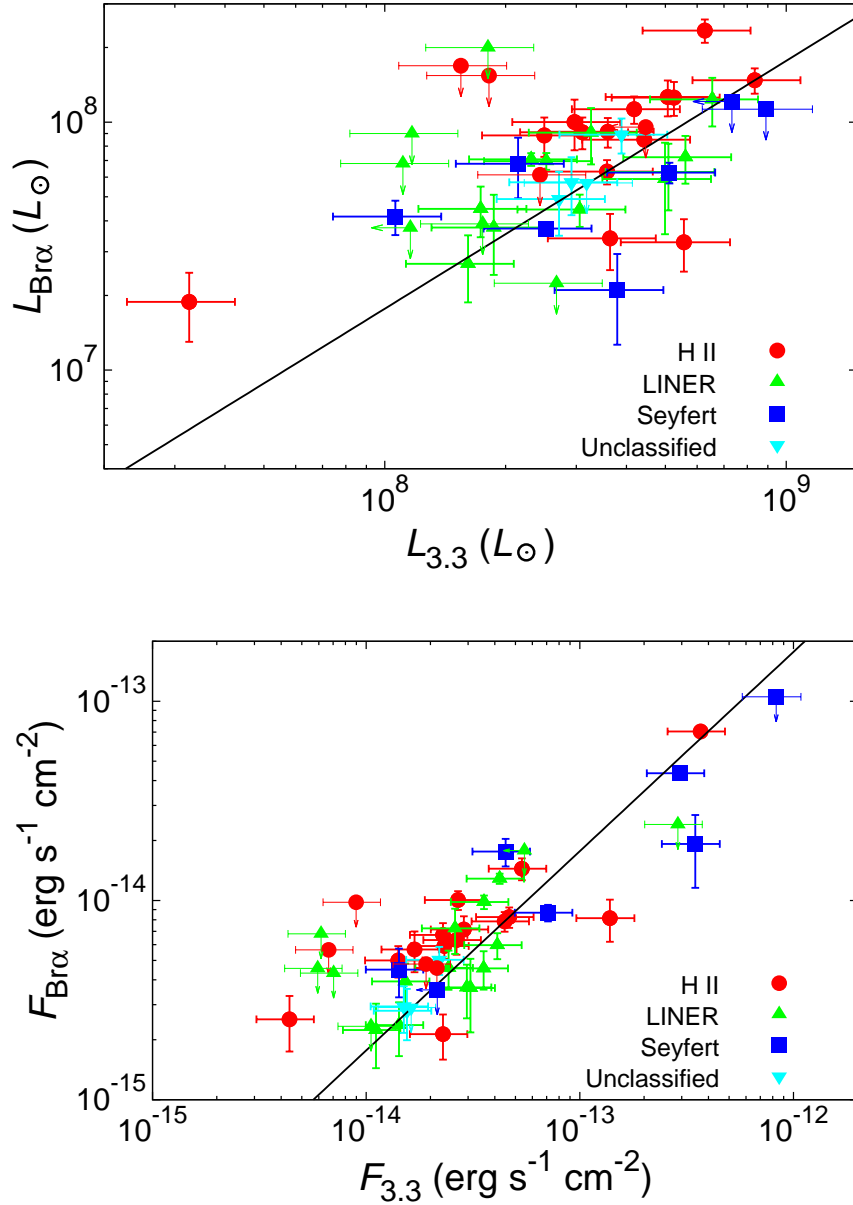


Figure 3.3. Comparison of the Br α line with the 3.3 μ m PAH emission. The top panel shows the comparison of the luminosities, while the bottom panel presents the comparison of the fluxes. The symbols and colors represent the optical classifications of the galaxy. The solid line shows the mean $L_{\text{Br}\alpha}/L_{3.3}$ ($F_{\text{Br}\alpha}/F_{3.3}$) ratio of 0.177 ± 0.003 . The figures are modified from those of Yano et al. (2016) to include galaxies with a 2.5σ upper-limit flux of the Br α line or the 3.3 μ m PAH emission.

formation may be hampered in ULIRGs. This deficit of $L_{3.3}$ was found even if the sources likely to be contaminated by AGN activity are excluded (Yamada et al. 2013). However, we obtain a clear correlation between $L_{3.3}$ and $L_{\text{Br}\alpha}$. We attribute this result to the narrowness of the infrared luminosity range of our sample (most of them lie within $10^{12}L_{\odot} < L_{\text{IR}} < 10^{12.5}L_{\odot}$). The infrared luminosity of the objects where the Br α line is not detected is also in this luminosity range, and hence we assume that the proportionality of Equation (3.1) is also valid for these objects.

The bottom panel of Figure 3.2 shows the comparison of $L_{3.3}$ with L_{IR} . The number of samples is increased from 33 in the comparison of $L_{\text{Br}\alpha}$ with L_{IR} in the top panel to 46 with the use of the 3.3 μm PAH emission. In this larger sample, we again find that galaxies show a significant scatter. The correlation coefficient between L_{IR} and $L_{3.3}$ is calculated to be 0.161, yielding the probability of obtaining such a correlation coefficient by chance of 29.7%. The correlation between L_{IR} and $L_{3.3}$ is not significant, and neither is that between L_{IR} and $L_{\text{Br}\alpha}$. We discuss the origin of these scatters in the next section.

3.4 Discussion

In §3.3, we utilize the luminosities of the Br α line and the 3.3 μm PAH emission as indicators of star formation. Using these indicators, we discuss the contribution of starburst to the total energy from ULIRGs.

3.4.1 Starburst Contribution

The optical classifications of ULIRGs are mainly based on the ratios of optical emission line (Baldwin et al. 1981) and reflect a qualitative difference in the energy sources, while they contain little quantitative information. We investigate the fractional contribution of starburst to the total infrared luminosity with the $L_{\text{Br}\alpha}/L_{\text{IR}}$ and $L_{3.3}/L_{\text{IR}}$ ratios and discuss the quantitative difference of the energy sources among the galaxies with different optical classifications.

Table 3.6. Statistical Tests for $L_{\text{Br}\alpha}/L_{\text{IR}}$ and $L_{3.3}/L_{\text{IR}}$

Optical Class	Probability for $L_{\text{Br}\alpha}/L_{\text{IR}}$		Probability for $L_{3.3}/L_{\text{IR}}$	
	Same Population (K-S Test)	Same Mean (t Test)	Same Population (K-S Test)	Same Mean (t Test)
H II vs. LINER	6.5×10^{-4}	2.4×10^{-3}	1.1×10^{-2}	2.8×10^{-3}
H II vs. Seyfert	4.1×10^{-3}	5.6×10^{-3}	6.2×10^{-2}	1.8×10^{-1}
LINER vs. Seyfert	8.5×10^{-2}	1.2×10^{-1}	8.1×10^{-1}	4.5×10^{-1}
H II vs. LINER & Seyfert	1.4×10^{-4}	9.0×10^{-4}	4.0×10^{-3}	3.7×10^{-3}

3.4.1.1 Difference among Galaxies with Different Optical Classifications

Focusing on the optical classifications of the galaxies, we find a trend that the galaxies classified as LINERs or Seyferts are distributed lower than those classified as H II galaxies in both the panels of Figure 3.2. This indicates that LINERs and Seyferts have lower $L_{\text{Br}\alpha}/L_{\text{IR}}$ and $L_{3.3}/L_{\text{IR}}$ ratios than H II galaxies. Here we discuss the significance of these differences.

The top panel of Figure 3.4 compares a distribution of the $L_{\text{Br}\alpha}/L_{\text{IR}}$ ratio for H II galaxies, LINERs, and Seyferts. The distributions of LINERs and Seyferts are similar to each other, while that of H II galaxies clearly deviates from the other two. To investigate whether the difference in the $L_{\text{Br}\alpha}/L_{\text{IR}}$ ratio is statistically significant, we performed the Kolmogorov–Smirnov (K–S) test between the galaxies with different optical classifications. The K–S test probabilities that the two sets of samples originate from the same population are summarized in Table 3.6. The K–S probability between LINERs and Seyferts is 8.5×10^{-2} and indicates no significant difference between them. On the other hand, H II galaxies show a probability of less than 5×10^{-3} against LINERs or Seyferts. If we combine LINERs and Seyferts, the probability that H II galaxies and the others are drawn from the same population is 1.4×10^{-4} . This difference is statistically significant, and we conclude that the $L_{\text{Br}\alpha}/L_{\text{IR}}$ ratio is statistically different between H II galaxies and LINERs/Seyferts.

The bottom panel of Figure 3.4 is the same as the top panel, but for the $L_{3.3}/L_{\text{IR}}$ ratio with the larger sample. The distribution of H II galaxies again deviates from the two other classifications. We performed the K–S test for the $L_{3.3}/L_{\text{IR}}$ ratio in the same way as for the $L_{\text{Br}\alpha}/L_{\text{IR}}$ ratio and summarize the K–S probabilities for the $L_{3.3}/L_{\text{IR}}$ ratio

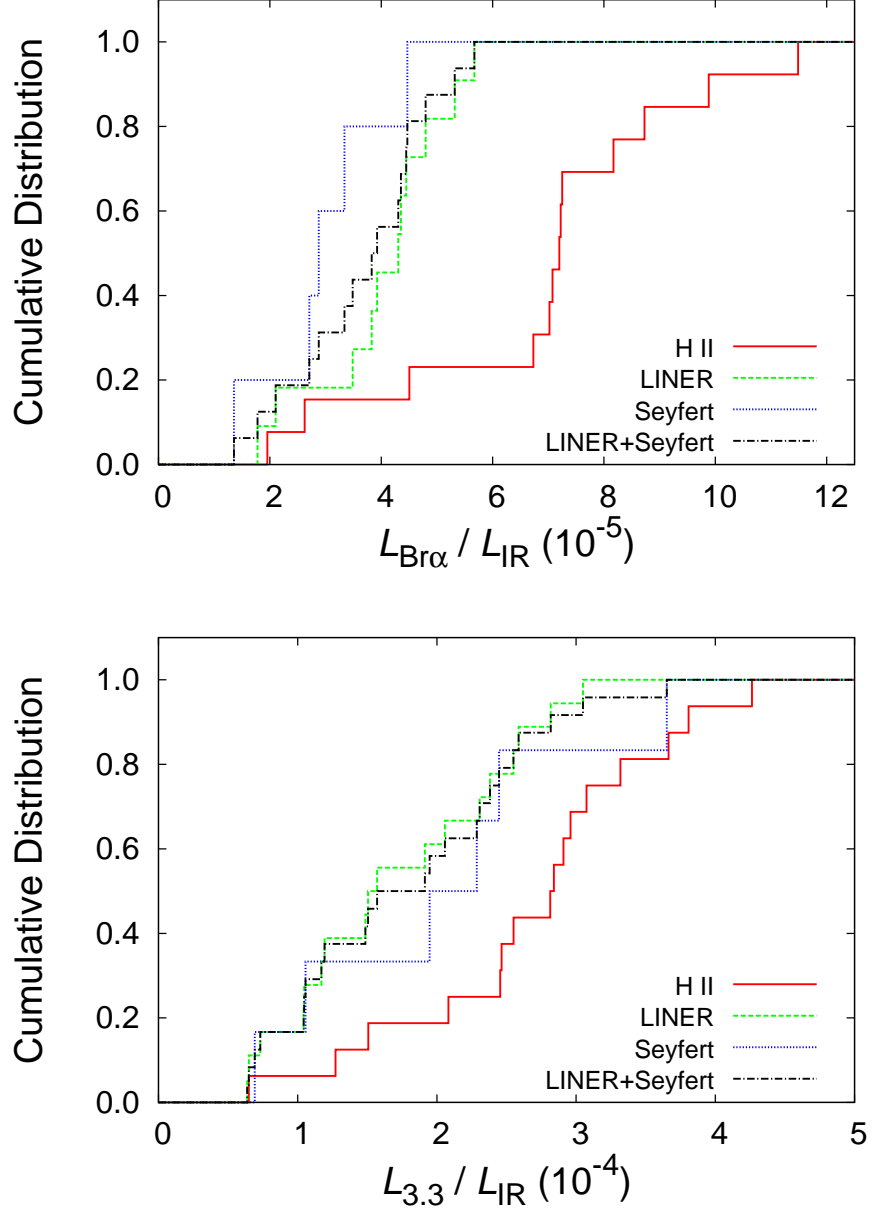


Figure 3.4. Cumulative distribution for the K-S test of the $L_{\text{Br}\alpha}/L_{\text{IR}}$ ratio (top) and the $L_{3.3}/L_{\text{IR}}$ ratio (bottom) for H II galaxies (red solid line), LINERs (green dashed line), Seyferts (blue dotted line), and the combination of LINERs and Seyferts (black dashed-dotted line).

Table 3.7. Mean and Deviation of $L_{\text{Br}\alpha}/L_{\text{IR}}$ and $L_{3.3}/L_{\text{IR}}$

Optical Class	$L_{\text{Br}\alpha}/L_{\text{IR}}$			$L_{3.3}/L_{\text{IR}}$		
	Number of Objects	Mean (10^{-5})	Deviation ^a (10^{-5})	Number of Objects	Mean (10^{-4})	Deviation ^a (10^{-4})
H II	13	6.9	2.6	16	2.7	0.9
LINER	11	4.0	1.2	18	1.7	0.8
Seyfert	5	3.0	1.1	6	2.0	1.1
LINER & Seyfert	16	3.7	1.2	24	1.8	0.8

^a1- σ standard deviation.

in Table 3.6. The K-S test between LINERs and Seyferts again indicates no significant difference between them, while the probability between H II galaxies and the combination of LINERs and Seyferts is 4.0×10^{-3} . This means that the distribution of the $L_{3.3}/L_{\text{IR}}$ is statistically different between H II galaxies and LINERs/Seyferts. Thus the result we obtained with the $L_{\text{Br}\alpha}/L_{\text{IR}}$ ratio is reproduced using $L_{3.3}$ with the larger sample.

The mean $L_{\text{Br}\alpha}/L_{\text{IR}}$ ratio in each classification is calculated and shown in Table 3.7. The combination of LINERs and Seyferts yields a mean $L_{\text{Br}\alpha}/L_{\text{IR}}$ ratio of 3.7×10^{-5} , which is about half of that in H II galaxies (6.9×10^{-5}). To investigate whether the mean $L_{\text{Br}\alpha}/L_{\text{IR}}$ ratio in LINERs or Seyferts is statistically lower than that in H II galaxies, we performed the Student's t test. The t -test probabilities that two sets of samples originate from populations with the same mean $L_{\text{Br}\alpha}/L_{\text{IR}}$ ratio are summarized in Table 3.6. The test between LINERs and Seyferts indicates that there is no significant difference between them, whereas H II galaxies show a low probability against the others. The probability between H II galaxies and the combination of LINERs and Seyferts is 9.0×10^{-4} , which is statistically significant. Thus, we conclude that the mean $L_{\text{Br}\alpha}/L_{\text{IR}}$ ratio in LINERs and Seyferts is significantly lower, about half of that in H II galaxies.

In the same way as for the $L_{\text{Br}\alpha}/L_{\text{IR}}$ ratio, the difference in the mean $L_{3.3}/L_{\text{IR}}$ ratio (Table 3.7) between the galaxies with different optical classifications is examined with the Student's t test. The result is summarized in Table 3.6. From the t -test probabilities for the $L_{3.3}/L_{\text{IR}}$ ratio, we conclude that the mean $L_{3.3}/L_{\text{IR}}$ ratio in LINERs and Seyferts is

significantly lower than that in H II galaxies. This is consistent with the result obtained from the $L_{\text{Br}\alpha}/L_{\text{IR}}$ ratio. Thus, with the larger sample, the difference among the galaxies with different optical classifications is further confirmed.

We here discuss the possible effect of dust extinction on the difference of the $L_{\text{Br}\alpha}/L_{\text{IR}}$ and $L_{3.3}/L_{\text{IR}}$ ratios. To use dust extinction to explain the difference in the mean $L_{\text{Br}\alpha}/L_{\text{IR}}$ or $L_{3.3}/L_{\text{IR}}$ ratio among galaxies with different optical classifications, extinction should be much higher in LINERs and Seyferts than in H II galaxies. However, Veilleux et al. (2009) reported that the optical depth of the $9.7 \mu\text{m}$ silicate absorption was generally smaller in Seyferts than in H II galaxies based on the *Spitzer* results. This indicates that the dust extinction in H II galaxies is generally higher than that in Seyferts and is opposite to the above scenario. Therefore, we conclude that the difference in the mean $L_{\text{Br}\alpha}/L_{\text{IR}}$ and $L_{3.3}/L_{\text{IR}}$ ratios among the galaxies with different optical classifications cannot be explained by the effect of heavy dust extinction.

In summary, we conclude that the mean $L_{\text{Br}\alpha}/L_{\text{IR}}$ and $L_{3.3}/L_{\text{IR}}$ ratios are significantly lower in LINERs and Seyferts than in H II galaxies. This difference is not attributable to the effect of dust extinction.

3.4.1.2 Fractional Contribution of Starburst as Energy Sources

We propose that the $L_{\text{Br}\alpha}/L_{\text{IR}}$ and $L_{3.3}/L_{\text{IR}}$ ratios reflect the fractional contribution of starburst to the total infrared luminosity, and the relative difference of the ratios among the galaxies with different optical classifications shows the difference in their energy sources.

We here assume that H II galaxies are completely energized by starburst, and the $L_{\text{Br}\alpha}/L_{\text{IR}}$ ratio of 6.9×10^{-5} , which is the mean ratio in H II galaxies, corresponds to a starburst contribution of 100%. On the basis of this assumption, we estimate the starburst contribution as $R_{\text{SB}}^{\text{AKARI}} = (L_{\text{Br}\alpha}/L_{\text{IR}})/(L_{\text{Br}\alpha}/L_{\text{IR}})_0$, where $(L_{\text{Br}\alpha}/L_{\text{IR}})_0 = 6.9 \times 10^{-5}$.

Even the *AKARI* observations, however, could be affected by dust extinction. To verify this effect, we compare our result with the mid-infrared spectroscopic results obtained by *Spitzer* IRS spectroscopy, which is expected to be less affected by dust extinction. Veilleux et al. (2009) summarized the six independent diagnostics to estimate the starburst/AGN contribution in ULIRGs based on *Spitzer* observations. Among our targets, 11 galaxies

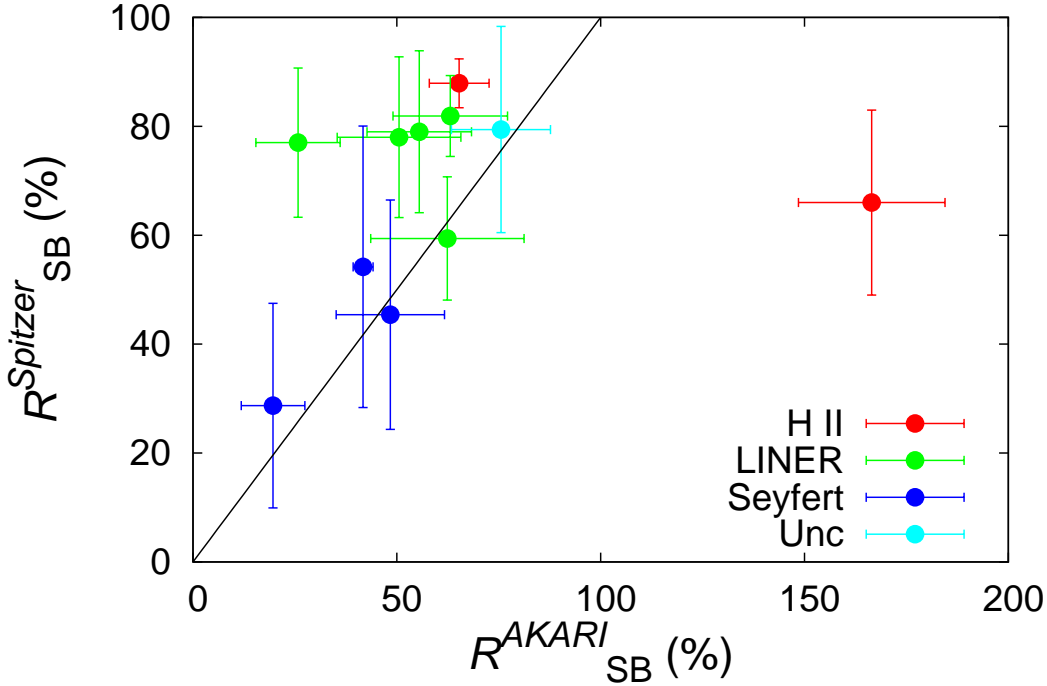


Figure 3.5. Comparison of the starburst contribution to the bolometric luminosity of galaxies measured by the *Spitzer* result ($R_{\text{SB}}^{\text{Spitzer}}$) with that estimated from our *AKARI* result ($R_{\text{SB}}^{\text{AKARI}}$; see §3.4.1.1). $R_{\text{SB}}^{\text{Spitzer}}$ is calculated from Column 8 of Table 12 in Veilleux et al. (2009). The error bar of $R_{\text{SB}}^{\text{Spitzer}}$ represents the standard deviation of the six methods of Table 12 in Veilleux et al. (2009). The symbols and colors represent the optical classifications of galaxies. The black solid line indicates $R_{\text{SB}}^{\text{Spitzer}} = R_{\text{SB}}^{\text{AKARI}}$.

are also reported in Veilleux et al. (2009), and the starburst contribution to the bolometric luminosity ($R_{\text{SB}}^{\text{Spitzer}}$) in these galaxies is calculated. To see the consistency of our work and the previous *Spitzer* works, we compare $R_{\text{SB}}^{\text{AKARI}}$ with $R_{\text{SB}}^{\text{Spitzer}}$ in Figure 3.5.

Figure 3.5 shows general agreement between $R_{\text{SB}}^{\text{AKARI}}$ and $R_{\text{SB}}^{\text{Spitzer}}$, but we note that $R_{\text{SB}}^{\text{Spitzer}}$ might be slightly higher than $R_{\text{SB}}^{\text{AKARI}}$ especially in LINERs. To investigate the difference of $R_{\text{SB}}^{\text{Spitzer}}$ and $R_{\text{SB}}^{\text{AKARI}}$, we estimate the error-weighted mean $R_{\text{SB}}^{\text{Spitzer}}/R_{\text{SB}}^{\text{AKARI}}$ ratio. The ratio of the total sample is 0.84 ± 0.15 , while it is 0.69 ± 0.44 , 1.13 ± 0.15 , and 1.28 ± 0.16 in H II galaxies, Seyferts, and LINERs, respectively. The biggest deviation of the ratio from unity is seen in LINERs, at a level of about 30%, but the significance level is not high (1.8σ). Due to the limited number of samples, we cannot deny the possibility that the two results might be different, but the current sample does not show a clear difference between the starburst contributions estimated by the two methods. We hence

conclude that our result is consistent with the *Spitzer* result, and so $R_{\text{SB}}^{\text{AKARI}}$ can be used as a quantitative indicator of the starburst contribution to the total infrared luminosity. Below, we use the $L_{\text{Br}\alpha}/L_{\text{IR}}$ ratio to discuss the energy sources of the galaxies.

We should note that the mean $R_{\text{SB}}^{\text{Spitzer}}/R_{\text{SB}}^{\text{AKARI}}$ ratio in the entire sample is affected by one outlying H II galaxy, IRAS 17068+4027. If we calculate the mean $R_{\text{SB}}^{\text{Spitzer}}/R_{\text{SB}}^{\text{AKARI}}$ ratio without IRAS 17068+4027, it becomes 1.30 ± 0.08 (compared to 0.84 ± 0.15 with IRAS 17068+4027), and so our *AKARI* observation could underestimate the starburst contribution by about 30% relative to the *Spitzer* observation. We have searched for a possible cause of the high $R_{\text{SB}}^{\text{AKARI}}$ value relative to $R_{\text{SB}}^{\text{Spitzer}}$ in IRAS 17068+4027, but have not successfully identified one. For example, we cannot attribute this to the hidden AGN activity, since Figure 3.5 shows that the $R_{\text{SB}}^{\text{Spitzer}}/R_{\text{SB}}^{\text{AKARI}}$ ratio of Seyferts, which are dominated by AGNs, does not deviate from unity. Moreover, we cannot find any clear evidence of the presence of AGNs in this galaxy from our observation (e.g., absence of the broad line) and other literature (e.g., Veilleux et al. 1997; Kim et al. 1998). We hence include this galaxy in the estimate of $R_{\text{SB}}^{\text{Spitzer}}/R_{\text{SB}}^{\text{AKARI}}$ since we have found no clear reason to ignore it.

3.4.1.3 Energy Sources of ULIRGs

Starburst is thought to be the dominant energy source in H II galaxies, while AGNs are considered to dominate in Seyferts. The result that the mean $L_{\text{Br}\alpha}/L_{\text{IR}}$ ratio is lower in Seyferts than in H II galaxies confirms this difference in energy sources. Here we consider the standard error, which equals the standard deviation divided by the square root of the sample size, as the statistical error of the mean $L_{\text{Br}\alpha}/L_{\text{IR}}$ and $L_{3.3}/L_{\text{IR}}$ ratios. The mean $L_{\text{Br}\alpha}/L_{\text{IR}}$ ratio in Seyferts is $(43 \pm 9)\%$ of that in H II galaxies. This means that the fractional contribution of starburst to the total infrared luminosity in Seyferts is $(43 \pm 9)\%$. Given the result that LINERs also have a lower $((58 \pm 8)\%)$ $L_{\text{Br}\alpha}/L_{\text{IR}}$ ratio than H II galaxies, energy sources other than starburst are needed in LINERs. The $L_{\text{Br}\alpha}/L_{\text{IR}}$ ratio in LINERs is similar to that in Seyferts, and thus we propose that AGNs are needed as energy generation mechanisms in LINERs as well as in Seyferts. The $L_{3.3}/L_{\text{IR}}$ ratio in LINERs is also similar to that in Seyferts and lower than that in H II galaxies. Thus the

idea that AGNs are needed in LINERs, as well as in Seyferts, is also supported in the larger sample.

The combination of LINERs and Seyferts yields a mean $L_{\text{Br}\alpha}/L_{\text{IR}}$ ratio of $(3.7 \pm 0.3) \times 10^{-5}$, which indicates that the fractional contribution of starburst to the total infrared luminosity in these galaxies is $(53 \pm 7)\%$. With the larger sample, using the $L_{3.3}/L_{\text{IR}}$ ratio, the contribution of starburst to the total infrared luminosity in the combination of LINERs and Seyferts is estimated as $(67 \pm 9)\%$. From this result, it is inferred that AGNs produce a significant fraction $((33 \pm 9)\%)$ of the total infrared luminosity in LINERs and Seyferts, causing the separation of the ratios between H II galaxies and LINERs/Seyferts. As a whole, our result indicates that AGNs account for about one-third of the total infrared luminosity of LINERs and Seyferts, and starburst explains the remaining infrared luminosity of ULIRGs. The mean $L_{3.3}/L_{\text{IR}}$ ratio in the entire sample is calculated as $(2.1 \pm 0.2) \times 10^{-4}$, which yields a contribution of starburst to the total infrared luminosity of $(80 \pm 9)\%$. Consequently, the AGN contribution to the total infrared luminosity in the entire sample is indicated as $(20 \pm 9)\%$. Thus, we conclude that starburst is the dominant power source for the extreme infrared luminosity of ULIRGs.

In addition to Veilleux et al. (2009), numerous works have been done using the mid-infrared spectroscopy with the *Spitzer* satellite to reveal the dust-enshrouded energy sources of ULIRGs. Armus et al. (2007) investigated the mid-infrared spectra of 10 ULIRGs and found evidence for AGNs in galaxies with optical Seyfert or LINER classifications, while they did not find evidence for buried AGNs in ULIRGs classified optically as H II galaxies. Nardini et al. (2009) analyzed 5–8 μm spectra of 71 ULIRGs and derived the AGN/starburst contribution to the overall energy output of each source using the technique of spectral decomposition. They found that the main fraction of ULIRG luminosity arose from starburst, while the AGN contribution was non-negligible ($\sim 23\%$). From radio observations of seven ULIRGs, Prouton et al. (2004) concluded that the AGN contribution was at most 50%. Our conclusion that starburst is the dominant power source for ULIRGs is consistent with these results from work at longer wavelengths. In particular, our estimation of the AGN contribution to the total infrared luminosity in our entire sample $((20 \pm 9)\%)$ shows a good agreement with the result obtained by Nardini et al. (2009).

For the less luminous population, luminous infrared galaxies (LIRGs; $L_{\text{IR}} = 10^{11}$ – $10^{12}L_{\odot}$), Alonso-Herrero et al. (2012) decomposed the *Spitzer* spectra of 53 LIRGs into AGN and starburst components. They found that the AGN contribution was only 5% on average in their sample, and the bulk of the infrared luminosity of these LIRGs was due to the starburst activity. Our estimation of the AGN contribution in ULIRGs is larger than this result from observation of LIRGs. As discussed in Alonso-Herrero et al. (2012), this supports the idea that the higher the total infrared luminosity, the greater the AGN contribution to it. Shipley et al. (2013) investigated mid-infrared PAH emissions in 65 LIRGs and estimated the AGN contribution to the total infrared luminosity in their targets. They divided their sample into a subsample of galaxies with *Spitzer* 3.6–8.0 μm colors indicative of warm dust heated by AGNs (IRAGN; 14 galaxies) and those galaxies whose colors indicated starburst processes (non-IRAGN; 65 galaxies). They found that for most IRAGN starburst accounted for 10%–50% of the total IR luminosity, while non-IRAGN were mostly dominated by starburst. Their estimation of the starburst contribution in IRAGN is quite low. It is even lower than our estimation of the starburst contribution in LINERs and Seyferts ($(67 \pm 9)\%$). We attribute the low starburst contribution of IRAGN relative to our estimation to the difference in the methods of classification of galaxies. We propose that the *Spitzer* classification method of IRAGN separated AGN-dominated galaxies better than the optical classification method, which should suffer from the effect of dust extinction, and caused the low starburst contribution in the IRAGN sample.

The results at longer wavelength rely on indicators that are a little complicated, such as fine-structure lines or spectral decomposition techniques that assume empirical starburst and AGN templates. On the other hand, our method is based on a direct indicator of the ionizing photons, the $\text{Br}\alpha$ line, and so is able to estimate the contribution of starburst in a robust way. We conclude that the contribution of starburst to the total infrared luminosity is different in galaxies with different optical classifications. The starburst contribution is estimated as $(67 \pm 9)\%$ in LINERs and Seyferts. Our result is consistent with the previous works at longer wavelengths.

3.4.2 Deficit of Ionizing Photons

Here we revisit the assumption of 100% contribution of starburst in H II galaxies by converting the observed luminosities to the number of ionizing photons. The Br α line luminosity can be converted into the number of ionizing photons, $Q_{\text{Br}\alpha}$, on the assumption of case B with $T = 10000$ K and the low-density limit of the model by Osterbrock & Ferland (2006):

$$Q_{\text{Br}\alpha} \text{ (s}^{-1}\text{)} = 2.54 \times 10^{13} L_{\text{Br}\alpha} \text{ (erg s}^{-1}\text{)}. \quad (3.2)$$

The number of ionizing photons from OB stars is theoretically related to the SFR on the assumption of the initial mass function (e.g., Kennicutt & Evans 2012). On the other hand, the total infrared luminosity can also be converted to SFR on the assumption of the initial mass function if it is generated solely by star formation (Kennicutt & Evans 2012). We assume that this is the case in H II galaxies. Thus, we can estimate the number of ionizing photons (Q_{IR}) expected from the SFR required to explain the total infrared luminosity. Adopting the calibration provided by Murphy et al. (2011), we convert the total infrared luminosity into the number of ionizing photons as

$$Q_{\text{IR}} \text{ (s}^{-1}\text{)} = 5.33 \times 10^9 L_{\text{IR}} \text{ (erg s}^{-1}\text{)}. \quad (3.3)$$

An $L_{\text{Br}\alpha}/L_{\text{IR}}$ ratio of 2.1×10^{-4} is required to obtain $Q_{\text{Br}\alpha}/Q_{\text{IR}} = 100\%$.

Using Equations (3.2) and (3.3), we convert the $L_{\text{Br}\alpha}/L_{\text{IR}}$ ratio into the $Q_{\text{Br}\alpha}/Q_{\text{IR}}$ ratio. We find that the mean $L_{\text{Br}\alpha}/L_{\text{IR}}$ ratio in H II galaxies of 6.9×10^{-5} yields a $Q_{\text{Br}\alpha}/Q_{\text{IR}}$ ratio of only $\sim 33\%$. This indicates that starburst explains merely less than one-third of the total infrared luminosity, even in H II galaxies. This is inconsistent with the assumption that H II galaxies are dominated by starburst. A similar result, that the number of ionizing photons derived from the near-infrared hydrogen recombination lines is low relative to that expected from the total infrared luminosity in ULIRGs, has been reported by Goldader et al. (1995) using the Br γ line and by Valdés et al. (2005) using the Pa α and Br γ lines. Our result indicates that the Br α line also suffers the same kind of deficit.

Comparing our result with the *Spitzer* result (Figure 3.5), we show that $R_{\text{SB}}^{\text{AKARI}}$, which is based on the assumption of 100% contribution of starburst in H II galaxies, is consistent with the fractional contribution of starburst estimated from the longer wavelength result (§3.4.1.2). This indicates that the apparently low $Q_{\text{Br}\alpha}/Q_{\text{IR}}$ ratio is caused by underestimation of the number of ionizing photons with the Br α line by a factor of ~ 3 .

As we see in §3.3.2 with the entire sample, the Br α line flux could be underestimated by a factor of two due to dust extinction. To investigate this effect in detail, we correct $L_{\text{Br}\alpha}$ using $A_V^{9.7}$ and calculate the mean $Q_{\text{Br}\alpha}/Q_{\text{IR}}$ ratio in H II galaxies. We find that the mean $Q_{\text{Br}\alpha}/Q_{\text{IR}}$ ratio increases to 55.5% but is still lower than 100%. The standard error is estimated as 7.5% (1σ), and so the significance of the deviation from 100% is estimated as $\sim 6\sigma$ even after the correction for dust extinction with $A_V^{9.7}$. Thus we conclude that the number of ionizing photons traced by the Br α line is deficient relative to that expected from the total infrared luminosity, even taking heavy dust extinction into consideration.

In addition to heavy dust extinction, we propose that dust within the starburst-ionized regions absorbs a significant fraction of ionizing photons from OB stars and causes the underestimation of the number of ionizing photons with the Br α line. If only a fraction $f\%$ of photons with energy > 13.6 eV ionizes the gas while the remaining $(100 - f)\%$ is absorbed by dust, the hydrogen lines underestimate the number of ionizing photons as $f\%$ of the intrinsic value. Hirashita et al. (2003) have estimated an average value of $(100 - f) \sim 50\%$, with some objects reaching $(100 - f) \sim 80\%$, based on observations of IUE-selected star-forming galaxies. To explain the discrepancy between $Q_{\text{Br}\alpha}$ and Q_{IR} in H II galaxies after taking the uncertainty of dust extinction into consideration, the fraction of ionizing photons absorbed by dust is required to be $\sim 45\%$, which is well within the range of the possible values indicated by Hirashita et al. (2003). We suggest that the absorption of ionizing photons within H II regions is required in addition to heavy dust extinction of the Br α line in order to explain the underestimation of $Q_{\text{Br}\alpha}$ relative to Q_{IR} in ULIRGs.

3.5 Summary

We conducted systematic observations of the hydrogen Br α line with the *AKARI* IRC 2.5–5.0 μm spectroscopy in 50 nearby ($z < 0.3$) ULIRGs to estimate the strength of starburst unbiased by dust extinction. We detected the Br α line in 33 ULIRGs. Comparing the Br α line with the 3.3 μm PAH emission and the total infrared luminosity, we investigate the fractional contribution of starburst to the total infrared luminosity in ULIRGs. The main results are as follows:

1. The effect of heavy dust extinction of the Br α line is investigated with the Br β /Br α line ratio in one source and the optical depth of 9.7 μm silicate absorption taken from *Spitzer* results in the entire sample. We conclude that the intrinsic Br α line flux is determined within the uncertainty of underestimation by a factor of two even if we take the effect of heavy dust extinction into consideration.
2. We compare the Br α line luminosity ($L_{\text{Br}\alpha}$) with the 3.3 μm PAH emission luminosity ($L_{3.3}$) and find a good correlation between them. This indicates that $L_{3.3}$ and $L_{\text{Br}\alpha}$ trace the same excitation sources, i.e., star formation. To investigate star formation in fainter objects, we derive $L_{\text{Br}\alpha}/L_{3.3} = 0.177 \pm 0.003$.
3. On the other hand, the total infrared luminosity (L_{IR}) and $L_{\text{Br}\alpha}$ show no clear correlation with each other. We also confirm that $L_{3.3}$ and L_{IR} show no clear correlation with each other in a larger sample of 46 galaxies in which objects with no Br α line detection are included. The mean $L_{\text{Br}\alpha}/L_{\text{IR}}$ (and $L_{3.3}/L_{\text{IR}}$) ratio is significantly lower in galaxies optically classified as LINERs and Seyferts than in H II galaxies. We propose that the difference reflects the contribution of starburst to the total infrared luminosity in ULIRGs. Assuming that H II galaxies are 100% energized by starburst, we estimate that the contribution of starburst to the total infrared luminosity in LINERs and Seyferts is $(67 \pm 9)\%$, and AGNs contribute to the remaining $(33 \pm 9)\%$.
4. We find that the number of ionizing photons derived from the Br α line ($Q_{\text{Br}\alpha}$) is significantly smaller than that expected from the SFR required to explain the total infrared luminosity (Q_{IR}). The mean $L_{\text{Br}\alpha}/L_{\text{IR}}$ ratio in H II galaxies yields a

$Q_{\text{Br}\alpha}/Q_{\text{IR}}$ ratio of only $(55.5 \pm 7.5)\%$ even after taking heavy dust extinction into consideration. We attribute this apparently low ratio to the underestimation of the number of ionizing photons with the $\text{Br}\alpha$ line. We conclude that the number of ionizing photons traced by the $\text{Br}\alpha$ line is deficient relative to that expected from the total infrared luminosity, even taking the effect of heavy dust extinction into consideration. As an additional cause of the deficit, we propose that dust within H II regions absorbs a significant fraction ($\sim 45\%$) of ionizing photons.

Chapter 4

Anomaly of Hydrogen

Recombination Line Ratio

4.1 Introduction

In this chapter, we investigate the H I $\text{Br}\beta/\text{Br}\alpha$ line ratio in ULIRGs and find an anomalously high $\text{Br}\beta/\text{Br}\alpha$ line ratio. We discuss possible causes of the high $\text{Br}\beta/\text{Br}\alpha$ line ratio and its implications for the nature of starburst in ULIRGs.

We expect that the $\text{Br}\beta/\text{Br}\alpha$ line ratio is less sensitive to dust extinction than the optical $\text{H}\beta/\text{H}\alpha$ line ratio. For instance, the $\text{H}\beta/\text{H}\alpha$ line ratio is nearly halved from that of case B with dust extinction of $A_V \sim 1$ mag, while the $\text{Br}\beta/\text{Br}\alpha$ line ratio is reduced by only $\sim 4\%$ from that of case B with the same extinction (Draine 2003). On the other hand, the dust extinction of $A_V > 15$ mag is expected in ULIRGs (e.g., Genzel et al. 1998). The $\text{Br}\beta/\text{Br}\alpha$ line ratio is halved from that of case B with dust extinction of $A_V \sim 15$ mag. Thus the $\text{Br}\beta/\text{Br}\alpha$ line ratio is expected to be a good indicator of high dust extinction in ULIRGs.

The validity of the assumption of case B is, however, poorly investigated in H II regions with such high dust extinction in ULIRGs. As we conclude in Chapter 3, most of the enormous infrared luminosity is produced by starburst in ULIRGs. This suggests that large amount of gas is contained in starburst regions in ULIRGs. If the large amount of gas makes H I lines other than those of the Lyman series optically thick, the case B

assumption is no longer valid, and line ratios would be significantly changed from that of case B. We investigate this problem with systematically observing the Br α and Br β lines in ULIRGs.

Using the *AKARI* near-infrared spectroscopy, we conduct a systematic observation of the Br α and Br β lines in ULIRGs. In Section 4.2, we present our targets, observations, and method of data reduction. The resulting spectra and measured flux of Br α and Br β lines are presented in Section 4.3. We discover ULIRGs with an anomalously high Br β /Br α line ratio, which we cannot explain with the case B theory and dust extinction. In Section 4.4, we discuss possible causes of the high Br β /Br α line ratio. We summarize our study in this chapter in Section 4.5. Throughout this chapter, we assume that the universe is flat with $\Omega_M = 0.27$, $\Omega_\Lambda = 0.73$, and $H_0 = 70.4 \text{ km s}^{-1} \text{ Mpc}^{-1}$ (Komatsu et al. 2011). We also assume the Milky way dust model of Draine (2003) for the extinction curve. In this model, dust extinction at the wavelength of the H α , H β , Br α , and Br β lines are estimated to be $A_{H\alpha} = 0.776A_V$, $A_{H\beta} = 1.17A_V$, $A_{Br\alpha} = 3.56 \times 10^{-2}A_V$, and $A_{Br\beta} = 8.09 \times 10^{-2}A_V$, respectively.

4.2 Observations and Data Reduction

4.2.1 Targets

Among the pointed observations of *AKARI*, we focused on those taken with a mission program “Evolution of ultraluminous infrared galaxies and active galactic nuclei” (AGNUL; P.I. T. Nakagawa) during the liquid-He cool holding period. This is the same set of data as that used in Chapter 3. The AGNUL program conducted systematic near-infrared spectroscopic observations of ULIRGs in the local universe. During the phases 1 & 2 observational period, 50 near-infrared grism spectroscopic observations of ULIRGs were conducted in this program. The observation log and basic information of the 50 AGNUL targets are summarized in Tables 3.1 and 3.2, respectively.

In addition, we checked all IRC near-infrared spectra taken within the phases 1 & 2 period using “IRC Point Source Spectral Catalogue” by visual inspection. Possible targets which can be used for this study were searched, and we found two galaxies (IRAS

Table 4.1. Observation Log for Additional Targets

Object Name	Observation ID	Observation Date
IRAS 09022–3615	3051018.1	2007 May 26
IRAS 10565+2448	3051019.1	2007 May 28

Table 4.2. Basic Information of Additional Target ULIRGs

Object Name	z^a	D_L^b (Mpc)	F_{25}^c (Jy)	F_{60}^c (Jy)	F_{100}^c (Jy)	L_{IR}^d ($10^{12}L_\odot$)	Optical ^e class	Ref. ^f
IRAS 09022–3615	0.060	266	1.20	11.6	11.1	1.64	H II	1
IRAS 10565+2448	0.043	190	1.27	12.1	15.0	1.07	H II	2

^aRedshift.

^bLuminosity distance calculated from z using our adopted cosmology.

^cIRAS fluxes at 25 μm (F_{25}), 60 μm (F_{60}), and 100 μm (F_{100}).

^dTotal infrared (3–1100 μm) luminosity calculated with $L_{IR} = 4\pi D_L^2 (\xi_1 \nu F_{25} + \xi_2 \nu F_{60} + \xi_3 \nu F_{100})$, $(\xi_1, \xi_2, \xi_3) = (2.403, -0.2454, 1.6381)$ (Dale & Helou 2002).

^eOptical classification of galaxies.

^fReferences of redshift: (1) Strauss et al. (1992); (2) Downes et al. (1993).

09022–3615 and IRAS 10565+2448) in which the Br α and Br β lines were clearly detected. They were observed with a mission program “the nature of new ULIRGs at intermediate redshift” (NULIZ; P.I. H. HoSeong). To enlarge the sample size, we added the two targets to our sample. The observation log and basic information of the two objects are summarized in Tables 4.1 and 4.2. In summary, we analyzed 52 near-infrared spectroscopic data taken with the observations described above.

4.2.2 Reduction of Spectroscopic Data

The data were basically reduced with the same process as that in Chapter 3, but we here used “IRC Spectroscopy Toolkit Version 20150331,” which was a different version from that used in Chapter 3. The spectral response curve was revised in this version. In addition, we revised error estimation and propagation in the toolkit. In chapter 3, we have to

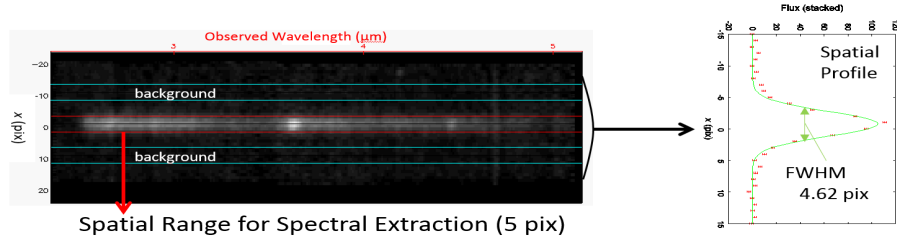


Figure 4.1. Left panel shows an example of two-dimensional spectra. The spatial region used for spectral extraction is shown by red lines while that used for background estimation is indicated by blue lines. The right panel shows the result of the stacking of the spectrum along the spatial direction. The spatial width of this object is estimated to be FWHM=4.62 pix.

consider both the statistical and systematic errors in order to compare our result with other observations. In contrast, we discuss the $\text{Br}\beta/\text{Br}\alpha$ line ratio in this chapter. The $\text{Br}\alpha$ and $\text{Br}\beta$ lines are observed at once within a same *AKARI* near-infrared spectrum, and so we take only the statistical errors into consideration when we calculate the $\text{Br}\beta/\text{Br}\alpha$ line ratio on the assumption that the systematic error affects the absolute flux of the whole spectrum and is canceled out when we take the line ratio. Thus we revised the toolkit so that we were able to obtain the statistical and systematic errors separately. The statistical error was determined by the standard deviation of signals of the blank sky, while the systematic one was derived from the uncertainty of the response calibration. We reduced all the spectroscopic data of the 50 AGNUL sample again. Each frame was dark-subtracted, linearity-corrected, and flat-field corrected. Wavelength and flux calibrations were also made within this toolkit. The wavelength calibration accuracy is taken to be ~ 1 pixel or $\sim 10^{-2} \mu\text{m}$ (Ohyama et al. 2007).

We estimated a spatial extension of the object by stacking the spectrum along the spatial direction (i.e., perpendicular to the dispersion direction) for each source as shown in Figure 4.1. The measured FWHM of the spatial profile is typically ~ 4 –5 pixel, which is consistent with the size of the point spread function of *AKARI* IRC in spectroscopic mode (Lorente et al. 2008). We adopted an aperture width of 5 pixel ($= 7''.3$) along the spatial direction for the spectrum extraction for each ULIRG. Smoothing with a boxcar kernel of 3 pixels in the dispersion direction was applied to each spectrum.

We analyzed 52 spectroscopic data as described in §4.2.1. Since the eastern (E) and

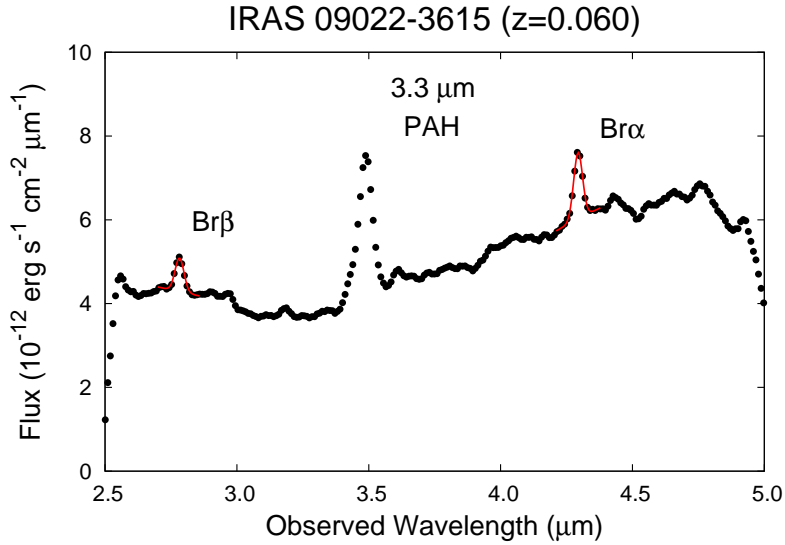


Figure 4.2. Example of the *AKARI* IRC 2.5–5.0 μm spectra of ULIRGs. The best-fit Gaussian profiles for the $\text{Br}\alpha$ and $\text{Br}\beta$ lines are plotted with the red lines.

western (W) nuclei of IRAS 17028+5817 are resolved with *AKARI* IRC, the spectra of the two nuclei are separately extracted. Thus, a total of 53 spectra are obtained from the 52 observations. Figure 4.2 presents an example of the obtained 2.5–5.0 μm spectra of ULIRGs.

4.3 Results

In this section, we present the $\text{Br}\alpha$ and $\text{Br}\beta$ line fluxes obtained with our observation. The $\text{Br}\alpha$ and $\text{Br}\beta$ lines are detected in 31 galaxies. In three out of the 31 galaxies, we find an anomalous $\text{Br}\beta/\text{Br}\alpha$ line ratio which is significantly higher than the case B value of 0.565. The ratio is not explainable with a combination of the case B theory and dust extinction. This indicates that the condition of H II regions in ULIRGs with the anomaly is entirely different from that of Galactic H II regions where the case B theory well explains H I line ratios.

4.3.1 Line Flux

We obtain the 2.5–5.0 μm near-infrared spectra in 53 objects as discussed in the previous chapter. In each spectrum, the $\text{Br}\alpha$ line at a rest-frame wavelength of $\lambda_{\text{rest}} = 4.05 \mu\text{m}$

and the Br β line at $\lambda_{\text{rest}} = 2.63 \mu\text{m}$ are fitted separately with a linear continuum and a Gaussian profile.

First, we fit the Br α line with four free parameters, the offset and the slope of the linear continuum, the normalization of the Gaussian profile, and the central wavelength. The line width is fixed at the spatial width of each object (FWHM $\sim 4\text{--}5$ pixel). Here, we assumed that the spectral resolution is determined by the size of each object because the observations employ slitless spectroscopy, and the intrinsic line widths are narrower than the Δv resolution of $\sim 3000 \text{ km s}^{-1}$. The range of wavelengths used for the fitting is determined to reproduce the continuum emission and is typically $\pm 0.15 \mu\text{m}$ around the central wavelength. The obtained central wavelengths of the Br α lines exhibit small discrepancies from those expected from redshifts. The discrepancy is larger than the fitting error of typically $\sim 10^{-3} \mu\text{m}$ but within the wavelength calibration error of $\sim 10^{-2} \mu\text{m}$ (Ohyama et al. 2007). Therefore, we shift the wavelength of the entire spectrum so that the best-fit central wavelength of the Br α line matches the redshift. Next, after fitting the Br α line, we fit the Br β line with fixing the central wavelength as expected from the redshift and the line width as same as the Br α line, i.e., free parameters are the offset and the slope of the local continuum and the normalization of the Gaussian. The flux of the Br α and Br β lines is then estimated by integrating the best-fit Gaussian profile. We show a typical result of the Gaussian fitting in Figure 4.2.

Among the 53 objects, we estimate the flux of the Br α and Br β lines in 47 galaxies, since four sources (IRAS 00183–7111, IRAS 04313–1649, IRAS 10091+4704, and IRAS 23498+2423) have a redshift higher than 0.2, and the Br α line was not observed within the 2.5–5.0 μm wavelength range, while two sources (IRAS 21477+0502 and IRAS 23129+2548) are found to suffer from spectral overlapping with other objects. In UGC 5101 and Mrk 273, we find the continuum slope changing around the Br β line. Thus we adopt a second-order polynomial as the shape of the continuum for the fitting of the Br β line in UGC 5101 and Mrk 273. We also find that in IRAS 10565+2448 and Mrk 273, the line width of the Br β line is slightly broader than that of the Br α line. The spatial extent of the two-dimensional spectrum at shorter wavelengths ($\lesssim 3 \mu\text{m}$) is $\sim 5\%$ broader than that at longer wavelengths in the two objects. We thus adopt the spatial extent near the wavelength of the Br β line

as the line width for the fitting of the Br β line in IRAS 10565+2448 and Mrk 273.

We detect the Br α or Br β lines at the 3σ level in 31 objects. For undetected lines, we derive 3σ upper-limit fluxes. The measured Br α and Br β line fluxes ($F_{\text{Br}\alpha}$ and $F_{\text{Br}\beta}$) are summarized in Table 4.3 along with the 1σ statistical error. The 1σ systematic error is estimated to be $\sim 10\%$ of the flux. We show all the 47 spectra in Appendix A.

We note that the flux of the Br α line and its error shown in Table 4.3 are different from those estimated in Chapter 3 (tabulated in Table 3.3). This is caused by the difference of the version of the toolkit used for the data reduction and the revision of the error estimation as we mention in §4.2.2. The error shown in Table 3.3 contains both the statistical and systematic errors, while that in Table 4.3 represents only the statistical error. We confirm that the $F_{\text{Br}\alpha}$ values in Tables 3.3 and 4.3 are consistent with each other if we propagate the systematic error ($\sim 10\%$ of the flux) to the statistical error shown in Table 4.3. In the calculation of the Br β /Br α line ratio, we take only the statistical error into consideration on the assumption that the systematic error is canceled out. Thus we are able to estimate the Br β /Br α line ratio with smaller errors than with the error-estimation method in Chapter 3 especially in bright galaxies with a high S/N ratio, i.e., the statistical error is smaller than the systematic error of $\sim 10\%$ of its flux. For faint sources where the statistical error dominates the systematic error, the revision of the error estimation has little effect on the estimation of the Br β /Br α line ratio.

The width of the Br α and Br β lines is consistent with the spectral resolution limit ($\Delta v \sim 3000 \text{ km s}^{-1}$) in all targets within a fitting uncertainty of $\leq 100 \text{ km s}^{-1}$. This means that none of the objects shows a broad component of the Brackett lines with an FWHM broader than $\sim 1000 \text{ km s}^{-1}$. If the broad line region of AGN contributes to line fluxes, hydrogen lines would have an FWHM of a few thousands km s^{-1} (Osterbrock & Ferland 2006). Thus the Br α and Br β lines are expected not to originate from the broad line regions. In Chapter 3, we find a good correlation of the flux of the Br α line and the $3.3 \mu\text{m}$ PAH emission. Combining these results, we assume that the Brackett lines originate from starburst activities in all the sample.

Table 4.3. Flux of Brackett Lines

Object Name	$F_{\text{Br}\alpha}^{\text{a}}$ (10^{-15} erg s $^{-1}$ cm $^{-2}$)	$F_{\text{Br}\beta}$	$F_{\text{Br}\beta}/F_{\text{Br}\alpha}$	A_V (mag)
IRAS 00456–2904	8.16±0.65	3.55±0.84	0.43±0.11	6.3±6.0
IRAS 00482–2721	2.95±0.82	<4.15	<1.40	> –22
IRAS 01199–2307	2.67±0.73	<4.39	<1.65	> –26
IRAS 01298–0744	<2.99	<3.31
IRAS 01355–1814	<2.92	<3.18
IRAS 01494–1845	4.95±0.76	6.46±0.82	1.31±0.26	–20.1±4.8
IRAS 01569–2939	6.28±0.76	<3.56	<0.57	> –0.10
IRAS 02480–3745	2.30±0.73	<3.11	<1.35	> –21
IRAS 03209–0806	5.34±0.81	3.13±0.83	0.59±0.18	–0.8±7.3
IRAS 03521+0028	<5.65	<5.15
IRAS 04074–2801	<2.61	4.99±0.88	>1.91	< –29.2
IRAS 05020–2941	2.78±0.67	<2.56	<0.92	> –12
IRAS 05189–2524	<29.15	<63.90
IRAS 06035–7102	15.1±1.0	7.8±1.7	0.52±0.12	2.1±5.3
IRAS 08572+3915	<36.34	<10.35
IRAS 08591+5248	2.60±0.74	4.20±0.83	1.61±0.56	–25.1±8.3
IRAS 09022–3615	66.95±0.47	33.94±0.78	0.507±0.012	2.60±0.58
UGC 5101	16.0±1.2	17.6±2.2	1.10±0.16	–16.0±3.4
IRAS 09463+8141	<4.08	<4.71
IRAS 09539+0857	<3.38	<2.60
IRAS 10035+2740	<4.21	<4.12
IRAS 10494+4424 ^b	13.54±0.59	11.83±0.87	0.873±0.074	–10.4±2.0
IRAS 10565+2448 ^b	37.6±1.2	36.9±1.6	0.983±0.053	–13.3±1.3
IRAS 10594+3818	6.4±1.1	4.2±1.2	0.65±0.22	–3.4±8.0
IRAS 11028+3130	<3.94	<5.13
IRAS 11180+1623	<5.06	<3.66
IRAS 11387+4116	4.91±0.68	<3.86	<0.79	> –7.9
IRAS 12447+3721	6.17±0.88	2.75±0.85	0.45±0.15	5.7±8.2
Mrk 231	<103	<201
Mrk 273 ^b	47.3±1.3	48.6±1.1	1.029±0.037	–14.37±0.87
IRAS 13469+5833	<3.39	<2.24
IRAS 13539+2920	11.9±1.0	4.44±0.88	0.374±0.073	9.9±4.7
IRAS 14121–0126	3.60±0.81	2.72±0.88	0.59±0.24	–1.1±9.8
IRAS 14202+2615	7.44±0.68	6.82±0.78	0.92±0.13	–11.6±3.5
IRAS 14394+5332	10.97±0.69	7.76±0.95	0.71±0.10	–5.4±3.3
IRAS 15043+5754	<3.44	<4.82
IRAS 16333+4630	3.52±0.84	<4.97	<1.41	> –22
IRAS 16468+5200	<4.39	<4.66

Table 4.3. (continued)

Object Name	$F_{\text{Br}\alpha}^{\text{a}}$ (10^{-15} erg s $^{-1}$ cm $^{-2}$)	$F_{\text{Br}\beta}$	$F_{\text{Br}\beta}/F_{\text{Br}\alpha}$	A_V (mag)
IRAS 16487+5447	10.68±0.72	4.86±0.95	0.455±0.094	5.2±4.9
IRAS 17028+5817E	<4.31	<4.14
IRAS 17028+5817W	6.46±0.91	6.8±1.2	1.05±0.24	-14.9±5.4
IRAS 17044+6720	3.84±0.99	<6.79	<1.77	> -27
IRAS 17068+4027	8.20±0.83	3.41±0.78	0.42±0.10	7.3±5.9
IRAS 17179+5444	2.69±0.81	<3.39	<1.26	> -19
IRAS 19254-7245	24.02±0.70	15.6±1.2	0.648±0.055	-3.3±2.0
IRAS 22088-1831	<3.02	<3.18
IRAS 23128-5919	64.28±0.80	30.17±0.14	0.469±0.006	4.44±0.31

^aObserved flux of the Br α line. The values are different from those in Table 3.3 because of the difference of the version of the toolkit used for the data reduction and the revision of the error estimation in this chapter.

^bShowing anomaly of Br β /Br α line ratio.

4.3.2 Anomaly of Br β /Br α Line Ratio

Owing to the unique 2.5–5.0 μm wavelength coverage of *AKARI*, the Br α and Br β lines are simultaneously observed within a single spectrum. This allows us to accurately estimate the Br β /Br α line ratio without introducing observational uncertainties such as aperture corrections. On the basis of the the Br β /Br α line ratio, visual extinction (A_V) is expected to be assessed in the same way as the Balmer decrement method. We assume an intrinsic line flux ratio for Br β /Br α of 0.565 (Osterbrock & Ferland 2006, case B with $T = 10000$ K and low-density limit). If dust extinction affects the line fluxes, the Br β /Br α line ratio becomes lower because the Br β line has a shorter wavelength and is attenuated more than the Br α line. Thus, the Br β /Br α line ratio lower than 0.565 is expected to be observed.

The comparison of $F_{\text{Br}\alpha}$ and $F_{\text{Br}\beta}$ is shown in Figure 4.3. The estimated Br β /Br α line ratios are summarized in Table 4.3, where we also tabulate A_V inferred from the Br β /Br α line ratio. Galaxies located below the case B line in Figure 4.3 have a Br β /Br α line ratio lower than 0.565. The flux ratio in these galaxies is consistent with the case B theory and dust extinction, and A_V magnitude is estimated to be positive in these objects. However, in five galaxies, we obtain an anomalous Br β /Br α line ratio, which is higher than 0.565

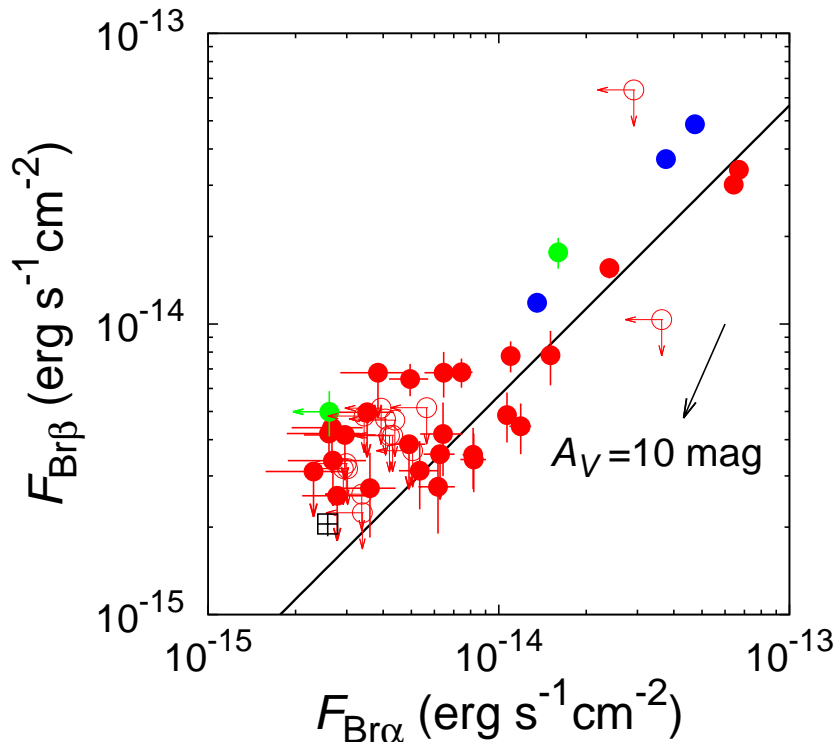


Figure 4.3. The Br α line flux ($F_{\text{Br}\alpha}$) versus the Br β line flux ($F_{\text{Br}\beta}$). The solid line shows the theoretical line ratio in the case B condition: $F_{\text{Br}\beta}/F_{\text{Br}\alpha} = 0.565$. The extinction vector in case of $A_V = 10$ mag is shown as the black arrow. The blue filled circles show galaxies with the anomalous Br β /Br α line ratio (higher than 0.565 with 3σ level) while red filled ones represent those with the normal ratio. The green filled circles show galaxies with the high Br β /Br α line ratio, but are excluded from the discussion because of the large uncertainty in the determination of the underlying continuum of the lines. The red open circles represent galaxies where both the Br α and Br β lines are not detected. The black open square shows the result of the stacked spectrum of 33 galaxies with $F_{\text{Br}\alpha} < 10^{-14}$ erg s $^{-1}$ cm $^{-2}$.

beyond the 3σ uncertainty. These galaxies are located above the case B line in Figure 4.3, i.e., the Br β line is more enhanced relative to the Br α line. This is opposite to the effect of dust extinction.

We examine the spectra of the five galaxies which deviate significantly ($> 3\sigma$) from case B in Figure 4.3. They are IRAS 04074–3801, UGC 5101, IRAS 10494+4424, IRAS 10565+2448, and Mrk 273. Among them, IRAS 04074–3801 is relatively faint, and the continuum is largely affected by a fringe-like pattern. In UGC 5101, the slope of the continuum emission varies significantly around the Br β line and makes it difficult to estimate the line flux. We find that if we adopt a wavelength range for fitting of the Br β line 1.5 times

wider than that of the current fitting, the Br β line flux is reduced by more than $\sim 30\%$ in the two galaxies. Thus we exclude two galaxies, UGC 5101 and IRAS 04074–3801, from discussion of the high Br β /Br α line ratio because of the large uncertainty in the determination of the underlying continuum of the line. On the other hand, in the remaining three galaxies, whose spectra are shown in Figure 4.4, the change of the wavelength range does not affect the line flux more than 10%. We conclude that the three galaxies (shown as blue circles in Figure 4.3), IRAS 10494+4424, IRAS 10565+2448, and Mrk 273, show a Br β /Br α line ratio (0.873 ± 0.074 , 0.983 ± 0.053 , and 1.029 ± 0.037 , respectively) significantly higher than that of case B (0.565). These line-ratio anomalies are not explainable with the case B theory and dust extinction, which could reduce but not increase the Br β /Br α line ratio. We present spectra around the Br α and Br β lines of the three galaxies in Figure 4.5. As a reference, we show the spectra of IRAS 04074–3801 and UGC 5101 in Figure 4.6.

We note that for the fitting of the Br β line, we adopt the second-order polynomial as the shape of the continuum in Mrk 273 and the spatial extent near the wavelength of the Br β line as the line width in IRAS 10565+2448 and Mrk 273. The Br β /Br α line ratio before these changes of the fitting method is 0.897 ± 0.038 and 0.983 ± 0.33 in IRAS 10565+2448 and Mrk 273, respectively. Thus the result that the Br β /Br α line ratio is higher than the case B ratio beyond the 3σ level in these galaxies is not altered by the changes of the fitting model.

We find no distinct physical properties which distinguish the three galaxies with the high Br β /Br α line ratio, IRAS 10494+4424, IRAS 10565+2448, and Mrk 273, from the other sources. The optical classifications of IRAS 10494+4424, IRAS 10565+2448, and Mrk 273 are LINER, H II galaxy, and Seyfert 2, respectively, and are all different from each other (Veilleux et al. 1999a). The three galaxies were observed in infrared wavelengths in several literature (e.g., Imanishi et al. 2008; Veilleux et al. 2009; Lee et al. 2012) in which their infrared properties such as the strength of PAH emissions were compared to those of other ULIRGs, but no significant difference between them was reported.

One common observational property of the three objects is that they have relatively low redshift ($z \sim 0.09$ for IRAS 10494+4424 and $z \sim 0.04$ for IRAS 10565+2448 and Mrk 273) among our sample, and so the Br α and Br β lines are detected with a high S/N ratio.

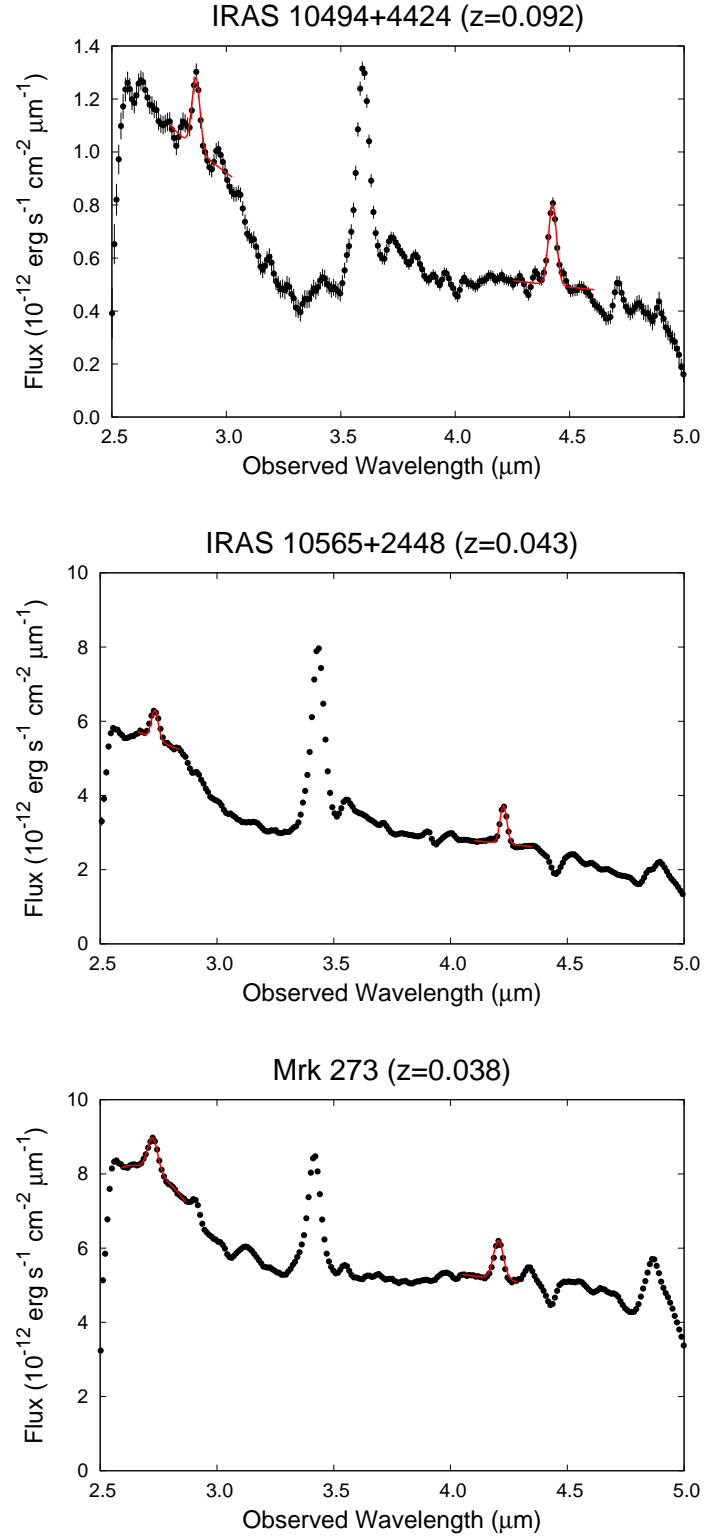


Figure 4.4. 2.5–5.0 μm near-infrared spectra of galaxies which show $\text{Br}\beta/\text{Br}\alpha$ line ratio significantly higher than that of case B. The best-fit Gaussian profiles for the $\text{Br}\alpha$ and $\text{Br}\beta$ lines are plotted with the red lines.

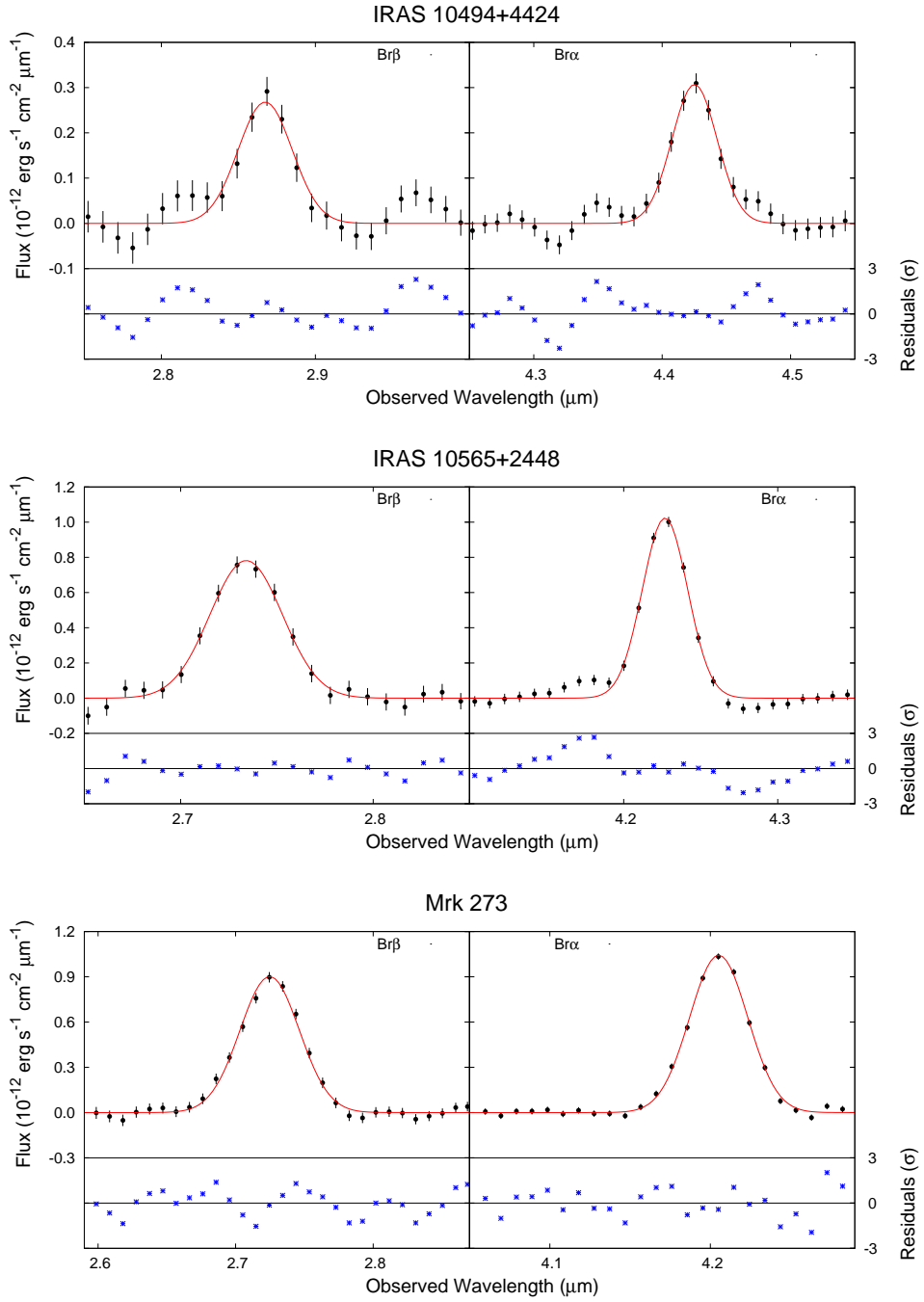


Figure 4.5. Spectra around the Br α (right) and Br β (left) lines of three galaxies which show anomalous Br β /Br α line ratio. Underlying continuum is subtracted. The best-fit Gaussian profile is plotted with the red solid line. The residual spectrum of the best fit is also displayed in the bottom panel with the blue crosses.

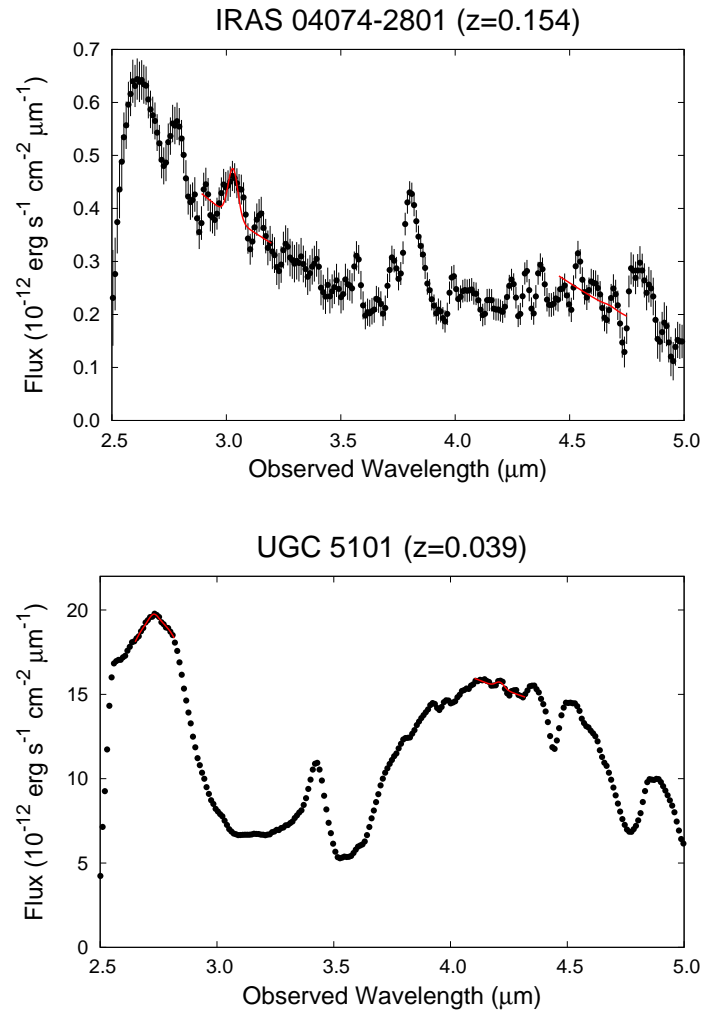


Figure 4.6. 2.5–5.0 μm near-infrared spectra of galaxies which show high $\text{Br}\beta/\text{Br}\alpha$ line ratio but have large uncertainty of the continuum determination. The best-fit Gaussian profiles for the $\text{Br}\alpha$ and $\text{Br}\beta$ lines are plotted with the red lines.

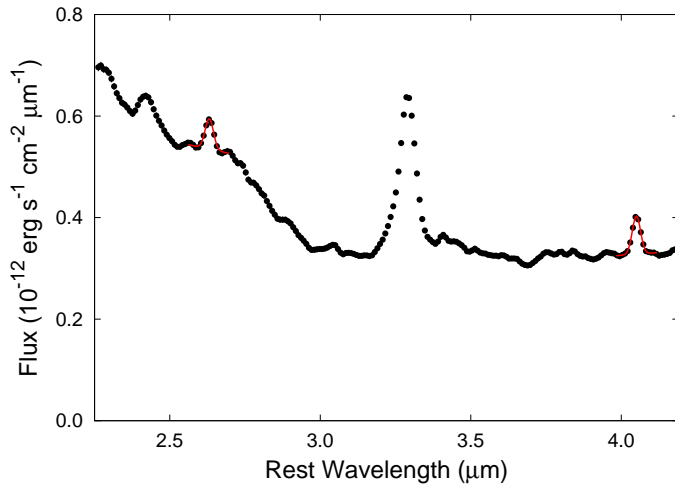


Figure 4.7. Averaged near-infrared spectra of 33 galaxies with $F_{\text{Br}\alpha} < 10^{-14} \text{ erg s}^{-1} \text{ cm}^{-2}$. The best-fit Gaussian profiles for the $\text{Br}\alpha$ and $\text{Br}\beta$ lines are plotted with the red lines.

The $\text{Br}\beta/\text{Br}\alpha$ line ratio is determined well in the three galaxies, and so this is one of the causes of the clear detection of the deviation of the $\text{Br}\beta/\text{Br}\alpha$ line ratio from that of case B. This implies that the anomaly of the $\text{Br}\beta/\text{Br}\alpha$ line ratio could be found in faint galaxies for which we are not able to determine the presence of the anomaly because of the large uncertainty of the observed $\text{Br}\beta/\text{Br}\alpha$ line ratio.

In order to investigate whether the anomaly is found in faint galaxies, we stack the near-infrared spectra of 33 galaxies with $F_{\text{Br}\alpha} < 10^{-14} \text{ erg s}^{-1} \text{ cm}^{-2}$. Each spectrum is corrected for redshift and is stacked in rest wavelengths. The averaged spectrum of the 33 galaxies is shown in Figure 4.7. We measure $F_{\text{Br}\alpha}$ and $F_{\text{Br}\beta}$ of the averaged spectrum with the Gaussian fitting and obtain $F_{\text{Br}\alpha} = (2.58 \pm 0.21) \times 10^{-15} \text{ erg s}^{-1} \text{ cm}^{-2}$ and $F_{\text{Br}\beta} = (2.05 \pm 0.19) \times 10^{-15} \text{ erg s}^{-1} \text{ cm}^{-2}$. This yields the $\text{Br}\beta/\text{Br}\alpha$ line ratio of 0.80 ± 0.10 , which is higher than the case B value of 0.565 with 2.3σ significance. Although the significance is not high enough ($< 3\sigma$), this is opposite to the expectation that ULIRGs show high dust extinction, i.e., the $\text{Br}\beta/\text{Br}\alpha$ line ratio lower than 0.565. Thus we propose that, with future high-sensitivity observations, the anomaly of the $\text{Br}\beta/\text{Br}\alpha$ line ratio would be found in faint galaxies where we are not able to determine the presence of the anomaly with the current *AKARI* observation.

In summary, we find the anomaly of the $\text{Br}\beta/\text{Br}\alpha$ line ratio, which is significantly higher than the case B value and is not explained by the effect of dust extinction, in three

out of 31 ULIRGs where we detect the Br α and Br β lines. As we discuss in Appendix B, the case B line ratio well explains the Br β /Br α line ratio in Galactic H II regions. This indicates that the condition of H II regions in the ULIRGs with the anomaly would be entirely different from that in the Galactic H II regions.

4.3.3 Possible Contamination to Brackett Lines

One possible cause of the line ratio anomaly is that the Brackett lines are blended with other features. The spectral resolution of our observation is not so high ($\sim 0.04\text{--}0.05\ \mu\text{m}$), so that the apparently high Br β /Br α line ratio can be caused by the contamination of other features. We investigate such features whose wavelength is close to that of the Brackett lines. However, observations around the wavelength of the Brackett lines (especially around the Br β line) is few because the wavelength is difficult to access from the ground due to the atmospheric interference, and so little information is available about possible contaminant features.

We investigate a list of infrared atomic lines provided by *ISO* observations (Table 4.10 of Glass 1999) and find no candidate lines near the wavelength of the Br β and Br α lines. With including molecular lines (Table 4.10 of Cox 2000), we find one candidate line, H₂ (1,0) O(2), whose wavelength is $2.627\ \mu\text{m}$. The wavelength of this line is very close to that of the Br β line, so that the flux of the Br β line would be overestimated due to the contamination of the molecular hydrogen line. Here we discuss the possible effect of the molecular hydrogen line on the Br β /Br α line ratio in the three galaxies with the anomalous line ratio, IRAS 10494+4424, IRAS 10565+2448, and Mrk 273.

We estimate the flux of the H₂ (1,0) O(2) line ($F_{\text{O}(2)}$) using another molecular hydrogen rotational-vibrational line, H₂ (1,0) O(3), which has the rest wavelength of $2.802\ \mu\text{m}$ and is simultaneously observed with our observation. Black & van Dishoeck (1987) calculated the flux ratios of the molecular hydrogen rotational-vibrational lines with two excitation mechanisms, fluorescence excitation and shock excitation. In previous ground-based *K*-band observations, H₂ lines were shown to be thermally excited with a temperature of $\sim 2000\ \text{K}$ in IRAS 10494+4424 (Murphy et al. 2001), IRAS 10565+2448 and Mrk 273 (Goldader et al. 1997). Thus we adopt the flux ratio of $F_{\text{O}(2)} = 0.26F_{\text{O}(3)}$ in the shock

Table 4.4. Flux of Molecular Hydrogen Line

Object Name	$F_{O(3)}$ (10^{-14} erg s $^{-1}$ cm $^{-2}$)	$F_{Br\beta}^{cor}/F_{Br\alpha}$ ^a
IRAS 10494+4424	0.272 ± 0.080	0.822 ± 0.074
IRAS 10565+2448	0.49 ± 0.12	0.949 ± 0.048
Mrk 273	2.07 ± 0.12	0.915 ± 0.030

^aThe flux of the H₂ (1,0) O(2) line is subtracted from that of the Br β line on the assumption of $F_{O(2)} = 0.26F_{O(3)}$ (2000 K shock model of Black & van Dishoeck 1987).

model ($T = 2000$ K) of Black & van Dishoeck (1987), where $F_{O(3)}$ is the flux of the H₂ (1,0) O(3) line.

We measure $F_{O(3)}$ in the three galaxies which show the anomalous ratio with the Gaussian fitting. The width and the central wavelength of the Gaussian profile are fixed while the normalization of the Gaussian profile and the linear continuum are set to be free parameters. Figure 4.8 shows the result of the Gaussian fitting of the H₂ (1,0) O(3) line. We detected the H₂ (1,0) O(3) line with the 3σ significance in the three galaxies. The measured flux is summarized in Table 4.4 along with the 1σ statistical error. The 1σ systematic error is estimated to be $\sim 10\%$ of the flux.

Using the H₂ (1,0) O(3) line flux, we estimate the H₂ (1,0) O(2) line flux and extract it from the Br β line flux. Again assuming that the systematic error is canceled out, we estimate the flux ratio of the pure Br β line to the Br α line. We summarize the result in Table 4.4 ($F_{Br\beta}^{cor}/F_{Br\alpha}$). The ratio is still higher than the case B value of 0.565 beyond the 3σ significance level in all the three galaxies. Thus the line contamination to the Br β line does not give full explanation of the anomalous line ratio. We conclude that the anomalous Br β /Br α ratio is real, and intrinsic condition of the ionized gas itself makes the ratio anomalous.

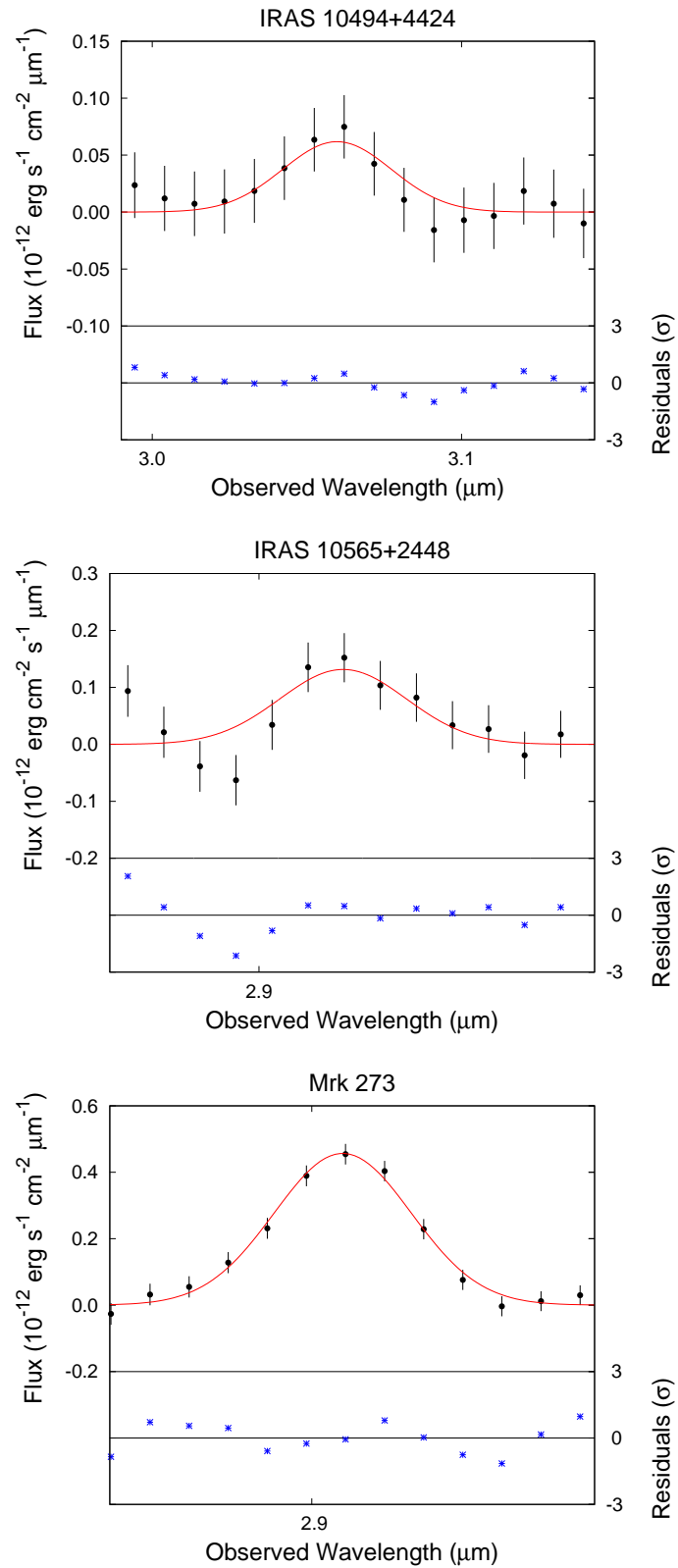


Figure 4.8. Spectra around the H_2 (1,0) O(3) line. Underlying continuum is subtracted. The best-fit Gaussian profile is plotted with the red solid line. The residual spectrum of the best fit is also displayed in the bottom panel with the blue crosses.

4.4 Discussion

In this section, we discuss possible causes of the anomalous $\text{Br}\beta/\text{Br}\alpha$ line ratio we discover in the previous section. In §4.4.1, we explore possible causes of the high $\text{Br}\beta/\text{Br}\alpha$ line ratio considering the hydrogen level population and the optical depth effect of the lines. On the basis of a numerical simulation, we propose conditions with a large column density achieved by high density gas as a possible cause of the high $\text{Br}\beta/\text{Br}\alpha$ line ratio. We discuss the possibility to observe such high-density H II regions in ULIRGs in §4.4.2. In §4.4.3, we compare our high-density model prediction with previous observations of other H I lines. Implicated effects on the nature of starburst in ULIRGs are stated in §4.4.4.

In this section, we use Einstein coefficients by Johnson (1972) and recombination coefficients by Verner & Ferland (1996).

4.4.1 Possible Causes of Anomaly

In order to investigate the H I line ratios, we should consider how the level populations of hydrogen atoms are determined. First we summarize three possible excitation mechanisms of hydrogen atoms: recombination, collisional excitation, and resonant excitation. Then we discuss possible explanation of the high $\text{Br}\beta/\text{Br}\alpha$ ratio in optically thin and thick cases separately.

4.4.1.1 Excitation Mechanisms of Hydrogen Atoms

As the first excitation mechanism, we discuss the recombination process. In the low density limit, where the collisional process is negligible, the hydrogen level populations are determined by recombination and radiative transitions. In this case, the equilibrium equation for a level population at a state with principal quantum number of \mathcal{N} is written as,

$$n_{\text{p}}n_{\text{e}}\alpha_{\mathcal{N}} + \sum_{\mathcal{N}'=\mathcal{N}+1}^{\infty} n_{\mathcal{N}'}A_{\mathcal{N}',\mathcal{N}} = n_{\mathcal{N}} \sum_{\mathcal{N}''=2}^{\mathcal{N}-1} A_{\mathcal{N},\mathcal{N}''}, \quad (4.1)$$

where n_{p} , n_{e} , and $n_{\mathcal{N}}$ are the number density of electrons, protons, and hydrogen atoms in quantum state of \mathcal{N} , respectively, $\alpha_{\mathcal{N}}$ is the recombination coefficient for \mathcal{N} , and $A_{\mathcal{N}',\mathcal{N}}$ is the Einstein A coefficient for the $\mathcal{N}' \rightarrow \mathcal{N}$ transition. We assume the case B condition

(Osterbrock & Ferland 2006), where the Lyman lines are assumed to be optically thick, so that the summation of the right-hand side ends at $\mathcal{N}'' = 2$. Using the cascade matrix $C_{\mathcal{N}',\mathcal{N}}$, which is the probability that population of \mathcal{N}' is followed by a transition to \mathcal{N} via all possible routes (Seaton 1959), Equation (4.1) is written as

$$n_{\mathcal{N}}A_{\mathcal{N}} = n_{\text{p}}n_{\text{e}} \sum_{\mathcal{N}'=\mathcal{N}}^{\infty} \alpha_{\mathcal{N}'}C_{\mathcal{N}',\mathcal{N}}, \quad (4.2)$$

where we write $\sum_{\mathcal{N}''=2}^{\mathcal{N}-1} A_{\mathcal{N},\mathcal{N}''}$ as $A_{\mathcal{N}}$. Thus we have

$$\frac{n_u}{n_l} = \frac{A_l \sum_{\mathcal{N}'=u}^{\infty} \alpha_{\mathcal{N}'}C_{\mathcal{N}',u}}{A_u \sum_{\mathcal{N}''=l}^{\infty} \alpha_{\mathcal{N}''}C_{\mathcal{N}'',l}} \quad (4.3)$$

for a level population of $\mathcal{N} = u$ and $\mathcal{N} = l$ states. The cascade matrix can be written down by the Einstein coefficients, which do not depend on gas properties such as temperature. The recombination coefficients weakly dependent on temperature, but in Equation (4.3), this dependence is almost canceled out because we have the coefficients both in the numerator and the denominator. Thus the level population is dependent on temperature weakly in the case that it is determined by the recombination process.

As the second excitation mechanism, we discuss the collisional process. In the high density limit, where the level population is entirely determined by the collisional process, the level population gets thermal equilibrium and follows the Boltzmann distribution. The ratio of the level populations in this case are written as

$$\frac{n_{\mathcal{N}}}{n_{\mathcal{N}'}} = \frac{g_{\mathcal{N}} \exp\left(-\frac{E_{\mathcal{N}}}{kT}\right)}{g_{\mathcal{N}'} \exp\left(-\frac{E_{\mathcal{N}'}}{kT}\right)}, \quad (4.4)$$

where $g_{\mathcal{N}}$ is the degeneracy of the \mathcal{N} state, k is the Boltzmann constant, $E_{\mathcal{N}}$ is the energy of the \mathcal{N} state relative to the ground state, and T is the gas temperature. Figure 4.9 shows the relative level population in several temperatures in this limit. The critical densities of the transitions of $\mathcal{N} = 1 \rightarrow 5$ and 6 are an order of $\sim 10^{11} \text{ cm}^{-3}$ (Storey & Hummer 1995), and so the gas density higher than this threshold is needed to realize the thermal equilibrium in those levels related to the Br α and Br β line emissions.

The third excitation mechanism is the resonant excitation. One example where this

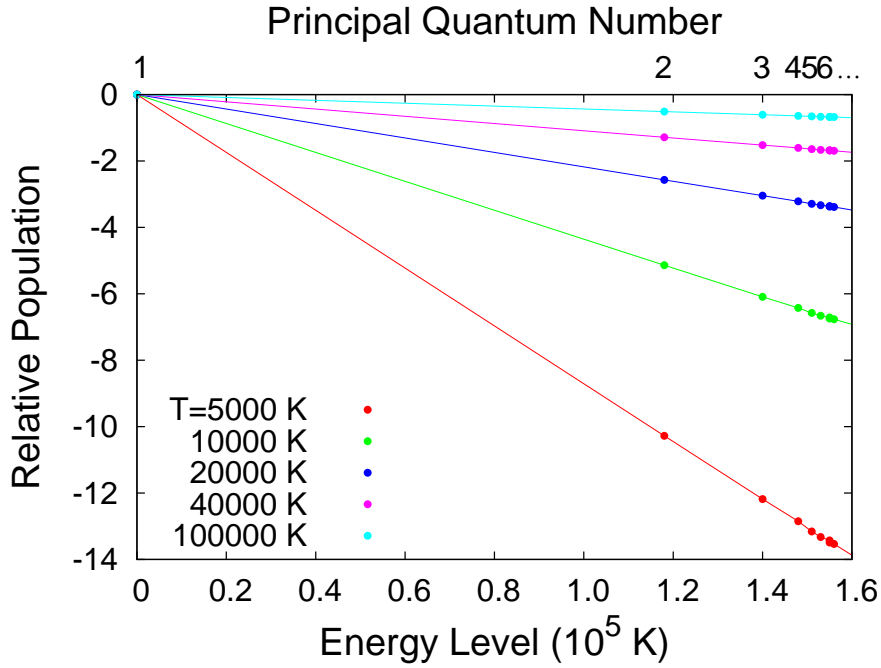


Figure 4.9. Relative level populations of hydrogen atom in thermal equilibrium.

process becomes important is the Bowen resonance of O III lines (Osterbrock & Ferland 2006). The wavelength of the O III $2p^2\ ^3P_2 - 3d^3\ ^3P_2^o$ line (303.80 Å) is accidentally coincident with that of the He II $L\alpha$ line (303.78 Å). The $3d^3\ ^3P_2^o$ level of O III is pumped with the He II $L\alpha$ line. This results in the enhancement of the O III lines originate from the $3d^3\ ^3P_2^o$ state. A similar situation would occur for hydrogen lines if a line whose wavelength is close to that of $\mathcal{N} = \mathcal{N}' \rightarrow 1$ transitions, i.e., the Lyman series, exists. In this case, the line pumps electrons of hydrogen in the ground state to the \mathcal{N}' state. This results in an enhancement of the level population of the \mathcal{N}' state.

Using the above three excitation mechanisms, we discuss possible explanations of the high $\text{Br}\beta/\text{Br}\alpha$ line ratio in the next section.

4.4.1.2 Optically Thin Case

We here consider the case that the Brackett lines are optically thin. In this case, once the level population of neutral hydrogen is determined, the flux ratios of H I lines are fixed.

The emergent Br β /Br α line ratio is expressed as

$$\frac{F_{\text{Br}\beta}}{F_{\text{Br}\alpha}} = \frac{n_6}{n_5} \frac{A_{\text{Br}\beta}}{A_{\text{Br}\alpha}} \frac{h\nu_{\text{Br}\beta}}{h\nu_{\text{Br}\alpha}} \sim 0.440 \frac{n_6}{n_5}, \quad (4.5)$$

where n_6/n_5 is the ratio of the level populations of hydrogen at $\mathcal{N} = 6$ and $\mathcal{N} = 5$, A_{line} is the Einstein A coefficient of the line, h is the Planck constant, and ν_{line} is the frequency of the line. This equation indicates that, in order to explain the high Br β /Br α line ratio, the level population at $\mathcal{N} = 6$ should be enhanced relative to that at $\mathcal{N} = 5$.

At low densities where the recombination process is dominant, the level population is determined by Equation (4.3). Assuming $T = 10000$ K as the gas temperature, we have $F_{\text{Br}\beta}/F_{\text{Br}\alpha} = 0.565$, i.e., the case B ratio, by substituting Equation (4.3) to Equation (4.5). On the other hand, in the high-density limit where the collisional process is dominant, the hydrogen level population is determined by Equation (4.4). Again, assuming $T = 10000$ K as the gas temperature, we have $F_{\text{Br}\beta}/F_{\text{Br}\alpha} = 0.522$ by substituting Equation (4.4) to Equation (4.5). If we take a limit of $T \rightarrow \infty$, Equation (4.4) gives $n_6/n_5 = g_6/g_5 = 1.44$ as the high- T limit. Even in this case, we have $F_{\text{Br}\beta}/F_{\text{Br}\alpha} = 0.634$, which is the highest line ratio achievable with the collisional excitation but is lower than the observed values. Thus, in both the high density and low density limits, we cannot explain the high Br β /Br α line ratio.

Generally speaking, the level population is affected both by the recombination and by the collisional process and so the combined results reside somewhere between the above two limits. This is expressed by the departure coefficient $b_{\mathcal{N}}$, which is the fractional departure of the population of the \mathcal{N} state from that of the Boltzmann distribution. We show $b_{\mathcal{N}}$ calculated by Peters et al. (2012) in Figure 4.10. For low \mathcal{N} states, Storey & Hummer (1995) calculated the $b_{\mathcal{N}}$ coefficients in several gas densities, and we show their result in Figure 4.11. The level populations at $\mathcal{N} = 6$ and $\mathcal{N} = 5$ is affected by the collisional process with densities higher than their critical density of $\sim 10^{11}$ cm $^{-3}$.

Using the $b_{\mathcal{N}}$ coefficient, we can estimate the n_6/n_5 ratio in each gas density, and so the Br β /Br α line ratio is derived from Equation (4.5). We show this result in Figure 4.12. At low densities, the Br β /Br α line ratio follows the case B ratio. When the density becomes $n \geq 10^{10}$ cm $^{-3}$, the collisional excitation starts to contribute to the $\mathcal{N} = 6$ state. This

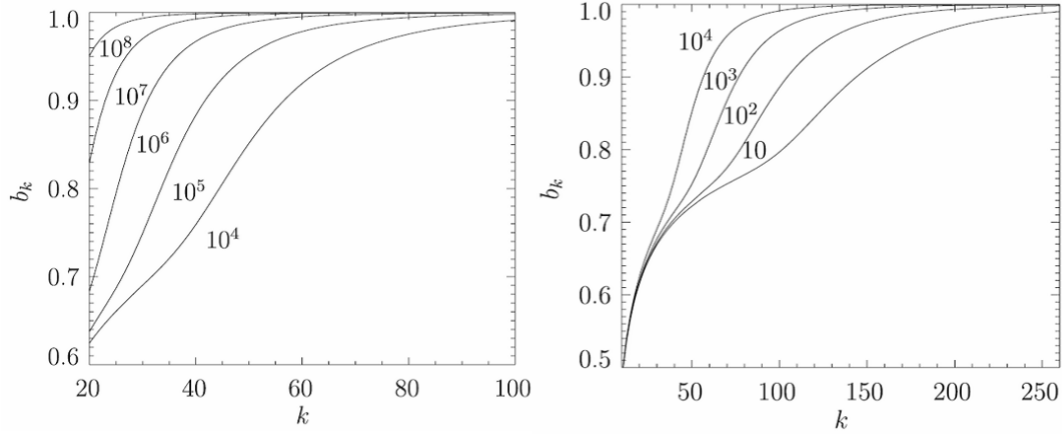


Figure 4.10. Departure coefficient for $\mathcal{N} \geq 20$ at $T = 10000$ K with the case B condition. The figures are taken from Peters et al. (2012). The principal quantum number is denoted as k .

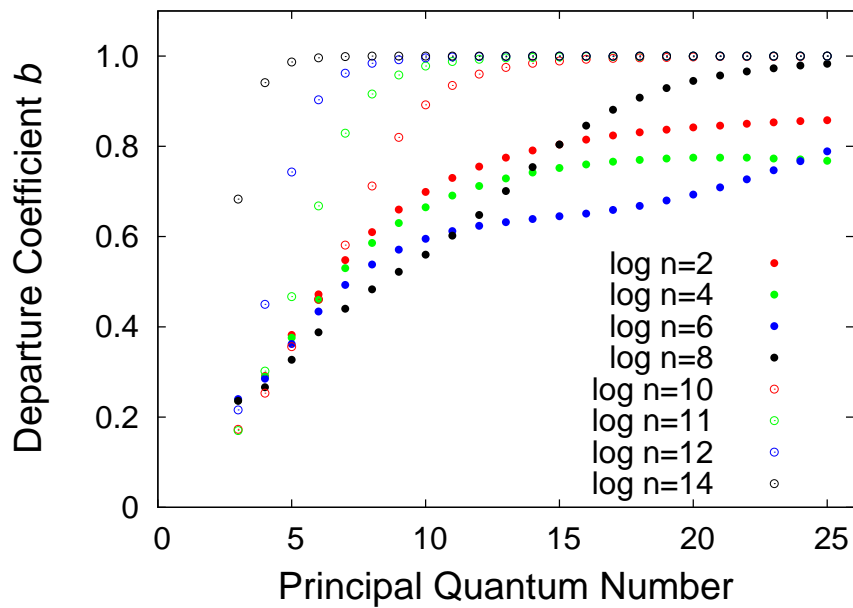


Figure 4.11. Departure coefficient for $\mathcal{N} \leq 25$ at $T = 10000$ K with the case B condition (data taken from Storey & Hummer 1995).

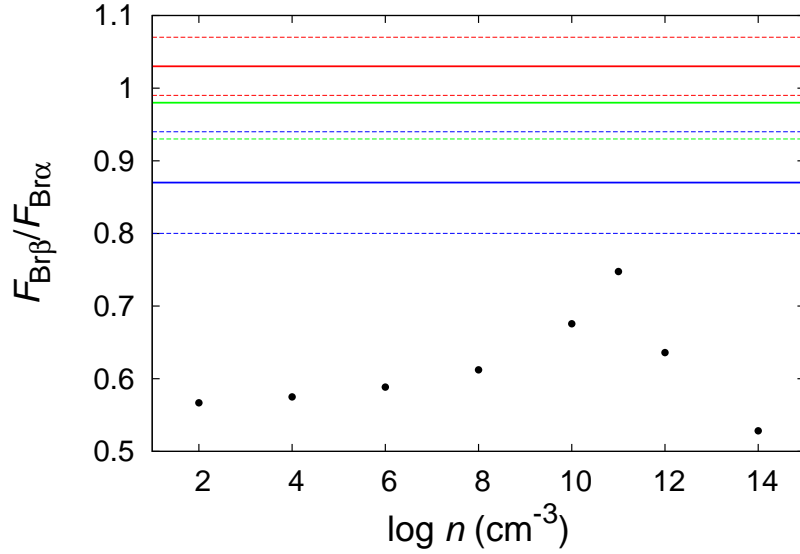


Figure 4.12. $F_{\text{Br}\beta}/F_{\text{Br}\alpha}$ ratio in the optically thin case. The red, green, and blue lines show the observed $F_{\text{Br}\beta}/F_{\text{Br}\alpha}$ ratio in Mrk 273, IRAS 10565+2448, and IRAS 10494+4424, respectively. The observed values are expressed by the solid lines, while the range of the 1σ uncertainty is shown by the dashed lines.

causes an enhancement of the Br β line. At higher densities of $n \geq 10^{12} \text{ cm}^{-3}$, the $\mathcal{N} = 5$ state begins to be collisionally excited, and so the Br β /Br α line ratio approaches the ratio in thermal equilibrium.

Figure 4.12 indicates that the Br β /Br α line ratio becomes as high as ~ 0.75 at $n \sim 10^{11} \text{ cm}^{-3}$. This ratio is within the 1.7σ uncertainty of the observed ratio in IRAS 10494+4424 (0.87 ± 0.07), but is still lower than those observed in IRAS 10565+2448 (0.98 ± 0.05) and Mrk 273 (1.03 ± 0.04) by more than 3σ uncertainty. Thus we conclude that we cannot explain the anomaly only with the recombination and the collisional process in the optically thin case.

With the resonant excitation, the $\mathcal{N} = 6$ state would be enhanced if a strong line with the wavelength of $\mathcal{N} = 6 \rightarrow 1$ (937.8 \AA) exists. We denote this line as X $_6$ and discuss its effect on the Br β /Br α line ratio. First we assume a case that hydrogen is excited only by this resonant excitation. Let x_6 to be the number of the resonance excitation per unit volume and unit time ($\text{cm}^{-3} \text{ s}^{-1}$), the number of the Br β transition ($\mathcal{N} = 6 \rightarrow 4$) caused by the resonant excitation is written as $x A_{6,4}/A_6 \sim 0.22x_6$. On the other hand, the number of the Br α transition ($\mathcal{N} = 6 \rightarrow 4$) is expressed as $x C_{6,5} C_{5,4} = 0.11x_6$. The Br β /Br α line

ratio is estimated to be $F_{\text{Br}\beta}/F_{\text{Br}\alpha} = 0.22x_6h\nu_{\text{Br}\beta}/0.11x_6h\nu_{\text{Br}\alpha} \sim 3.2$. Thus it is possible to make the line ratio consistent with our observation.

Next we discuss how strong the X_6 line is required to be to explain the observed anomaly. The level populations of $\mathcal{N} = 5$ and 6 are now written by taking the resonant excitation rate x_6 into consideration in Equation (4.2) as

$$\begin{aligned} n'_6 A_6 &= n_p n_e \sum_{\mathcal{N}'=6}^{\infty} \alpha_{\mathcal{N}'} C_{\mathcal{N}',6} + x_6, \\ \therefore n'_6 &= n_p n_e \frac{\sum_{\mathcal{N}'=6}^{\infty} \alpha_{\mathcal{N}'} C_{\mathcal{N}',6}}{A_6} + \frac{x_6}{A_6} \end{aligned} \quad (4.6)$$

and

$$\begin{aligned} n'_5 A_5 &= n_p n_e \sum_{\mathcal{N}'=6}^{\infty} \alpha_{\mathcal{N}'} C_{\mathcal{N}',5} + C_{6,5} x_6, \\ \therefore n'_5 &= n_p n_e \frac{\sum_{\mathcal{N}'=5}^{\infty} \alpha_{\mathcal{N}'} C_{\mathcal{N}',5}}{A_5} + \frac{C_{6,5} x_6}{A_5}. \end{aligned} \quad (4.7)$$

In order to explain the observed anomaly of $F_{\text{Br}\beta}/F_{\text{Br}\alpha} \sim 1$, a level population of $n'_6/n'_5 \sim 2.27$ is required. With Equations (4.6) and (4.7), this is expressed as

$$\begin{aligned} n_p n_e \frac{\sum_{\mathcal{N}'=6}^{\infty} \alpha_{\mathcal{N}'} C_{\mathcal{N}',6}}{A_6} + \frac{x_6}{A_6} &= 2.27 \left(n_p n_e \frac{\sum_{\mathcal{N}'=5}^{\infty} \alpha_{\mathcal{N}'} C_{\mathcal{N}',5}}{A_5} + \frac{C_{6,5} x_6}{A_5} \right), \\ \therefore x_6 &= 2.29 \times 10^{-14} \left(\frac{n}{\text{cm}^{-3}} \right)^2 \text{ cm}^{-3} \text{ s}^{-1}. \end{aligned} \quad (4.8)$$

We here approximate $n_e n_p \sim n^2$, where n is the total hydrogen number density, i.e., we write n as $n(\text{H}^0) + n(\text{H}^+)$, where $n(\text{H}^0)$ and $n(\text{H}^+)$ are the number density of neutral and ionized hydrogen, respectively. We assume all photons emitted by the X_6 line are absorbed by hydrogen atoms. On the basis of this assumption, x_6 is equal to the emission rate of the X_6 line. We write the rate as $n \xi_X f_{X_6} A_{X_6}$, where ξ_X is the abundance of the atom emitting the X_6 line relative to hydrogen, f_{X_6} is a fraction of excited atoms which can radiate the X_6 line to those at other states, and A_{X_6} is an Einstein A coefficient of the X_6 line. From Equation (4.8), A_{X_6} is estimated as

$$A_{X_6} = 2.29 \times 10^{-14} f_{X_6}^{-1} \xi_X^{-1} \left(\frac{n}{\text{cm}^{-3}} \right) \text{ s}^{-1}. \quad (4.9)$$

It is difficult to estimate the fraction f_{X_6} , and we here assume the most extreme case that it is an order of unity to take weak lines into consideration. At gas density of $n = 10^3 \text{ cm}^{-3}$, on the assumption that the atom have an abundance similar to that of metal elements of $\xi_X \sim 10^{-4}$, A_{X_6} is estimated to be $\sim 10^{-7} \text{ s}^{-1}$, which is close to those of forbidden lines. This indicates that if a line with a wavelength of $\sim 937.8 \text{ \AA}$ and a transition probability of the order of that for forbidden lines exists, the resonant process would make the $\text{Br}\beta/\text{Br}\alpha$ line ratio anomalous.

We investigate atomic and molecular data known to date to search possible resonant lines. As the line data, we refer a line list provided in the Cloudy simulation (Ferland et al. 1998). Cloudy is a spectral synthesis code designed to numerically simulate an astrophysical plasma and its emission. Atomic and molecular data are extensively collected in the code (references are available in a file distributed along with the code). We search possible resonant lines with a wavelength of $\sim 937.8 \text{ \AA}$ within a velocity range of $\sim 10 \text{ km s}^{-1}$, which corresponds to the thermal velocity at $T = 10000 \text{ K}$ (Osterbrock & Ferland 2006). We find no candidates in the Cloudy data. Thus we exclude this resonant process from possible causes of the anomaly of the $\text{Br}\beta/\text{Br}\alpha$ line ratio.

In summary, we conclude that we cannot explain the anomaly of the $\text{Br}\beta/\text{Br}\alpha$ line ratio in the case that the Brackett lines are optically thin.

4.4.1.3 Optically Thick Case

The other case is that the Brackett lines become optically thick, and the observed line ratio is altered from Equation (4.5). In this case, it is possible to explain the high $\text{Br}\beta/\text{Br}\alpha$ line ratio if the $\text{Br}\alpha$ line gets optically thick and saturated while the $\text{Br}\beta$ line is still optically thin. We discuss the optical depth effect on the ratio in this section.

Optical Depth of Brackett Lines

On the assumption of uniform gas, the line optical depth at the line center for a transition $\mathcal{N} = u \rightarrow l$, $\tau_{u,l}$, is expressed as

$$\tau_{u,l} = \int_0^R \alpha_{l,u} n_l dl \sim \alpha_{l,u} N_l, \quad (4.10)$$

where R is the size of gas, $\alpha_{l,u}$ is the absorption cross section of the $l \rightarrow u$ transition, n_l is the number density of neutral hydrogen at the $\mathcal{N} = l$ state, and N_l is the column density of neutral hydrogen at the $\mathcal{N} = l$ state. The optical depth of the Brackett lines is proportional to the column density of neutral hydrogen at the quantum state of $\mathcal{N} = 4$.

The absorption cross section is related to the Einstein B coefficient, $B_{l,u}$, by

$$\alpha_{l,u} = \frac{hc}{4\pi^{3/2}} \frac{B_{l,u}}{v_{\text{Dop}}}, \quad (4.11)$$

where c is the speed of light, and v_{Dop} is the Doppler velocity half width, the point where the line profile falls to $1/e$ of its peak. If the line profile is determined only by the thermal motion, the width is written as $v_{\text{Dop}} = v_{\text{Therm}} = \sqrt{2kT/m_{\text{H}}}$, where m_{H} is the mass of hydrogen atom. At $T = 10000$ K, v_{Therm} is estimated to be ~ 13 km s $^{-1}$. If a turbulent motion with a velocity of v_{Turb} affects the line width, v_{Dop} is written as $\sqrt{v_{\text{Therm}}^2 + v_{\text{Turb}}^2}$.

Substituting Equation (4.11) to Equation (4.10), and assuming $T = 10000$ K, we obtain the line optical depths of the Br α and Br β lines as

$$\tau_{\text{Br}\alpha} \sim 6.3 \left(\frac{N_4}{10^{12} \text{ cm}^{-2}} \right) \left(\frac{v_{\text{Dop}}}{10 \text{ km s}^{-1}} \right)^{-1}, \quad (4.12)$$

$$\tau_{\text{Br}\beta} \sim 7.1 \left(\frac{N_4}{10^{13} \text{ cm}^{-2}} \right) \left(\frac{v_{\text{Dop}}}{10 \text{ km s}^{-1}} \right)^{-1}. \quad (4.13)$$

Thus, on the assumption of $v_{\text{Dop}} \sim 10$ km s $^{-1}$ for instance, the Br α line becomes optically thick while the Br β line is still optically thin in the conditions with $N_4 \sim 2 \times 10^{11}$ cm $^{-2}$. We discuss possible conditions which make the high Br β /Br α line ratio on the basis of Equations (4.12) and (4.13).

Possible Conditions Making High Br β /Br α Line Ratio

We here make an assumption that the high Br β /Br α line ratio is produced within a single isolated H II region ionized by a single star, and what we observe is an ensemble of such H II regions. Within a single H II region, we assume that v_{Dop} is determined only by the thermal width v_{Therm} of the order of ~ 10 km s $^{-1}$, which is a typical velocity observed in nearby H II regions (e.g., Arthur et al. 2016). We assume that the Br α line becomes optically thick within each H II regions.

We consider a spherical and uniform H II region and discuss how to make the Br α line optically thick with the three excitation mechanisms described in §4.4.1.1. First, we consider the case in which the recombination process is dominant. In this case, n_4 is estimated by Equation (4.2) as $\sim 3.6 \times 10^{-21} (n/\text{cm}^{-3})^2 \text{ cm}^{-3}$, and so we can write N_4 with n and R as

$$N_4 = n_4 R \sim 3.6 \times 10^{-21} \left(\frac{n}{\text{cm}^{-3}} \right)^2 \left(\frac{R}{\text{cm}} \right) \text{ cm}^{-2}. \quad (4.14)$$

If we write $nR = N$, where N is the total hydrogen column density, then we have

$$N_4 = 3.6 \times 10^{-21} \left(\frac{n}{\text{cm}^{-3}} \right) \left(\frac{N}{\text{cm}^{-2}} \right) \text{ cm}^{-2}. \quad (4.15)$$

Thus N_4 is proportional to n as well as N . We now assume that a H II region is ionized by a central star with a number of ionizing photons per unit time of $Q(\text{H})$. On the assumption of ionizing equilibrium and $T = 10000 \text{ K}$, we have

$$\begin{aligned} Q(\text{H}) &= \int \alpha_{\text{B}} n_e n_{\text{p}} dV \sim \frac{4\pi}{3} \alpha_{\text{B}} n^2 R^3 = \frac{4\pi}{3} \alpha_{\text{B}} N^3 n^{-1} \\ \therefore N &= 3.37 \times 10^{20} \left(\frac{Q(\text{H})}{10^{49} \text{ s}^{-1}} \right)^{\frac{1}{3}} \left(\frac{n}{\text{cm}^{-3}} \right)^{\frac{1}{3}} \text{ cm}^{-2}, \end{aligned} \quad (4.16)$$

where α_{B} is the total recombination coefficient of hydrogen in case B, and $Q(\text{H}) = 10^{49} \text{ s}^{-1}$ is a typical value of a O star (Osterbrock & Ferland 2006). Substituting Equation (4.16) with (4.15), we can write N_4 with n and $Q(\text{H})$ as

$$N_4 = 2.35 \times 10^{11} \left(\frac{Q(\text{H})}{10^{49} \text{ s}^{-1}} \right)^{\frac{1}{3}} \left(\frac{n}{10^8 \text{ cm}^{-3}} \right)^{\frac{4}{3}} \text{ cm}^{-2}. \quad (4.17)$$

Thus within a single H II region with an ionizing source of $Q(\text{H}) \sim 10^{49} \text{ s}^{-1}$, gas density as high as $n \sim 10^8 \text{ cm}^{-3}$ is required to achieve the column density of $N_4 \sim 2 \times 10^{11} \text{ cm}^{-2}$ large enough to make the Br α line optically thick.

At the density of $n = 10^8 \text{ cm}^{-3}$, the collisional process is not dominant for the population at the quantum state of $\mathcal{N} = 4$ because the critical density of the $\mathcal{N} = 1 \rightarrow 4$ transition is $\sim 10^{12} \text{ cm}^{-3}$ (Storey & Hummer 1995). This is also shown in Figure 4.11.

The relative difference of b_4 coefficients at $n = 10^8 \text{ cm}^{-3}$ and at 10^2 cm^{-3} is less than 10% and indicates that the $\mathcal{N} = 4$ state is not dominantly populated by the collisional process at the density of $n \leq 10^8 \text{ cm}^{-3}$. Thus the relation of Equation (4.17), in which only the recombination process is considered, is valid if we take the collisional excitation into consideration at the density of $n = 10^8 \text{ cm}^{-3}$.

The resonant excitation would enhance the $\mathcal{N} = 4$ state if a line with the wavelength of $\mathcal{N} = 4 \rightarrow 1$ (972.5 Å) exists. In this case, the required density of $n \sim 10^8 \text{ cm}^{-3}$ in Equation (4.17) to make the Br α line optically thick would be lowered. We denote the possible resonant line as X_4 and write the rate of the resonant excitation by the X_4 line as x_4 ($\text{cm}^{-3} \text{ s}^{-1}$). From Equation (4.2), the $\mathcal{N} = 4$ state is populated by the recombination process with a rate of $n_e n_p \sum_{\mathcal{N}'=4}^{\infty} \alpha_{\mathcal{N}'} C_{\mathcal{N}',4} \sim 6.2 \times 10^2 \text{ cm}^{-3} \text{ s}^{-1}$ at $n = 10^8 \text{ cm}^{-3}$. This indicates that if x_4 is larger than $\sim 10^3 \text{ cm}^{-3} \text{ s}^{-1}$, the resonant process significantly populates the $\mathcal{N} = 4$ state in the condition with $n = 10^8 \text{ cm}^{-3}$.

In the same way as the case of the $\mathcal{N} = 1 \rightarrow 6$ resonance we discuss in §4.4.1.2, we estimate the transition probability of the X_4 line, A_{X_4} , required to make the resonant process dominant for the $\mathcal{N} = 4$ population. We assume that all photons emitted by the X_4 line is absorbed by hydrogen, so that x_4 is equal to the rate of the emission of the X_4 line, $n \xi_X f_{X_4} A_{X_4}$, where ξ_X is an abundance of the atom emitting the X_4 line relative to hydrogen, and f_{X_4} is a fraction of excited atoms which can radiate the X_4 line to those at other states. We here assume f_{X_4} is an order of unity as the most extreme case. At gas density of $n = 10^8 \text{ cm}^{-3}$, on the assumption that the atom have an abundance similar to that of metal elements of $\xi_X \sim 10^{-4}$, A_{X_4} is estimated to be $\sim 10^{-1} \text{ s}^{-1}$. Thus if a line with a wavelength of $\sim 972.5 \text{ Å}$ and a transition probability of $\sim 10^{-1} \text{ s}^{-1}$ exists, we should take the resonant process into consideration for the determination of the population of the $\mathcal{N} = 4$ state.

We search possible resonant lines with a wavelength of $\sim 972.5 \text{ Å}$ within a velocity range of $\sim 10 \text{ km s}^{-1}$, which corresponds to the thermal velocity at $T = 10000 \text{ K}$ (Osterbrock & Ferland 2006) in the line list of the Cloudy code (Ferland et al. 1998) and find no candidates for the X_4 line. Thus we conclude that the resonant process discussed above does not take place and is excluded from the excitation mechanisms of the $\mathcal{N} = 4$ state.

Simulation with Cloudy

In order to quantitatively investigate the $\text{Br}\beta/\text{Br}\alpha$ line ratio with taking all excitation mechanisms into consideration, we use the Cloudy code (ver. 10.00; Ferland et al. 1998) and simulate the ratio in the optically thick case. Cloudy calculates the recombination and the collisional process altogether. Cloudy also solves radiative transfer of lines and so can be used to investigate the effect of optical depth on the line fluxes.

To execute a simulation with Cloudy, four parameters are required: (1) the spectral shape of the incident radiation, (2) the intensity of the incident radiation, (3) the density of surrounding gas, and (4) the criteria for stopping the calculation. We consider a single spherical H II region with uniform gas ionized by a central hot star. For the spectral shape of the incident radiation (1), we use 40000 K blackbody radiation to simulate a typical O star (Osterbrock & Ferland 2006). As the intensity of the incident radiation (2), we specify the number of ionizing photons per unit time, $Q(\text{H})$. We vary $Q(\text{H})$ from 10^{48} s^{-1} to 10^{51} s^{-1} with intervals of a decade on the assumption that the ionizing radiation is dominated by heavy OB stars in starburst regions. The $Q(\text{H})$ values of 10^{48} s^{-1} , 10^{49} s^{-1} , and 10^{50} s^{-1} correspond to the typical values of B stars, O5 stars, and heavy O stars (O3 stars), respectively (Osterbrock & Ferland 2006). We also calculate the case of $Q(\text{H}) = 10^{51} \text{ s}^{-1}$ for reference. The gas density (3) is also varied from $n = 10^5 \text{ cm}^{-3}$ to 10^{10} cm^{-3} with intervals of a decade. In order to simulate line emissions from the ionized region, we adopt a electron fraction to the total gas, i.e., ionization degree, of 0.1 for the stopping criteria of one calculation (4). In addition to the above parameters, we specify a spherical geometry and a inner radius of surrounding gas, which is required in Cloudy when we use $Q(\text{H})$ as the intensity of the incident radiation, of $r = 10^{12} \text{ cm}$. We also make the calculations iterate until the difference of the line optical depths between the last two iterations become smaller than 0.20. The adopted parameters described above are summarized in Table 4.5. Other parameters are set to be the default values of Cloudy, e.g., the line width is determined by the thermal velocity, the solar abundances are adopted, and dust grains are not included in the calculations.

The result of the Cloudy simulations of the $\text{Br}\beta/\text{Br}\alpha$ line ratio is shown in Figure 4.13. We find that the $\text{Br}\beta/\text{Br}\alpha$ line ratio becomes high in the conditions with high n and N .

Table 4.5. Parameters Used in Cloudy Simulations^a

Parameter	Value	Description
Blackbody	40000 K	Spectral shape of incident radiation.
$\log Q(\text{H})^{\text{b}}$	48–51	Intensity of incident radiation.
$\log r^{\text{c}}$	12	Inner radius of surrounding gas.
$\log n^{\text{d}}$	5–10	Density of surrounding gas.
Stop Efrac ^e	–1	Stop criteria for calculation.
Sphere	...	Geometry of surrounding gas.
Iterate to Convergence ^f	0.20	Stop criteria for iteration.

^aAll inputted parameters we used for the calculations are listed. Other parameters were set to the default values of Cloudy.

^bLog of the number of ionizing photons in s^{-1} .

^cLog of the inner radius of gas in cm.

^dLog of the total hydrogen number density of gas in cm^{-3} .

^eLog of the electron fraction below which one calculation stops.

^fMaking the calculation iterate until the difference of optical depths between the last two iteration becomes smaller than the specified value.

On the other hand, the ratio is close to the case B value (0.565) in the low n and N conditions. This result follows our simple estimation that the high $\text{Br}\beta/\text{Br}\alpha$ line ratio is produced when the $\text{Br}\alpha$ line becomes optically thick, and the optical depth of the $\text{Br}\alpha$ line is proportional to N_4 , which is proportional to n and N as shown in Equation (4.15). We now compare the observed $\text{Br}\beta/\text{Br}\alpha$ line ratio with the Cloudy results. Figure 4.13 indicates that the observed ratio in the three galaxies is explained in the conditions with $n \sim 10^8 \text{ cm}^{-3}$, where the $\text{Br}\alpha$ line starts to become optically thick. In conditions with higher n , the $\text{Br}\beta/\text{Br}\alpha$ line ratio becomes too high to explain the observed anomaly. On the basis of this result, we conclude that in order to explain the observed $\text{Br}\beta/\text{Br}\alpha$ line ratio within a single H II region, gas density as high as $n \sim 10^8 \text{ cm}^{-3}$ is required to achieve column density large enough to make the $\text{Br}\alpha$ line optically thick.

Next, we discuss an ensemble of H II regions, each of which is represented by the high-density model, to explain the observed luminosity of the $\text{Br}\alpha$ line. We summarize the observed luminosity of the $\text{Br}\alpha$ line in the three galaxies with the high $\text{Br}\beta/\text{Br}\alpha$ line ratio

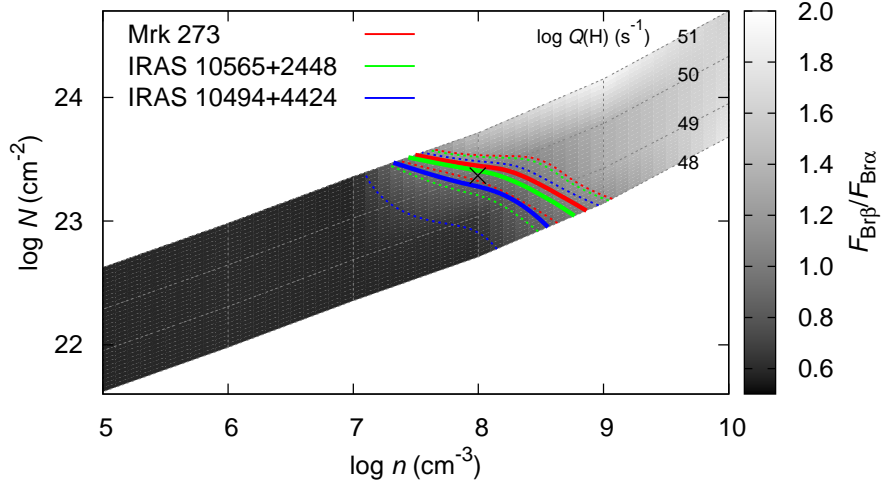


Figure 4.13. Cloudy result of the Br β /Br α line ratio. $Q(\text{H})$ and n are varied within the ranges of $10^{48} \text{ s}^{-1} \leq Q(\text{H}) \leq 10^{51} \text{ s}^{-1}$ and $10^5 \text{ cm}^{-3} \leq n \leq 10^{10} \text{ cm}^{-3}$ with the intervals of a decade. The Br β /Br α line ratio is shown as the gray scale. The observed Br β /Br α line ratios of Mrk 273, IRAS 10565+2448, and IRAS 10494+4424 are presented as the red, green, and blue lines, respectively. The observed value is shown by the solid lines, and the range of the 3σ uncertainties are indicated by the dotted lines. The model calculated with $Q(\text{H}) = 10^{50} \text{ s}^{-1}$ and $n = 10^8 \text{ cm}^{-3}$ is indicated by the black cross.

in Table 4.6. In the high-density model, the luminosity of the Br α line produced by a single H II region is estimated to be $L_{\text{Br}\alpha}^{\text{Model}} = 2.79 \times 10^{36} \text{ erg s}^{-1}$, and we estimate the number of H II regions k_{tot} as shown in Table 4.6. From this result, we conclude that $\sim 10^5$ H II regions with the high-density condition are required to explain our observation.

We here make an order estimation of the expected number of H II regions in the line of sight k_{los} to determine the effect of optical depth on the line emitted from a single H II region and intercepted by other H II regions. We assume a volume filling factor of $\varepsilon \sim 10^{-6}$, which is a typical value of H II regions observed in starburst galaxies (Anantharamaiah et al. 1993). We also assume that H II regions are uniformly and spherically distributed. We assume that k_{los} is represented by the number of H II region in the line of sight from the center of the line emitting region. Then, the typical radius of the line emitting region is represented by $k_{\text{los}}/\varepsilon$ while the volume is expressed by $k_{\text{tot}}/\varepsilon$. From this relation, we have

$$\left(\frac{k_{\text{los}}}{\varepsilon}\right)^3 \sim \frac{k_{\text{tot}}}{\varepsilon}, \quad \therefore \quad k_{\text{los}} \sim k_{\text{tot}}^{\frac{1}{3}} \varepsilon^{\frac{2}{3}}. \quad (4.18)$$

Table 4.6. Comparison of Luminosity with High-Density Model

Object Name	$L_{\text{Br}\alpha}$ (10^{41} erg s $^{-1}$)	$k_{\text{tot}}^{\text{a}}$ (10^4)
IRAS 10494+4424	2.68 ± 0.14	9.6
IRAS 10565+2448	1.62 ± 0.05	5.8
Mrk 273	1.48 ± 0.04	5.3

^aThe number of H II regions represented by the high-density model required to explain the observed luminosity of the Br α line.

By substituting $k_{\text{tot}} = 10^5$ and $\varepsilon = 10^{-6}$ into Equation (4.18), we obtain $k_{\text{los}} \sim 10^{-7/3}$. We assume the relative velocity of H II regions of the order of ~ 100 km s $^{-1}$, which is a typical line velocity observed in galaxies (e.g., Osterbrock & Ferland 2006) and is an order of magnitude higher than the thermal velocity. Then the optical depth of the Br α line caused by intercepting H II regions is estimated to be three orders of magnitude smaller than that in an H II region where the line originates. Thus we conclude that the line ratio produced in a single H II region is not affected by other H II regions even if we consider an ensemble of $\sim 10^5$ H II regions.

We propose an ensemble of H II regions, in each of which the Br α line is optically thick, can explain the high Br β /Br α line ratio. The high Br β /Br α line ratio is produced within each of H II regions, and what we observe is a collection of such H II regions. To achieve the column density large enough to make the Br α line optically thick within a single H II region, the gas density as high as $n \sim 10^8$ cm $^{-3}$ is required.

Single Giant H II Region Model

We here consider another simplified model in which the line emitting region is not a collection of H II regions but a single giant H II region where all the ionizing stars are concentrated at the center of uniform gas. We discuss whether the high Br β /Br α line ratio is produced within such a giant H II region by the optical depth effect.

We have shown that ionizing sources with $Q(\text{H})$ of the order of $\sim 10^{55}$ s $^{-1}$ are required to explain the observed luminosity of the Br α line. Thus here we also assume a central ion-

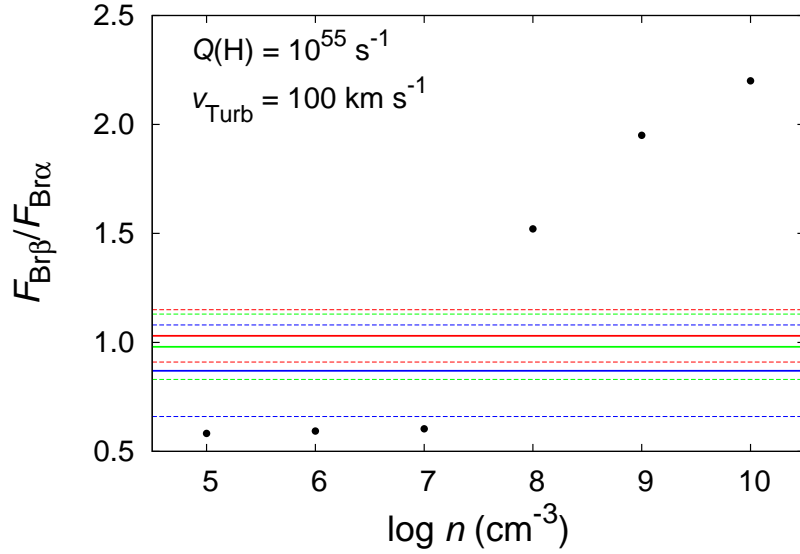


Figure 4.14. Cloudy result of the Br β /Br α line ratio with $Q(\text{H}) = 10^{55} \text{ s}^{-1}$ and $v_{\text{Turb}} = 100 \text{ km s}^{-1}$. The red, green, and blue lines show the observed $F_{\text{Br}\beta}/F_{\text{Br}\alpha}$ ratio in Mrk 273, IRAS 10565+2448, and IRAS 10494+4424, respectively. The observed values are expressed by the solid lines, while the range of the 3σ uncertainty is shown by the dashed lines.

izing source of $Q(\text{H}) = 10^{55} \text{ s}^{-1}$, which corresponds to 10^5 – 10^6 OB stars. As a turbulence velocity within the giant H II region, we assume $v_{\text{Turb}} = 100 \text{ km s}^{-1}$. In this condition, Equation (4.12) indicates that $N_4 \sim 2 \times 10^{12} \text{ cm}^{-2}$ is required to make the Br α line optically thick. Substituting $N_4 = 2 \times 10^{12} \text{ cm}^{-2}$ and $Q(\text{H}) = 10^{55} \text{ s}^{-1}$ for Equation (4.17), we obtain $n \sim 2 \times 10^7 \text{ cm}^{-3}$ for the gas density required to make the Br α line optically thick within the giant H II region.

In order to investigate the Br β /Br α line ratio quantitatively in this case, we again use the Cloudy code to simulate the giant H II region. Most of the parameters are the same as those tabulated in Table 4.5 except that $Q(\text{H})$ is fixed at 10^{55} s^{-1} , and $v_{\text{Turb}} = 100 \text{ km s}^{-1}$ is considered. We show the Cloudy results in Figure 4.14. The observed Br β /Br α line ratio is explained with gas density within the range of $n = 10^7$ – 10^8 cm^{-3} . The luminosity of the Br α line estimated in these conditions is $L_{\text{Br}\alpha} \sim 2$ – $4 \times 10^{41} \text{ erg s}^{-1}$. We confirm that this well agrees with the observed value. We conclude that gas density as high as $n \sim 10^7$ – 10^8 cm^{-3} is also required to explain the observed Br β /Br α line ratio in the other extreme case that the line emitting region is a single giant H II region with the central ionizing source of $Q(\text{H}) = 10^{55} \text{ s}^{-1}$.

There is one caveat in the Cloudy result shown in Figure 4.14. With $Q(\text{H}) = 10^{55} \text{ s}^{-1}$, the electron column density within the H II region exceeds $N_e \sim 2 \times 10^{24} \text{ cm}^{-2}$ in conditions with $n \geq 10^8 \text{ cm}^{-3}$, and so the H II region becomes Compton thick. The Cloudy code is not designed to simulate Compton-thick regimes (Ferland et al. 1998), and so the validity of the result is not guaranteed in those conditions. The process of the Thomson scattering does not include any energy transferring effect. Thus we expect that the result of the emergent line ratio is still valid even if the H II region becomes Compton thick.

In summary, we propose that we can explain the high $\text{Br}\beta/\text{Br}\alpha$ line ratio with the optical depth effect. We consider two extreme cases as line emitting regions: an ensemble of an H II region ionized by a single star and a giant H II region where all the ionizing stars are concentrated at the center. In both the cases, we conclude that the gas density as high as $n \sim 10^8 \text{ cm}^{-3}$ is required to achieve the column density of neutral hydrogen large enough to make the $\text{Br}\alpha$ line optically thick. We propose this high-density scenario as the most plausible cause of the high $\text{Br}\beta/\text{Br}\alpha$ line ratio.

As a reference model explaining the observed $\text{Br}\beta/\text{Br}\alpha$ line ratio, we adopt an ensemble model in which each H II regions are represented by the Cloudy result calculated under the condition of $n = 10^8 \text{ cm}^{-3}$ and $Q = 10^{50} \text{ s}^{-1}$. This high-density model represents an ensemble of an H II region ionized by an O3 star with the high gas density. The $\text{Br}\beta/\text{Br}\alpha$ line ratio in this model (0.929) well explains the observed values in IRAS 10494+4424, IRAS 10565+2448, and Mrk 273 of 0.87 ± 0.07 , 0.98 ± 0.05 , and 1.03 ± 0.04 , respectively.

4.4.2 The Expected Number of High-Density H II Regions in ULIRGs

Our model requires $\sim 10^5$ H II regions with high-density gas of $n \sim 10^8 \text{ cm}^{-3}$ to explain the high $\text{Br}\beta/\text{Br}\alpha$ line ratio. Here we discuss the possibility to observe such a number of high-density H II regions in ULIRGs in comparison with ultracompact H II regions in our Galaxy.

Ultracompact H II regions in our Galaxy (e.g., Kurtz 2000; Churchwell 2002) are reported to have high-density gas up to $n \sim 10^7 \text{ cm}^{-3}$ and sizes of the order of 10^{-2} pc (e.g., de Pree et al. 1995). The density and the size of the ultracompact H II regions are comparable to those of the high-density H II regions required in our model. We thus consider

the high-density H II regions in our model as analogous objects of the ultracompact H II regions in our Galaxy.

A simple estimate of a lifetime of H II regions at the ultracompact state with a size of $r \sim 10^{-2}$ pc is given by dividing r by the sound speed of the ionized material v_s (~ 10 km s $^{-1}$ at $T = 10000$ K) on the assumption that H II regions expand at velocities comparable with v_s . This yields a lifetime of $r/v_s \sim 10^3$ yr for the ultracompact H II regions in our Galaxy. On the other hand, the number of the ultracompact H II regions is estimated to be $\sim 10^3$ in our Galaxy (Churchwell 2002). Adopting a formation rate of O stars of $\sim 10^{-2}$ stars yr $^{-1}$ in our Galaxy (de Pree et al. 1995), the lifetime of the ultracompact H II regions are estimated to be $\sim 10^5$, which is two orders of magnitude longer than that estimated by assuming the simple expansion of H II regions. This large difference of the lifetime is recognized as a “lifetime problem” first mentioned by Wood & Churchwell (1989) and still remains an open question (e.g., Kurtz 2000; Churchwell 2002). Here we simply adopt the observed lifetime of $\sim 10^5$ yr as the representative lifetime of the ultracompact H II regions.

We assume that the high-density H II regions required in our high-density model have a lifetime of the same order ($\sim 10^5$ yr) of that of the ultracompact H II regions in our Galaxy. Here we consider the fact that the SFR in ULIRGs is about two orders of magnitude higher than that in our Galaxy (Sanders et al. 1988). Scaling the number of the ultracompact H II regions observed in our Galaxy ($\sim 10^3$; Churchwell 2002) with the SFR, we expect that the number of high-density H II regions is an order of $\sim 10^5$ in ULIRGs. Thus we propose that it is possible to observe $\sim 10^5$ high-density H II regions in ULIRGs as our model predicts.

After $\sim 10^5$ yr lifetime of the ultracompact phase, the gas density of H II regions is expected to become lower than $\sim 10^7$ cm $^{-3}$ with expansion of H II regions (de Pree et al. 1995). The typical lifetime of O stars is an order of 10^6 yr (Osterbrock & Ferland 2006), which is an order of magnitude longer than that of the ultracompact H II regions. Thus the number of H II regions with the gas density lower than $\sim 10^7$ cm $^{-3}$ is expected to be an order of magnitude larger than that of the ultracompact H II regions. However, to explain the high Br β /Br α line ratio, our model requires that most H II regions are in

the ultracompact phase. Our results indicate that some mechanism is required to keep Brackett lines from H II regions in ULIRGs dominated by those from ultracompact H II regions.

4.4.3 Comparison with Other Hydrogen Recombination Lines

The high-density model predicts that the H I line ratios of not only the Br β /Br α line but also other ratios deviate from the case B values. We here compare this prediction with other observations of H I lines.

4.4.3.1 Comparison with H α Line

The H α line ($\mathcal{N} = 3 \rightarrow 2$, 6563 Å) is one of the most intensively observed H I line because it is in the optical wavelength and so is easily observable from ground-based telescopes. We here compare the fluxes of the Brackett lines and the H α line in the three ULIRGs, IRAS 10494+4424, IRAS 10565+2448, and Mrk 273, which show the high Br β /Br α line ratio.

When we compare line fluxes obtained from different observations, aperture matching becomes important for a fair comparison. Our *AKARI* observation employs the slitless spectroscopy, and we used the aperture width of $\sim 7''$ to extract the near-infrared spectra.

IRAS 10565+2448 was observed with the integral field unit on Gemini North telescope by Shih & Rupke (2010). They reported a integrated H α line flux of $F_{\text{H}\alpha} = (8.42 \pm 0.84) \times 10^{-14} \text{ erg s}^{-1} \text{ cm}^{-2}$ (before extinction correction) within an aperture of $5'' \times 7''$ in this galaxy. We adopt this flux for the comparison with our result.

For IRAS 10494+4424 and Mrk 273, we conducted a narrowband imaging observation of the H α line to obtain its flux within an aperture of $7''$ diameter. We performed the narrowband imaging observation of the optical H α line with the Nickel 40-inch telescope at Lick observatory. The observation was performed on 2014 November 26. The observational method was the same as described in Theios et al. (2016). The sky was clear with seeing of $\sim 2''$ FWHM. We used the Nickel Direct Imaging Camera (CCD-C2), which has 2048 \times 2048 pixels, read out with 2×2 binning, to yield 1024 \times 1024 pixels $0''.37$ on a side. The observed wavelength of the H α line was 7167 Å at redshift of IRAS 10494+4424 ($z = 0.092$)

Table 4.7. Observed H α Line Flux

Object	$F_{\text{H}\alpha}$ (10^{-14} erg s $^{-1}$ cm $^{-2}$)	$F_{\text{H}\alpha}/F_{\text{Br}\alpha}$	A_V ^a (mag)
IRAS 10494+4424	1.46 ± 0.15	1.08 ± 0.16	5.08 ± 0.22
IRAS 10565+2448	8.42 ± 0.84	2.24 ± 0.33	4.01 ± 0.21
Mrk 273	33.1 ± 3.3	7.0 ± 1.0	2.33 ± 0.21

^aVisual extinction derived from the H α /Br α line ratio on the assumption of the case B ratio.

and 6811 Å at that of Mrk 273 ($z = 0.038$). The filters (central wavelength/FWHM in Å) we used to measure the flux of the H α line were 7146/80 for IRAS 10494+4424 and 6826/78 for Mrk 273 (on-band images). We used the 6826 filter for IRAS 10494+4424 and the 7146 filter for Mrk 273 to measure the flux of the underlying continuum (off-band images). We obtained three exposures in each of the H α and continuum filters, with individual exposure times of 900 s. We dithered the telescope between exposures to mitigate the effect of hot and bad pixels on the detector. We also obtained bias and twilight sky flat field frames for each filter.

We reduced the data using standard IRAF procedures, including bias and flat-field correction. We averaged the three dithered frames in each filter and subtracted the off-band from the on-band to obtain a pure H α + [N II] line image. The narrowband filters were photometrically calibrated with observing standard stars and comparing them with Sloan Digital Sky Survey (SDSS; Ahn et al. 2012) data. The fluxes in the filters were consistent with each other to within 5%. With the IRAF phot module, we performed circular aperture photometry (7'' in diameter) for the continuum-subtracted image and obtained the H α + [N II] line flux. We assume the [N II]/H α line ratio of 0.60 in IRAS 10494+4424 and 1.01 in Mrk 273 (Kim et al. 1998) and corrected for the [N II] emission. We summarize the H α line flux in Table 4.7.

Figure 4.15 shows the comparison of the flux of the Br α , Br β and H α lines. The high-density model well explains both the H α /Br α and Br β /Br α line ratios with dust extinction of $A_V \sim 2.5$ –5.0 mag, which is higher than the typical value of $A_V \sim 1.3$ mag suggested

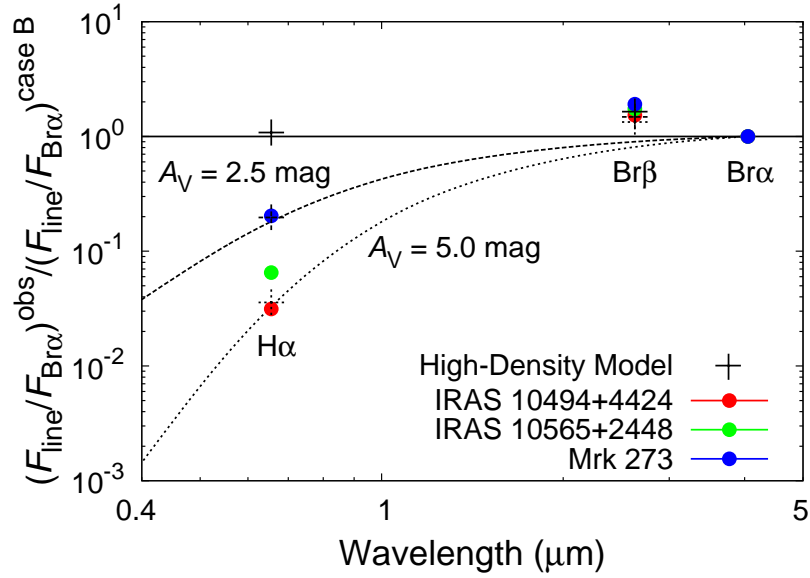


Figure 4.15. Hydrogen recombination line fluxes relative to the Br α line. The ratios are normalized to those predicted in the case B theory (10000 K, low-density limit; Osterbrock & Ferland 2006). The black lines show line ratios in the case B model with different visual extinction. The black crosses show line ratios predicted by the high-density model. The solid, dashed, and dotted crosses indicates the ratio with no dust extinction, with extinction of $A_V = 2.5$ mag, and with extinction of $A_V = 5.0$ mag, respectively.

by Kennicutt (1998) for typical spiral galaxies. The Br β /Br α line ratio is not affected so much (reduced only by ~ 10 –20%) even with the relatively high dust extinction. Thus the high Br β /Br α line ratio predicted by the high-density model is clearly seen with dust extinction of $A_V \sim 2.5$ –5.0 mag, and well explains the observed ratios. On the other hand, the H α /Br α line ratio is almost determined only by the effect of dust extinction, and the difference between the case B and the high-density model is small. The observed H α /Br α line ratio is consistent with the high-density model with dust extinction of $A_V \sim 2.5$ –5.0 mag, and is also explained by the case B model with the almost same dust extinction. We cannot distinguish the two models with the H α /Br α line ratio, but the difference can be seen clearly with the Br β /Br α line ratio.

We conclude that the high-density model is consistent with the observations of the H α line. We also conclude that the effect of dust extinction at the optical wavelength is so strong that the deviation of H I line ratios from those of case B cannot be seen in the optical wavelength.

Table 4.8. Flux Ratio of H α and H β Lines

Object Name	$F_{H\beta}/F_{H\alpha}$	A_V^{opta} (mag)	Reference ^b
IRAS 09022–3615	0.18 ± 0.009	1.90 ± 0.14	1
IRAS 10565+2448	0.06 ± 0.003	4.83 ± 0.14	2

^aVisual extinction derived from H α /H β line ratio.

^bReferences for optical line ratio: (1) Lee et al. (2011), (2) Veilleux et al. (1995).

4.4.3.2 Comparison with H β /H α Line Ratio

The H β line ($\mathcal{N} = 4 \rightarrow 2$, 4861 Å) is observable also in the optical wavelength in addition to the H α line, and so the H β /H α line ratio is one of the most intensively studied ratio among H I lines (e.g., Kim et al. 1998). We here compare the H β /H α line ratio with our Br β /Br α line ratio.

We use the H β /H α line ratio in Table 3.3 for the AGNUL sample. The ratio in two galaxies added to our sample in this chapter is summarized in Table 4.8. The H β /H α line ratio in all the targets are well below the case B value of 0.348. This indicates that the H β /H α line ratio is explained with the combination of case B and dust extinction. The inferred dust extinction on the assumption of the case B ratio (A_V^{opt} in Tables 3.3 and 4.8) is typically ~ 2.5 mag.

The comparison of the H β /H α line ratio with our Br β /Br α line ratio is shown in Figure 4.16. Figure 4.16 shows a large scatter between the two ratios. The extinction vectors in Figure 4.16 indicates that the H β /H α line ratio is largely affected by dust extinction and is almost determined by its effect. On the other hand, the Br β /Br α line ratio is almost unchanged with dust extinction of $A_V \sim 2.5$ mag.

The high Br β /Br α line ratio cannot be achieved by the case B model. On the other hand, the extinction vector from the high-density model indicates that the high Br β /Br α line ratio is well explained by the high-density model as well as the H β /H α line ratio with dust extinction of $A_V \sim 2.5$ mag.

In the high-density model, the H β /H α line ratio is predicted to be 0.217. We note that

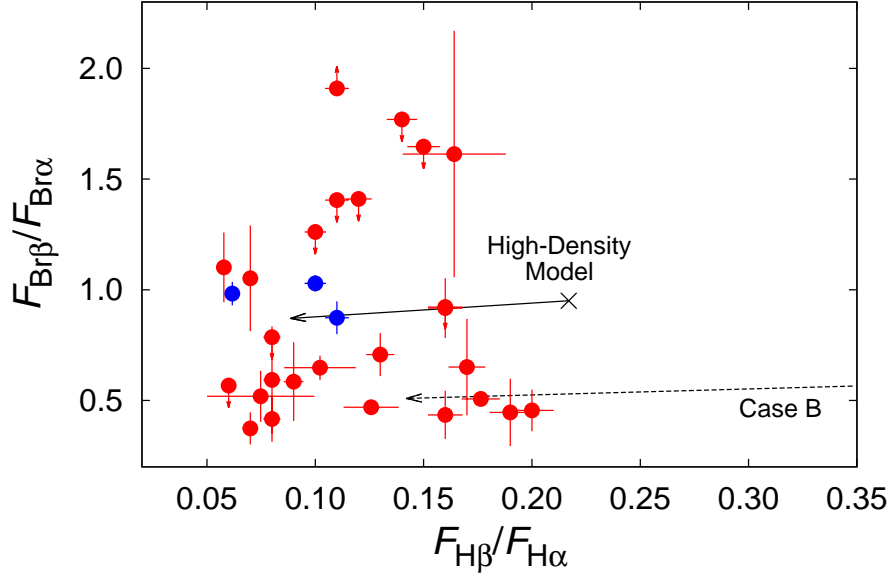


Figure 4.16. $\text{Br}\beta/\text{Br}\alpha$ line ratio versus $\text{H}\beta/\text{H}\alpha$ line ratio. The three galaxies with the high $\text{Br}\beta/\text{Br}\alpha$ line ratio is represented by the blue circles, while the others are shown by the red circles. The black cross indicates the line ratios predicted by the high-density model. The extinction vector in case of $A_V = 2.5$ mag is shown as the black arrows. The solid arrow shows extinction from the ratios of the high-density model, while the dashed arrow indicates extinction from the ratios of case B.

the deviation of the $\text{H}\beta/\text{H}\alpha$ line ratio in the high-density model is not distinguishable from the effect of dust extinction. This indicates that the deviation cannot be probed with the $\text{H}\beta/\text{H}\alpha$ line ratio even in conditions where dust extinction is very low.

From this result, we conclude that the high-density model is consistent with the observations of the $\text{H}\beta/\text{H}\alpha$ line ratio. We again propose that the deviation of H I line ratios from those of case B can be observed only in infrared wavelengths where the effect of dust extinction is small.

4.4.3.3 Comparison with $\text{Pa}\alpha/\text{Br}\gamma$ Line Ratio

In the previous sections, we conclude that the deviation of H I line ratios from those of case B cannot be seen in the optical wavelength because of dust extinction. We here compare our result with the infrared H I lines.

Among the infrared H I lines, the $\text{Br}\gamma$ line at $2.17 \mu\text{m}$ and the $\text{Pa}\alpha$ line at $1.88 \mu\text{m}$ are observable within the common aperture in the K -band ($\sim 1.9\text{--}2.5 \mu\text{m}$) observations

Table 4.9. Modeled and Observed H I Line Ratios

Lines	Case B	High-Density Model	IRAS 10494+4424	IRAS 10565+2448	Mrk 273
Br β /Br α	0.565	0.929	0.87 ± 0.07	0.98 ± 0.05	1.03 ± 0.04
H α /Br α	34.4	37.2	1.08 ± 0.16	2.24 ± 0.33	7.0 ± 1.0
H β /H α	0.348	0.217	0.110 ± 0.005	0.061 ± 0.003	0.100 ± 0.005
Pa α /Br γ	12.1	9.95	16.1 ± 1.5^a	...	10.8 ± 1.0^b

^aTaken from Murphy et al. (2001).

^bTaken from Veilleux et al. (1999b).

from the ground in objects with redshift of ~ 0.01 – 0.15 . These lines are relatively strong among the H I lines and have been observed in various studies to measure dust extinction (e.g., Goldader et al. 1995; Veilleux et al. 1999b). We investigate the high-density model prediction on this line ratio.

We summarize the predicted line ratios of the high-density model in Table 4.9. The predicted Pa α /Br γ line ratio is 9.95, deviating from the case B value of 12.1. In this deviation, the Pa α line at the shorter wavelength is weakened relative to the Br γ line at the longer wavelength. This is the same trend as the effect of dust extinction. The Pa α /Br γ line ratio of 9.95 corresponds to dust extinction of $A_V = 7.31$ mag on the assumption of the case B ratio. This means that we cannot distinguish the deviation of the Pa α /Br γ line ratio from that of case B with the effect of dust extinction. Thus our model is consistent with the fact that no anomaly has been reported in the previous observations of the Pa α /Br γ line ratio.

Among our targets with the anomalous Br β /Br α line ratio, the Pa α /Br γ line ratio was observed in IRAS 10494+4424 by Murphy et al. (2001) and in Mrk 273 by Veilleux et al. (1999b). We cannot find observations of the Pa α /Br γ line ratio in IRAS 10565+2448. The Pa α /Br γ line ratio in Mrk 273 is 10.8 ± 1.0 and is consistent with our prediction. The Pa α /Br γ line ratio in IRAS 10494+4424 was reported to be 16.1 ± 1.5 . This ratio indicates that the Pa α line is enhanced relative to the Br γ line compared to the case B ratio. This is opposite to the effect of dust extinction and also to the deviation of our model from the case B ratio. Thus the ratio is explained neither by our model nor by the case B ratio

with dust extinction. Murphy et al. (2001) regarded this anomaly as not significant. They claimed that the observation of the Pa α and Br γ lines in IRAS 10494+4424 was performed with different apertures, and this made the observed Pa α /Br γ line ratio uncertain by as large as 50%. Thus we also treat the deviation as not significant here.

In summary, we conclude that our model does not contradict to the previous observations of H I line ratios.

4.4.4 Implications with Our Model

From the high density condition of ionized gas indicated by our model, we propose two implications on the radio recombination lines and the nature of starburst activities in ULIRGs.

4.4.4.1 Radio Recombination Lines

We here discuss the effect of the high density condition on the radio recombination lines. Our model requires gas density of $n = 10^8 \text{ cm}^{-3}$. In high density conditions, collisional process becomes important for high \mathcal{N} states. As shown in Figure 4.11, the hydrogen states with low principal quantum numbers ($\mathcal{N} \leq 15$) are not dominated by collisions even with this density of $n = 10^8 \text{ cm}^{-3}$. On the other hand, the collisional process starts to contribute significantly to the states with $\mathcal{N} \geq 20$. This means that hydrogen radio recombination lines emitted with transitions in high \mathcal{N} states are affected by the high density our model predicts.

Peters et al. (2012) show that at the density of $n = 10^8 \text{ cm}^{-3}$, $b_{\mathcal{N}}$ becomes ~ 1 at $\mathcal{N} > 30$ levels (Figure 4.10). On the other hand, in the condition with $n = 10^6 \text{ cm}^{-3}$, where the anomaly of the Br β /Br α line ratio is not found with the Cloudy simulation, only the states with $\mathcal{N} > 50$ become thermalized. This indicates that observations of radio recombination lines with low \mathcal{N} transitions ($\mathcal{N} < 50$) is required to probe our model prediction. However, previous observations of the radio recombination lines was mainly focused on the high \mathcal{N} transitions because of the difficulty of the observation at high frequencies where $\mathcal{N} < 50$ transitions fall in.

Those radio recombination lines at $\mathcal{N} < 50$ levels are now observable within the fre-

quency range of ALMA. We predict that the radio recombination lines with $\mathcal{N} < 50$ transitions are thermalized in the galaxies with the line ratio anomaly.

4.4.4.2 High-Density Starburst

If the conditions indicated by the Cloudy simulation are realized, the ULIRGs with the anomaly harbor the high-density starburst with $n \sim 10^8 \text{ cm}^{-3}$. Klessen et al. (2007) suggested that gas with a high temperature and a high density would yield a top-heavy initial-mass-function. If an extreme case of the top-heavy IMF is realized in the ultra-high-density starburst indicated by our results, the OB star population is much more enhanced than normal conditions. We propose this scenario as an explanation of the high efficiency of starburst in ULIRGs.

4.5 Summary

We conducted systematic observations of the H I Br α and Br β lines with the *AKARI* IRC in 52 nearby ($z < 0.3$) ULIRGs. We detected Br α and Br β lines in 31 ULIRGs. Among the 31 ULIRGs, three galaxies, IRAS 10494+4424, IRAS 10565+2448, and Mrk 273, show a Br β /Br α line ratio (0.873 ± 0.074 , 0.983 ± 0.053 , and 1.029 ± 0.037 , respectively) significantly higher than that of case B (0.565). If dust extinction affects the flux of the lines, the Br β /Br α line ratio becomes lower than 0.565 because the Br β line has a shorter wavelength and so is more attenuated than the Br α line. Thus we cannot explain the high Br β /Br α line ratio in the three galaxies with the combination of the case B theory and dust extinction.

We investigate the cause of the anomaly and obtain the following results:

1. We investigate the possibility of a contamination of the Br β line by other lines. We identify one candidate, the H₂ (1,0) O(2) line, whose wavelength (2.627 μm) is close to that of the Br β line (2.626 μm). We estimate the flux of the H₂ (1,0) O(2) line from that of another molecular hydrogen line, H₂ (1,0) O(3) at 2.802 μm , on the assumption that the line ratio corresponds to that of the 2000 K shock model (Black & van Dishoeck 1987). The expected flux of the H₂ (1,0) O(2) line is typically $\sim 5\%$ of that of the observed Br β line. The Br β /Br α line ratio, therefore, is still higher

than that of case B beyond the 3σ level even after we subtract the flux of the H_2 (1,0) O(2) line from that of the $\text{Br}\beta$ line. Thus we conclude that the contamination does not give full explanation of the high $\text{Br}\beta/\text{Br}\alpha$ line ratio.

2. In the case that the Brackett lines are optically thin, we cannot explain the high $\text{Br}\beta/\text{Br}\alpha$ line ratio with possible excitation mechanisms: recombination, collisional excitation, and resonant excitation.
3. On the other hand, we find that we can explain the deviation of the $\text{Br}\beta/\text{Br}\alpha$ line ratio from that of case B if the $\text{Br}\alpha$ line becomes optically thick while the $\text{Br}\beta$ line is still optically thin.
4. We assume that the high $\text{Br}\beta/\text{Br}\alpha$ line ratio is produced in an ensemble of H II regions with uniform density gas and each H II region is ionized by a single star. We simulate such H II regions with the Cloudy code and find that the high $\text{Br}\beta/\text{Br}\alpha$ line ratio is explained when the $\text{Br}\alpha$ line becomes optically thick. To achieve a column density large enough to make the $\text{Br}\alpha$ line optically thick within a single H II region, the gas density as high as $n \sim 10^8 \text{ cm}^{-3}$ is required. From this result, we propose an ensemble of H II regions, in each of which the $\text{Br}\alpha$ line is optically thick, can explain the high $\text{Br}\beta/\text{Br}\alpha$ line ratio.
5. We investigate line ratios of optical H I lines in the galaxies which show the high $\text{Br}\beta/\text{Br}\alpha$ line ratio in our sample. We find that the flux of the optical lines is highly extinguished by dust extinction, and it is difficult to tell if the line ratio contradicts to that of the case B theory. We conclude that the deviation of H I line ratios from those of case B is clearly seen only in the infrared H I lines because optical lines are largely affected by dust extinction.
6. We investigate consistency of the high-density model and other infrared H I line observations. The H I line ratios other than the $\text{Br}\beta/\text{Br}\alpha$ line ratio are compared with those predicted by the high-density model in the three galaxies with the high $\text{Br}\beta/\text{Br}\alpha$ line ratio. We conclude that our model is consistent with previous observations of the $\text{Pa}\alpha/\text{Br}\gamma$ line ratio.

7. Our model requires high density H II regions of $n = 10^8 \text{ cm}^{-3}$. This affects high \mathcal{N} transitions of H I lines which fall in radio frequencies. We predict that the radio recombination lines with $\mathcal{N} < 50$ transitions are thermalized in the galaxies with the high $\text{Br}\beta/\text{Br}\alpha$ line ratio.
8. Klessen et al. (2007) suggested that gas with a high temperature and a high density would yield a top-heavy IMF. If an extreme case of the top-heavy IMF is realized in the high-density starburst indicated by our model, the OB star population is much more enhanced than normal conditions. We propose this scenario as an explanation of the high efficiency of starburst in ULIRGs.

Chapter 5

Conclusion

We take two approaches to investigate the energy sources and the nature of starburst activities in ULIRGs.

1. In order to estimate the strength of starburst unbiased by dust extinction, we conducted systematic observations of the hydrogen Br α line with the *AKARI* IRC 2.5–5.0 μm spectroscopy in 50 nearby ($z < 0.3$) ULIRGs. We detected the Br α line in 33 ULIRGs. Comparing the Br α line with the 3.3 μm PAH emission and the total infrared luminosity, we investigate the fractional contribution of starburst to the total infrared luminosity in ULIRGs. The main results are as follows:
 - (a) We compare the Br α line luminosity ($L_{\text{Br}\alpha}$) with the 3.3 μm PAH emission luminosity ($L_{3.3}$) and find a good correlation between them. This indicates that $L_{3.3}$ and $L_{\text{Br}\alpha}$ trace the same excitation sources, i.e., star formation. To investigate star formation in fainter objects, we derive $L_{\text{Br}\alpha}/L_{3.3} = 0.177 \pm 0.003$.
 - (b) On the other hand, the total infrared luminosity (L_{IR}) and $L_{\text{Br}\alpha}$ show no clear correlation with each other. We also confirm that $L_{3.3}$ and L_{IR} show no clear correlation with each other in a larger sample. The mean $L_{\text{Br}\alpha}/L_{\text{IR}}$ (and $L_{3.3}/L_{\text{IR}}$) ratio is significantly lower in galaxies optically classified as LINERs and Seyferts than in H II galaxies. We propose that the difference reflects the contribution of starburst to the total infrared luminosity in ULIRGs. We estimate that the contribution of starburst to the total infrared luminosity in LINERs and Seyferts

is $(67 \pm 9)\%$, and AGNs contribute to the remaining $(33 \pm 9)\%$.

(c) We find that the number of ionizing photons derived from the Br α line ($Q_{\text{Br}\alpha}$) is significantly smaller than that expected from the SFR required to explain the total infrared luminosity (Q_{IR}). We attribute this apparently low ratio to the underestimation of the number of ionizing photons with the Br α line. We propose that dust within H II regions absorbs a significant fraction ($\sim 45\%$) of ionizing photons.

2. In order to investigate the validity of the standard theory of H I line ratios, case B, in ULIRGs, we conducted systematic observations of the H I Br β line in addition to the Br α line with the *AKARI* IRC in 52 nearby ($z < 0.3$) ULIRGs. We detected Br α and Br β lines in 31 ULIRGs. Among the 31 ULIRGs, three galaxies, IRAS 10494+4424, IRAS 10565+2448, and Mrk 273, show a Br β /Br α line ratio (0.873 ± 0.074 , 0.983 ± 0.053 , and 1.029 ± 0.037 , respectively) significantly higher than that of case B (0.565). We cannot explain the high Br β /Br α line ratio in the three galaxies with the combination of the case B theory and dust extinction. We investigate the cause of the anomaly and obtain the following results:

(a) In the case that the Brackett lines are optically thin, we cannot explain the high Br β /Br α line ratio with possible excitation mechanisms: recombination, collisional excitation, and resonant excitation.

(b) On the other hand, we find that we can explain the deviation of the Br β /Br α line ratio from that of case B if the Br α line becomes optically thick while the Br β line is still optically thin.

(c) To check the result (b) quantitatively, we assume that the high Br β /Br α line ratio is produced in an ensemble of H II regions with uniform density gas and each H II region is ionized by a single star. We simulate such H II regions with the Cloudy code and find that the high Br β /Br α line ratio is explained when the Br α line becomes optically thick. To achieve the column density large enough to make the Br α line optically thick within a single H II region, the gas density as high as $n \sim 10^8 \text{ cm}^{-3}$ is required. From this result, we propose an ensemble

of H II regions, in each of which the Br α line is optically thick, can explain the high Br β /Br α line ratio.

- (d) We investigate line ratios of optical H I lines in the galaxies which show the high Br β /Br α line ratio in our sample. We find that the flux of the optical lines is highly extinguished by dust extinction, and it is difficult to tell if the line ratio contradicts to that of the case B theory. We conclude that the deviation of H I line ratios from those of case B is clearly seen only in the infrared H I lines because optical lines are largely affected by dust extinction.
- (e) We investigate consistency of the high-density model and other infrared H I line observations and show that our model is consistent with previous observations of the Pa α /Br γ line ratio.
- (f) Klessen et al. (2007) suggested that gas with a high temperature and a high density would yield a top-heavy IMF. If an extreme case of the top-heavy IMF is realized in the high-density starburst indicated by our model, the OB star population is much more enhanced than normal conditions. We propose this scenario as an explanation of the high efficiency of starburst in ULIRGs.

Appendix A

Near-Infrared Spectra of Ultraluminous Infrared Galaxies

We here present all the 2.5–5.0 μm near-infrared spectra of ULIRGs, which are discussed in Chapter 4.

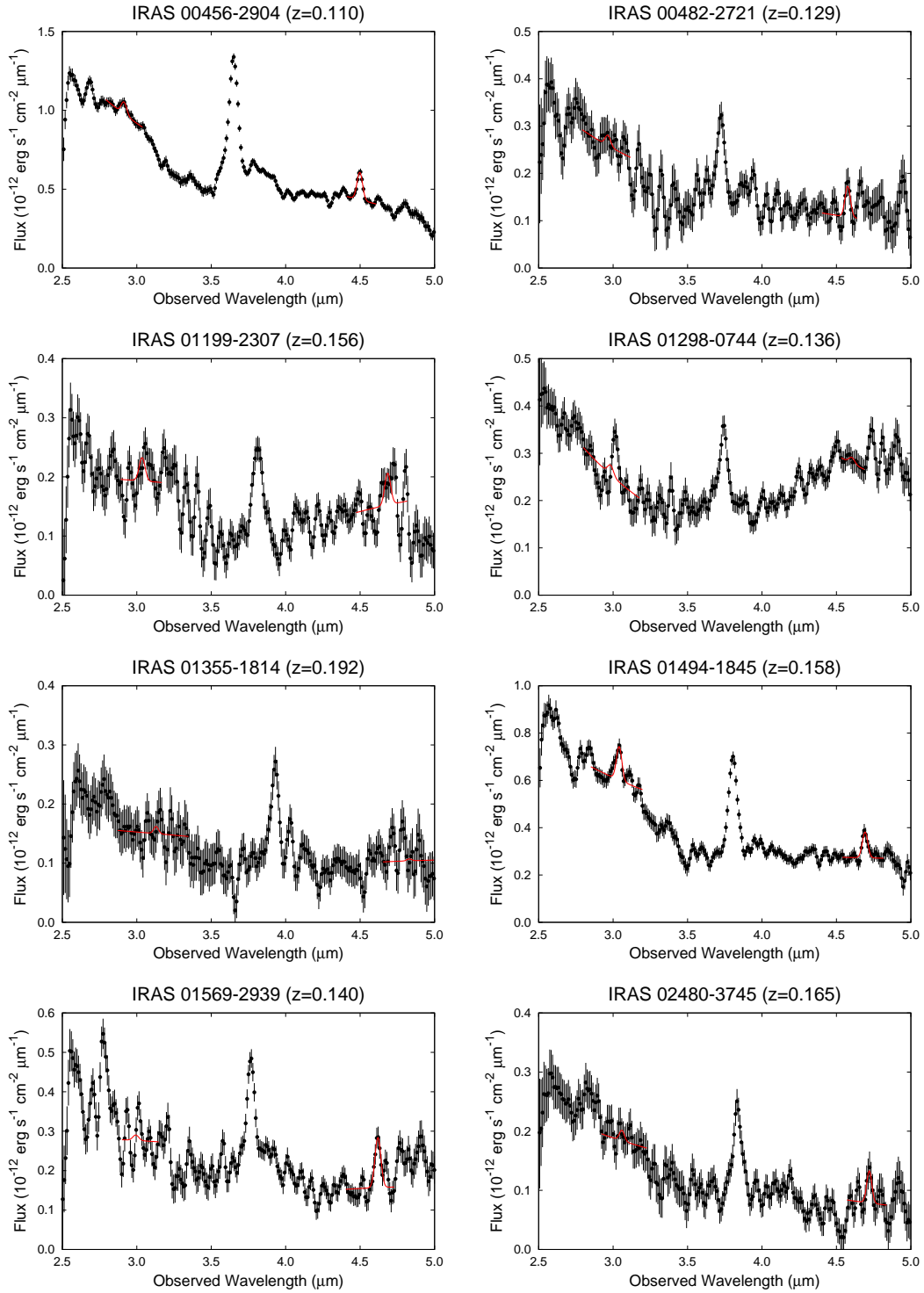


Figure A.1. *AKARI* 2.5–5.0 μm near-infrared spectra of ULIRGs. The best-fit Gaussian profile for the Br α and Br β lines are presented with red lines.

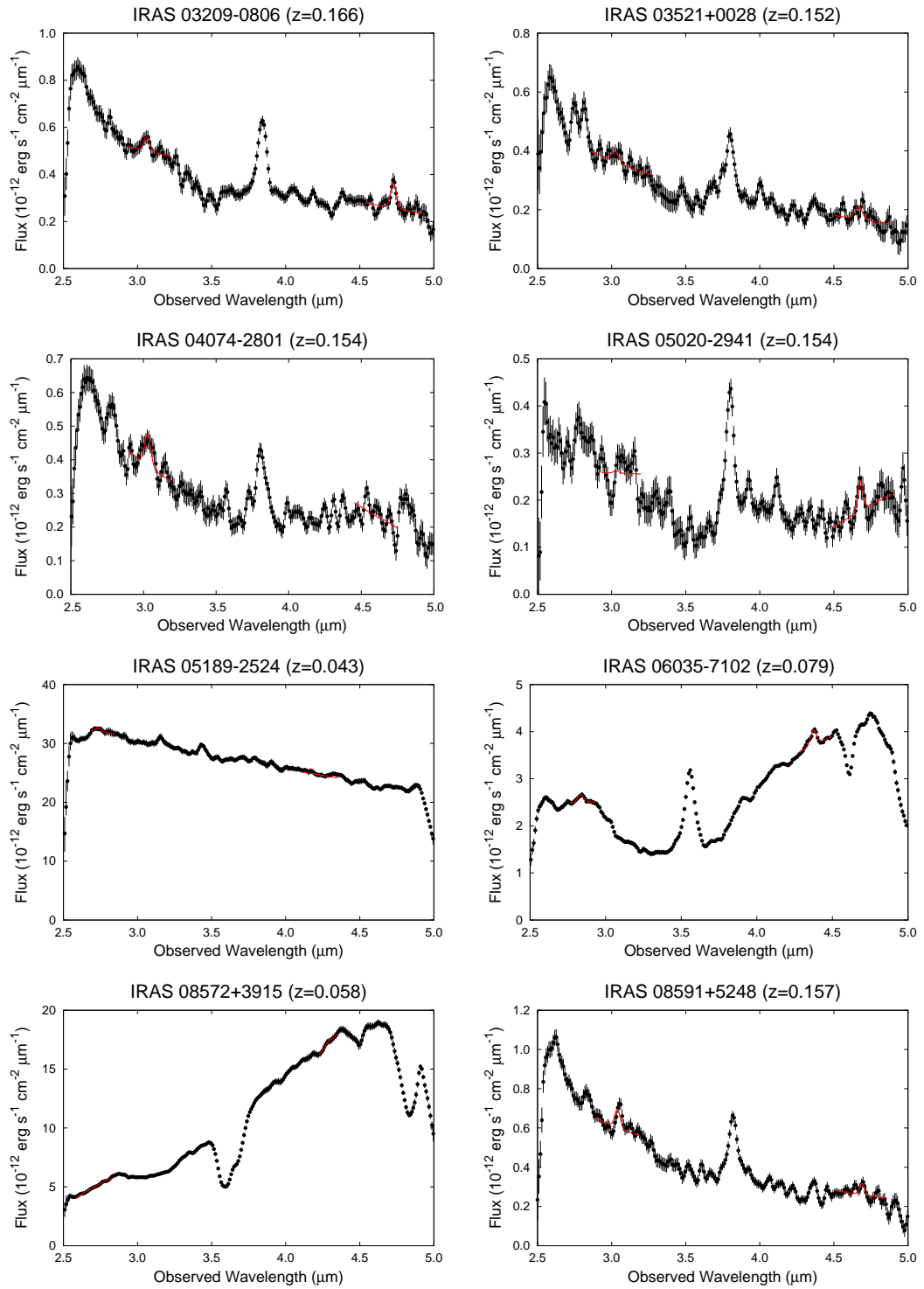


Figure A.1. *Continued*

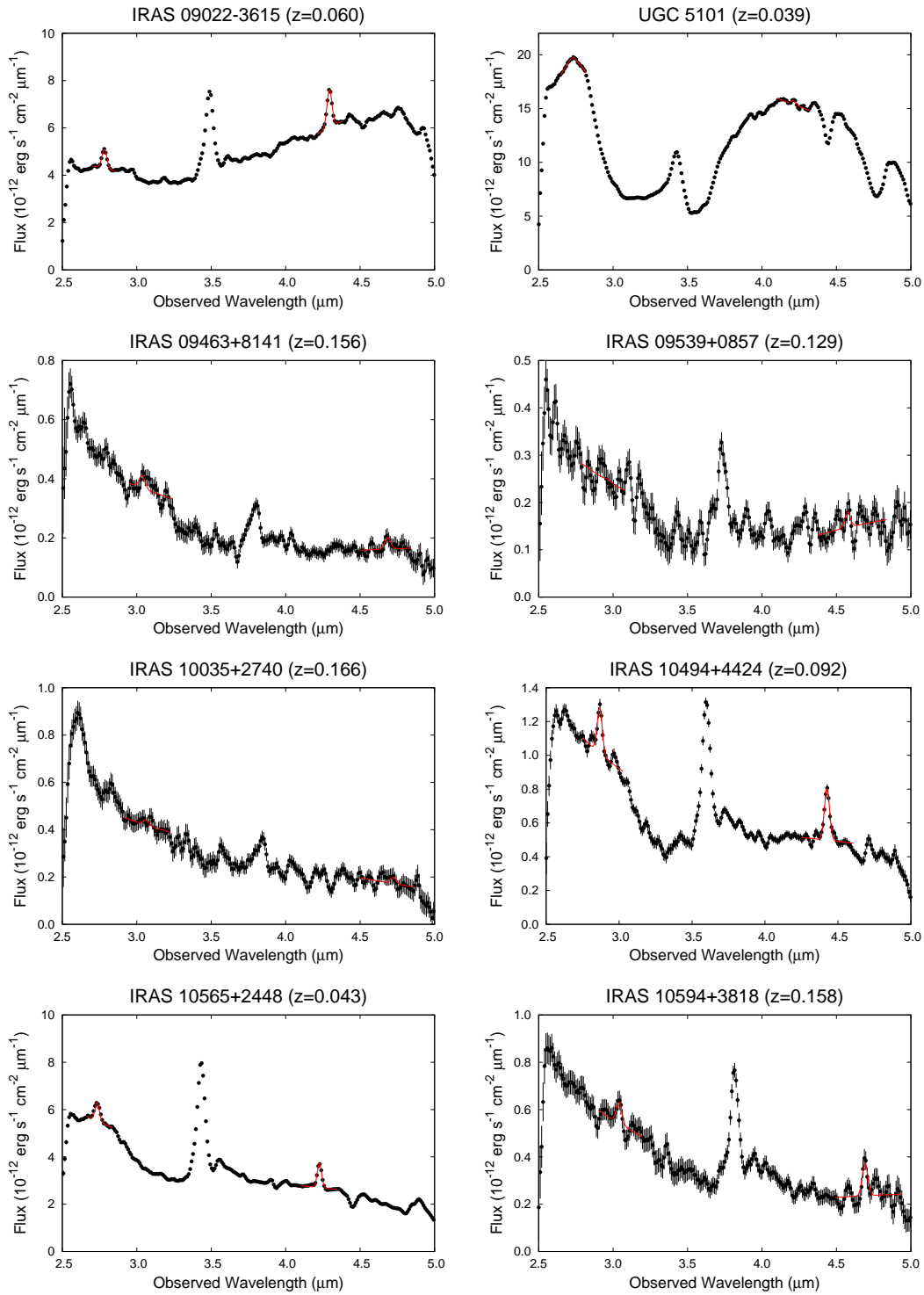


Figure A.1. *Continued*

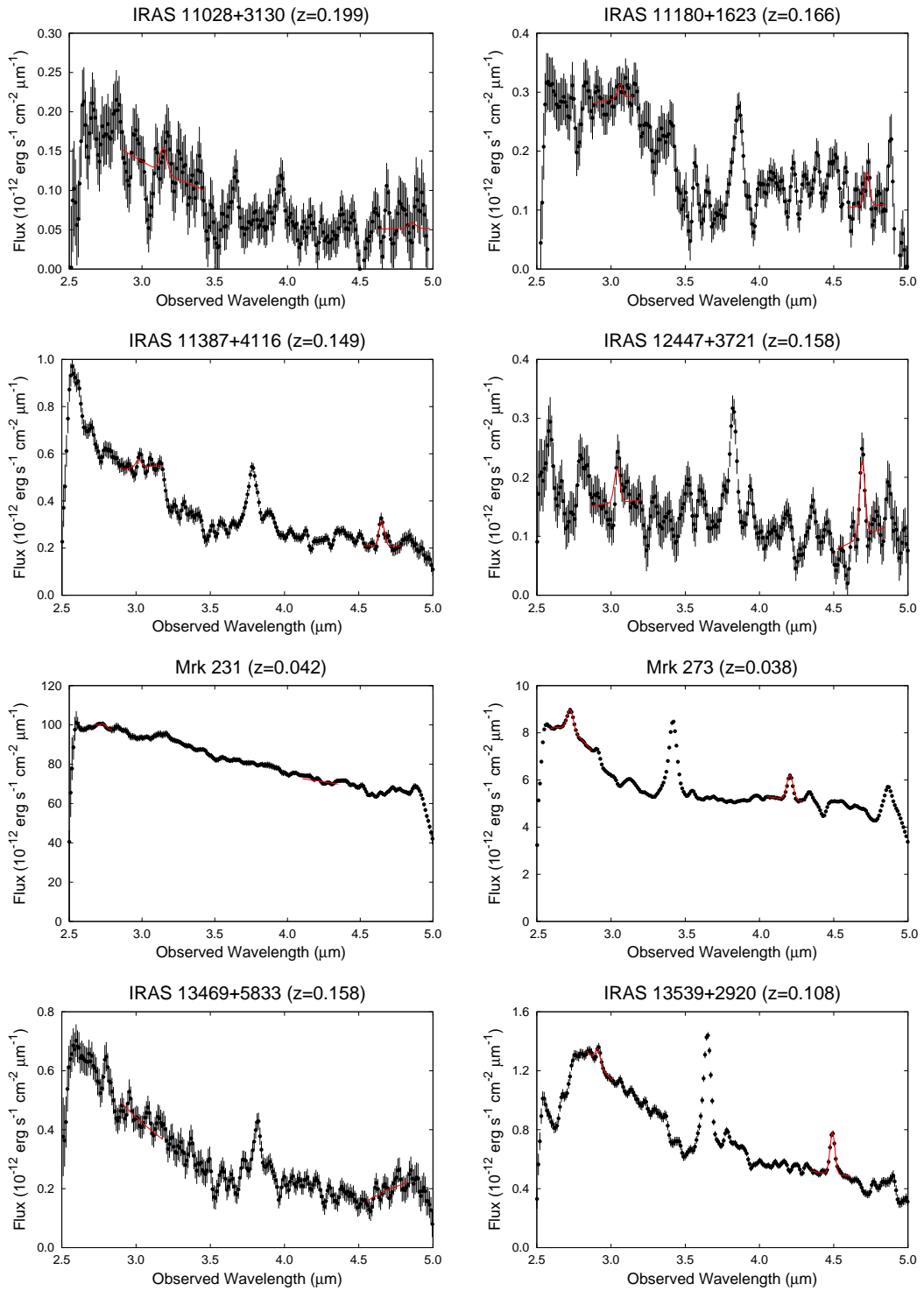


Figure A.1. *Continued*

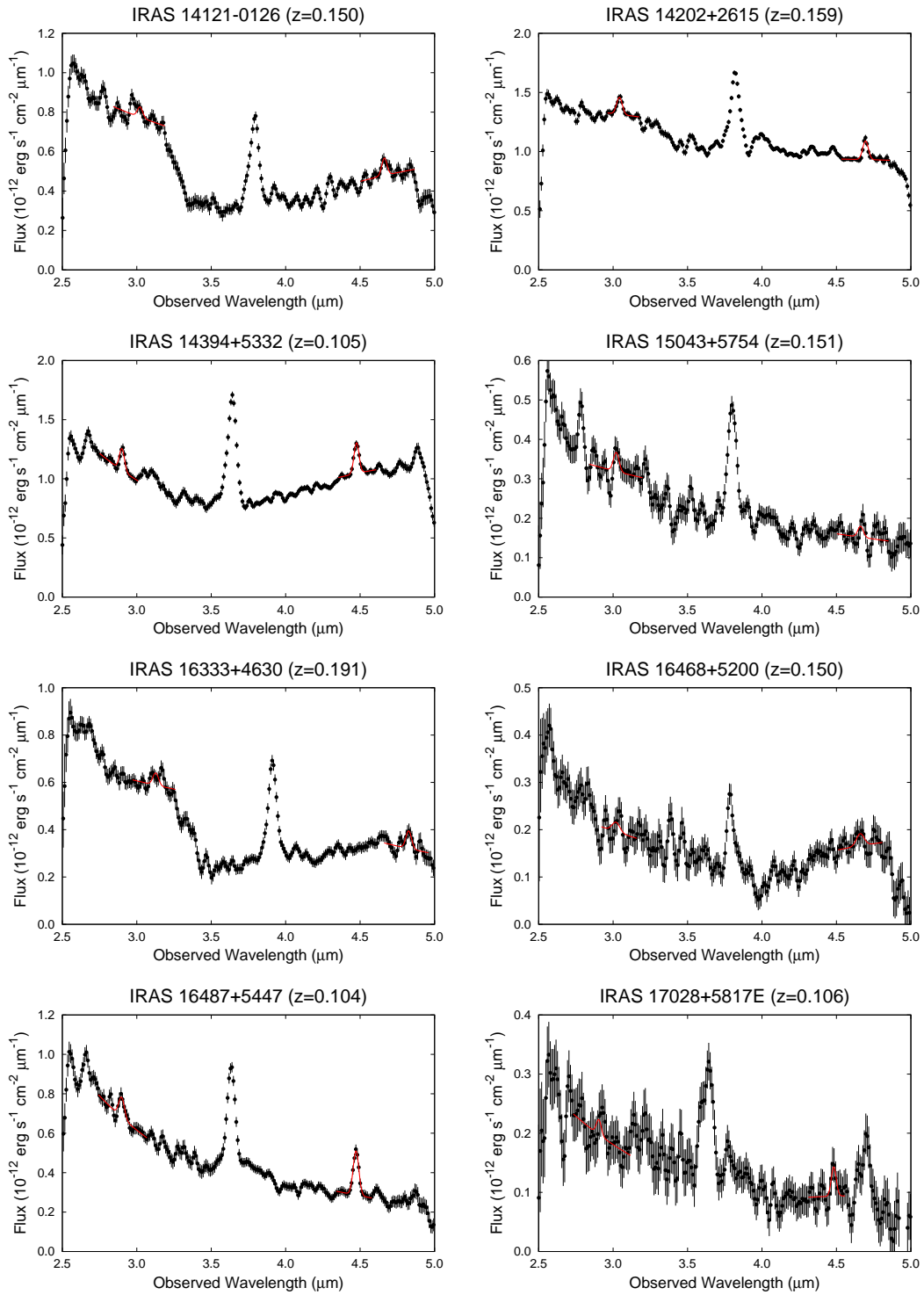


Figure A.1. *Continued*

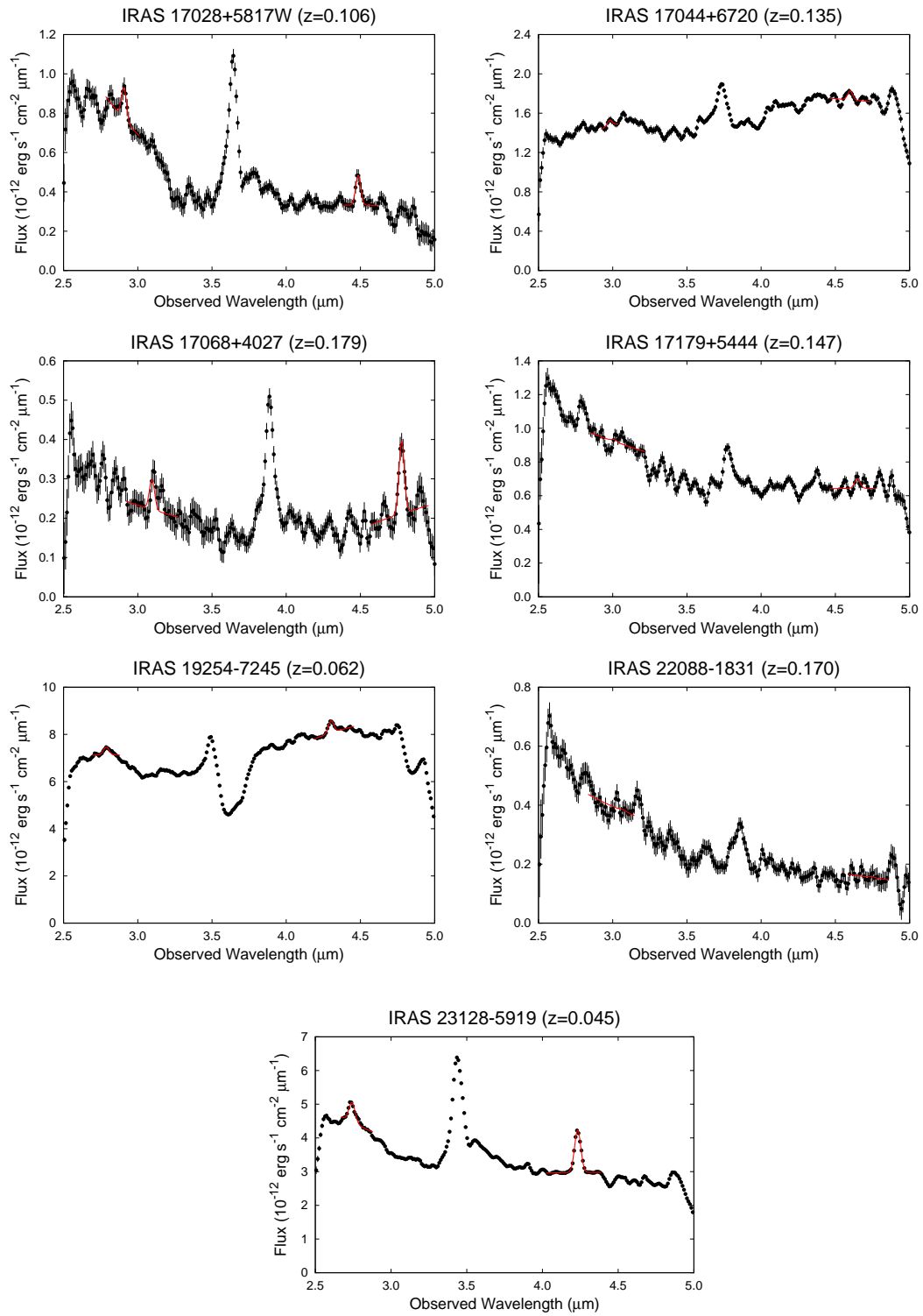


Figure A.1. *Continued*

Appendix B

Br β /Br α Line Ratio in Galactic H II Regions

Our result of the high Br β /Br α line ratio indicates that the condition of H II regions in the ULIRGs with the anomaly is different from that of Galactic H II regions, where the case B theory is expected to well explain the line ratio. To investigate the difference, we discuss the applicability of the case B line ratio of the Br α and Br β lines in Galactic H II regions.

Because of the difficulty of observing the wavelength range of the Br α and Br β lines due to the atmospheric interference, previous observations are limited to those conducted in space, namely, observations with the *ISO* and *AKARI* satellites. We investigate observations of Galactic H II regions with the two satellites.

B.1 *ISO* Observation

Lutz et al. (1996) obtained a 2.4–45 μm spectrum of the Galactic center with Short Wavelength Spectrometer on board *ISO*. The $14'' \times 21''$ aperture was centered at Sgr A* to cover H II regions in the Galactic center region. They detected H I lines, including the Br α and Br β lines, between 2.5–9.0 μm wavelengths. The Br β /Br α line ratio in the Galactic center was reported to be ~ 0.25 , which was consistent with the case B condition with dust extinction (Lutz 1999). Lutz (1999) also discussed the applicability of the case B

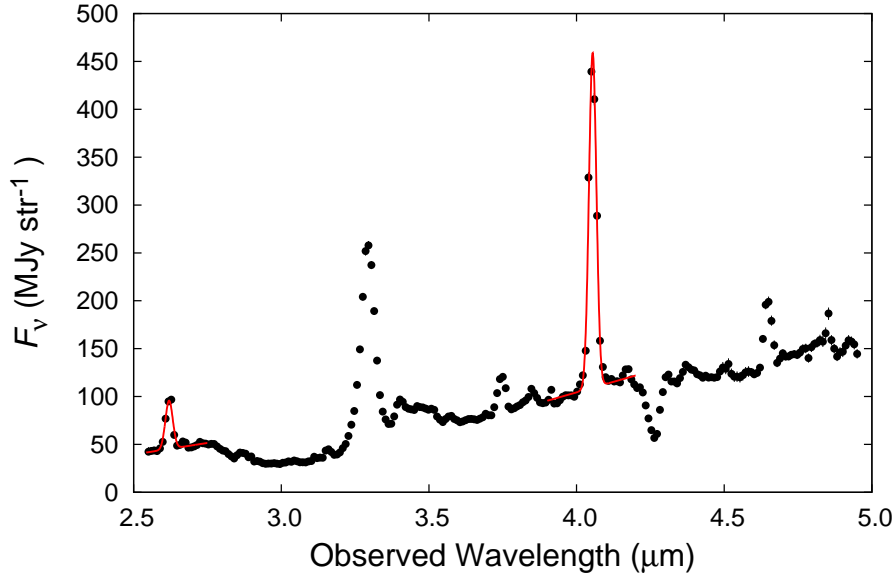


Figure B.1. Typical example of the cataloged spectra of Galactic H II regions provided by Mori et al. (2014). The spectrum is taken from the position “-04” of W31a (ID: 5200165.1) by the use of the “Nh” slit. The best-fit Gaussian profile for the Br α and Br β lines are presented with red lines.

condition in the Galactic center with the use of the Br α line, the Pf α line ($\mathcal{N} = 6 \rightarrow 5$; 7.46 μm), and a blend of the Hu β line ($\mathcal{N} = 8 \rightarrow 6$; 7.50 μm) with the $\mathcal{N} = 11 \rightarrow 7$ transition (7.51 μm). They concluded that the flux ratios of these lines were consistent with the case B line ratios, and the population of the respective upper levels followed the case B. Thus the *ISO* result indicates that the case B line ratio is applicable to H II regions in the Galactic center region.

B.2 *AKARI* Observation

With the *AKARI* near-infrared spectroscopy, Mori et al. (2014) conducted a systematic observation of 36 Galactic H II regions and provided a catalog of 2.5–5.0 μm spectra of the Galactic H II regions*. A typical example of the cataloged spectra is shown in Figure B.1.

We estimate the Br α and Br β line fluxes in those Galactic H II regions using the 232 cataloged spectra. The Br α and Br β lines are separately fitted with a Gaussian profile and a linear continuum in each spectrum. According to Mori et al. (2014), we fix the FWHM of

*The catalog is publicly available at URL: http://www.ir.isas.jaxa.jp/AKARI/Archive/Catalogues/IRC_GALHII_spec/

the Gaussian profile to $0.031 \mu\text{m}$ for spectra taken with the “Ns” slit and $0.025 \mu\text{m}$ for those taken with “Nh” slit to match the spectral resolution of the slits. The central wavelength of the lines are also fixed to $4.05 \mu\text{m}$ for the $\text{Br}\alpha$ line and $2.63 \mu\text{m}$ for the $\text{Br}\beta$ line. The range of wavelength used for the fitting is $\pm 0.15 \mu\text{m}$ around the central wavelength of each line. The line flux is then estimated by integrating the best-fit Gaussian profile. A typical example of the Gaussian fitting is shown in Figure B.1.

We show the obtained flux of the $\text{Br}\alpha$ and $\text{Br}\beta$ lines in the Galactic H II regions in Figure B.2. The result shows that almost all the $\text{Br}\beta/\text{Br}\alpha$ line ratio is lower than that in the case B condition except a few spectra. This means that the $\text{Br}\beta/\text{Br}\alpha$ line ratio in the Galactic H II regions is explained by the case B condition with dust extinction of typically $A_V \sim 10$ mag.

Combining the results of the observations of *ISO* and *AKARI*, we conclude that the case B condition is valid in Galactic H II regions. Thus our result of the anomaly of the $\text{Br}\beta/\text{Br}\alpha$ line ratio in ULIRGs indicates that the condition of H II regions in the ULIRGs with the anomaly is different from the case B conditions.

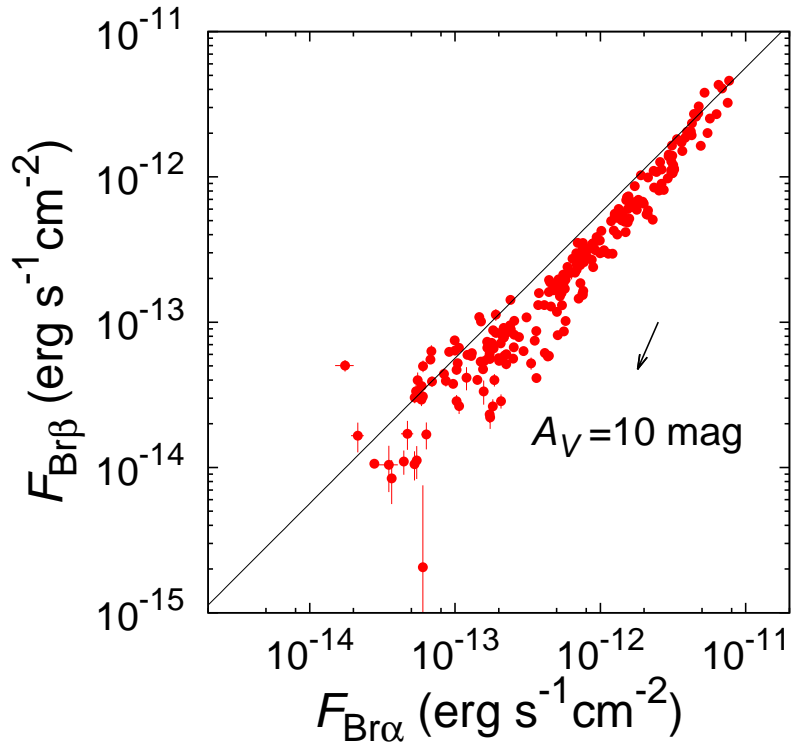


Figure B.2. The flux of the Br α and Br β lines in Galactic H II regions estimated by the use of the spectral catalog of Mori et al. (2014). The solid line shows the theoretical line ratio in the case B condition: $F_{\text{Br}\beta}/F_{\text{Br}\alpha} = 0.565$. The extinction vector in case of $A_V = 10$ mag is shown as the black arrow.

Acknowledgements

I would like to express my deepest gratitude to my supervisor Prof. Takao Nakagawa for guiding and encouraging me over the 6 years of my graduate course. I am also grateful to Dr. Naoki Isobe and Dr. Mai Shirahata who have been supporting me and giving a lot of advice since the beginning of my study at graduate school.

This work is based on observations made with *AKARI*, a JAXA project, with the participation of ESA. I am grateful to all the members of the *AKARI* project for making this study possible. I also would like to extend my sincere appreciation to all the members of LIRA at ISAS/JAXA, where I spent my 6 years in graduate school. I particularly thank Dr. Fumihiko Usui and Mr. Shunsuke Baba for having discussions on the reduction of the *AKARI* spectra.

I am gratefully acknowledge Prof. Matthew Malkan for giving me the opportunity to stay in UCLA and having fruitful discussions on the anomaly of hydrogen line ratio. I am also thankful to Ms. Vanshree Bhalotia for the reduction of the Nickel data.

I would like to express my thanks and appreciations to Prof. Satoshi Yamamoto, my supervisor of the Leading Graduates Schools Program “Advanced Leading Graduate Course for Photon Science (ALPS),” for supporting me throughout my time in graduate school. I also would like to acknowledge generous support that I have received from the ALPS program, which enabled the stay at UCLA.

Last but not the least, I thank my family for supporting me throughout all my studies at university.

References

- Abazajian, K., Adelman-McCarthy, J. K., Agüeros, M. A., et al. 2003, *AJ*, 126, 2081
- . 2005, *AJ*, 129, 1755
- Adelman-McCarthy, J. K., Agüeros, M. A., Allam, S. S., et al. 2006, *ApJS*, 162, 38
- . 2008, *ApJS*, 175, 297
- Ahn, C. P., Alexandroff, R., Allende Prieto, C., et al. 2012, *ApJS*, 203, 21
- Alonso-Herrero, A., Pereira-Santaella, M., Rieke, G. H., & Rigopoulou, D. 2012, *ApJ*, 744, 2
- Anantharamaiah, K. R., Zhao, J.-H., Goss, W. M., & Viallefond, F. 1993, *ApJ*, 419, 585
- Armus, L., Heckman, T. M., & Miley, G. K. 1989, *ApJ*, 347, 727
- Armus, L., Charmandaris, V., Bernard-Salas, J., et al. 2007, *ApJ*, 656, 148
- Arthur, S. J., Medina, S.-N. X., & Henney, W. J. 2016, *MNRAS*, 463, 2864
- Baldwin, J. A., Phillips, M. M., & Terlevich, R. 1981, *PASP*, 93, 5
- Black, J. H., & van Dishoeck, E. F. 1987, *ApJ*, 322, 412
- Buchanan, C. L., McGregor, P. J., Bicknell, G. V., & Dopita, M. A. 2006, *AJ*, 132, 27
- Carilli, C. L., Wrobel, J. M., & Ulvestad, J. S. 1998, *AJ*, 115, 928
- Churchwell, E. 2002, *ARA&A*, 40, 27
- Colless, M., Dalton, G., Maddox, S., et al. 2001, *MNRAS*, 328, 1039

- Colless, M., Peterson, B. A., Jackson, C., et al. 2003, arXiv:astro-ph/0306581
- Cox, A. N. 2000, *Allen's astrophysical quantities* (4th ed.; New York: AIP Press; Springer)
- Dale, D. A., & Helou, G. 2002, *ApJ*, 576, 159
- Darling, J., & Giovanelli, R. 2006, *AJ*, 132, 2596
- Dartois, E., & Muñoz-Caro, G. M. 2007, *A&A*, 476, 1235
- de Pree, C. G., Rodriguez, L. F., & Goss, W. M. 1995, *Rev. Mexicana Astron. Astrofis.*, 31, 39
- Downes, D., Solomon, P. M., & Radford, S. J. E. 1993, *ApJ*, 414, L13
- Draine, B. T. 2003, *ARA&A*, 41, 241
- Duc, P.-A., Mirabel, I. F., & Maza, J. 1997, *A&AS*, 124, 533
- Ferland, G. J., Korista, K. T., Verner, D. A., et al. 1998, *PASP*, 110, 761
- Fisher, K. B., Huchra, J. P., Strauss, M. A., et al. 1995, *ApJS*, 100, 69
- Fritz, T. K., Gillessen, S., Dodds-Eden, K., et al. 2011, *ApJ*, 737, 73
- Genzel, R., Lutz, D., Sturm, E., et al. 1998, *ApJ*, 498, 579
- Glass, I. S. 1999, *Handbook of Infrared Astronomy*, ed. R. Ellis, J. Huchra, S. Kahn, G. Rieke, & P. B. Stetson (Cambridge, New York: Cambridge University Press)
- Goldader, J. D., Joseph, R. D., Doyon, R., & Sanders, D. B. 1995, *ApJ*, 444, 97
- . 1997, *ApJ*, 474, 104
- Hirashita, H., Buat, V., & Inoue, A. K. 2003, *A&A*, 410, 83
- Ho, L. C. 2008, *ARA&A*, 46, 475
- Hou, L. G., Wu, X.-B., & Han, J. L. 2009, *ApJ*, 704, 789
- Huchra, J., Davis, M., Latham, D., & Tonry, J. 1983, *ApJS*, 52, 89
- Hummer, D. G., & Storey, P. J. 1987, *MNRAS*, 224, 801

- Hwang, H. S., Serjeant, S., Lee, M. G., Lee, K. H., & White, G. J. 2007, MNRAS, 375, 115
- Imanishi, M. 2009, ApJ, 694, 751
- Imanishi, M., Dudley, C. C., Maiolino, R., et al. 2007, ApJS, 171, 72
- Imanishi, M., Maiolino, R., & Nakagawa, T. 2010a, ApJ, 709, 801
- Imanishi, M., Nakagawa, T., Ohyama, Y., et al. 2008, PASJ, 60, 489
- Imanishi, M., Nakagawa, T., Shirahata, M., Ohyama, Y., & Onaka, T. 2010b, ApJ, 721, 1233
- Johnson, L. C. 1972, ApJ, 174, 227
- Jones, D. H., Saunders, W., Colless, M., et al. 2004, MNRAS, 355, 747
- Jones, D. H., Read, M. A., Saunders, W., et al. 2009, MNRAS, 399, 683
- Kawada, M., Baba, H., Barthel, P. D., et al. 2007, PASJ, 59, 389
- Kennicutt, R. C., & Evans, N. J. 2012, ARA&A, 50, 531
- Kennicutt, Jr., R. C. 1998, ARA&A, 36, 189
- Kessler, M. F., Steinz, J. A., Anderegg, M. E., et al. 1996, A&A, 315, L27
- Kim, D.-C., & Sanders, D. B. 1998, ApJS, 119, 41
- Kim, D.-C., Veilleux, S., & Sanders, D. B. 1998, ApJ, 508, 627
- Kim, J. H., Im, M., Lee, H. M., et al. 2012, ApJ, 760, 120
- Klessen, R. S., Spaans, M., & Jappsen, A.-K. 2007, MNRAS, 374, L29
- Komatsu, E., Smith, K. M., Dunkley, J., et al. 2011, ApJS, 192, 18
- Kurtz, S. E. 2000, RevMexAA Ser. Conf., 9, 169
- Lauberts, A., & Valentijn, E. A. 1989, The Surface Photometry Catalogue of the ESO-Uppsala Galaxies (Garching, Germany: European Southern Observatory)

- Lee, J. C., Hwang, H. S., Lee, M. G., Kim, M., & Kim, S. C. 2011, MNRAS, 414, 702
- Lee, J. C., Hwang, H. S., Lee, M. G., Kim, M., & Lee, J. H. 2012, ApJ, 756, 95
- Lipari, S., Colina, L., & Macchetto, F. 1994, ApJ, 427, 174
- Lorente, R., Onaka, T., Ita, Y., et al. 2008, AKARI IRC Data User Manual (Version 1.4), <http://www.ir.isas.jaxa.jp/ASTRO-F/Observation/DataReduction/IRC/>
- Lutz, D. 1999, in ESA Special Publication, Vol. 427, The Universe as Seen by ISO, ed. P. Cox & M. Kessler, 623
- Lutz, D., Feuchtgruber, H., Genzel, R., et al. 1996, A&A, 315, L269
- Mirabel, I. F., Lutz, D., & Maza, J. 1991, A&A, 243, 367
- Mori, T. I., Onaka, T., Sakon, I., et al. 2014, ApJ, 784, 53
- Moshir, M., Kopman, G., & Conrow, T. A. O. 1992, *IRAS Faint Source Survey, Explanatory Supplement Version 2* (Pasadena, CA: California Institute of Technology)
- Murakami, H., Baba, H., Barthel, P., et al. 2007, PASJ, 59, 369
- Murphy, E. J., Condon, J. J., Schinnerer, E., et al. 2011, ApJ, 737, 67
- Murphy, Jr., T. W., Soifer, B. T., Matthews, K., Armus, L., & Kiger, J. R. 2001, AJ, 121, 97
- Nagar, N. M., Wilson, A. S., Falcke, H., Veilleux, S., & Maiolino, R. 2003, A&A, 409, 115
- Nakagawa, T., Enya, K., Hirabayashi, M., et al. 2007, PASJ, 59, 377
- Nardini, E., Risaliti, G., Salvati, M., et al. 2009, MNRAS, 399, 1373
- Neugebauer, G., Habing, H. J., van Duinen, R., et al. 1984, ApJ, 278, L1
- Ohya, Y., Onaka, T., Matsuhara, H., et al. 2007, PASJ, 59, 411
- Onaka, T., Matsuhara, H., Wada, T., et al. 2007, PASJ, 59, 401
- Osterbrock, D. E., & Ferland, G. J. 2006, *Astrophysics of Gaseous Nebulae and Active Galactic Nuclei* (2nd ed.; Sausalito, CA: University Science Books)

- Peters, T., Longmore, S. N., & Dullemond, C. P. 2012, MNRAS, 425, 2352
- Prouton, O. R., Bressan, A., Clemens, M., et al. 2004, A&A, 421, 115
- Rothberg, B., & Joseph, R. D. 2006, AJ, 131, 185
- Rupke, D. S. N., Veilleux, S., & Baker, A. J. 2008, ApJ, 674, 172
- Sanders, D. B., Egami, E., Lipari, S., Mirabel, I. F., & Soifer, B. T. 1995, AJ, 110, 1993
- Sanders, D. B., Mazzarella, J. M., Kim, D.-C., Surace, J. A., & Soifer, B. T. 2003, AJ, 126, 1607
- Sanders, D. B., & Mirabel, I. F. 1996, ARA&A, 34, 749
- Sanders, D. B., Soifer, B. T., Elias, J. H., et al. 1988, ApJ, 325, 74
- Seaton, M. J. 1959, MNRAS, 119, 90
- Shih, H.-Y., & Rupke, D. S. N. 2010, ApJ, 724, 1430
- Shiple, H. V., Papovich, C., Rieke, G. H., et al. 2013, ApJ, 769, 75
- Storey, P. J., & Hummer, D. G. 1995, MNRAS, 272, 41
- Strauss, M. A., & Huchra, J. 1988, AJ, 95, 1602
- Strauss, M. A., Huchra, J. P., Davis, M., et al. 1992, ApJS, 83, 29
- Theios, R. L., Malkan, M. A., & Ross, N. R. 2016, ApJ, 822, 45
- Valdés, J. R., Berta, S., Bressan, A., et al. 2005, A&A, 434, 149
- van Buren, D., Mac Low, M.-M., Wood, D. O. S., & Churchwell, E. 1990, ApJ, 353, 570
- Veilleux, S., Kim, D.-C., & Sanders, D. B. 1999a, ApJ, 522, 113
- Veilleux, S., Kim, D.-C., Sanders, D. B., Mazzarella, J. M., & Soifer, B. T. 1995, ApJS, 98, 171
- Veilleux, S., & Osterbrock, D. E. 1987, ApJS, 63, 295
- Veilleux, S., Sanders, D. B., & Kim, D.-C. 1997, ApJ, 484, 92

- . 1999b, *ApJ*, 522, 139
- Veilleux, S., Rupke, D. S. N., Kim, D.-C., et al. 2009, *ApJS*, 182, 628
- Verner, D. A., & Ferland, G. J. 1996, *ApJS*, 103, 467
- Werner, M. W., Roellig, T. L., Low, F. J., et al. 2004, *ApJS*, 154, 1
- Willett, K. W., Darling, J., Spoon, H. W. W., Charmandaris, V., & Armus, L. 2011, *ApJS*, 193, 18
- Wood, D. O. S., & Churchwell, E. 1989, *ApJS*, 69, 831
- Wu, Y., Charmandaris, V., Huang, J., Spinoglio, L., & Tommasin, S. 2009, *ApJ*, 701, 658
- Yamada, R., Oyabu, S., Kaneda, H., et al. 2013, *PASJ*, 65, 103
- Yano, K., Nakagawa, T., Isobe, N., & Shirahata, M. 2016, *ApJ*, 833, 272
- York, D. G., Adelman, J., Anderson, Jr., J. E., et al. 2000, *AJ*, 120, 1579